

**Towards High Energy Density Anode-less Lithium Metal Batteries  
A Study of Lithium Dendrites Suppression and Elimination**

Wang, C.

**DOI**

[10.4233/uuid:79489c85-e9be-41ff-b79a-10d2b974fc94](https://doi.org/10.4233/uuid:79489c85-e9be-41ff-b79a-10d2b974fc94)

**Publication date**

2021

**Document Version**

Final published version

**Citation (APA)**

Wang, C. (2021). *Towards High Energy Density Anode-less Lithium Metal Batteries: A Study of Lithium Dendrites Suppression and Elimination*. [Dissertation (TU Delft), Delft University of Technology]. <https://doi.org/10.4233/uuid:79489c85-e9be-41ff-b79a-10d2b974fc94>

**Important note**

To cite this publication, please use the final published version (if applicable).  
Please check the document version above.

**Copyright**

Other than for strictly personal use, it is not permitted to download, forward or distribute the text or part of it, without the consent of the author(s) and/or copyright holder(s), unless the work is under an open content license such as Creative Commons.

**Takedown policy**

Please contact us and provide details if you believe this document breaches copyrights.  
We will remove access to the work immediately and investigate your claim.

# **Towards High Energy Density Anode-less Lithium Metal Batteries**

**A Study of Lithium Dendrites Suppression and  
Elimination**

Dissertation

for the purpose of obtaining the degree of doctor

at Delft University of Technology

by the authority of the Rector Magnificus, Prof.dr.ir. T.H.J.J. van der Hagen,

chair of the Board for Doctorates

to be defended publicly on

Wednesday 2 June 2021 at 10:00 o'clock

by

**Chao WANG**

Master of Engineering in Materials Engineering,

Tsinghua University, China

born in Hubei, China

This dissertation has been approved by the promotor.

Composition of the doctoral committee:

Rector Magnificus	chairperson
Prof.dr.ir. M. Wagemaker	Delft University of Technology, promotor
Prof. dr. E. H. Brück	Delft University of Technology, promotor

.....

Independent members:

Dr. Y.-B. He	Tsinghua University, China
Prof.dr. Y. Yang	Xiamen University, China
Prof.dr. M. Tromp	University of Groningen, the Netherlands
Prof.dr. F.M. Mulder	Delft University of Technology, the Netherlands
Dr. E.M. Kelder	Delft University of Technology, the Netherlands



The work described in this thesis was carried out in the group of Storage of Electrochemical Energy (SEE), Faculty of Applied Sciences, Delft University of Technology. This work was partially supported by Guangzhou Elite Project (GEP).

Keywords: Lithium metal batteries, high dielectric, dendrite suppression and elimination, high reversibility, high energy density.

**ISBN 978-94-6423-289-9**

Copyright © 2021 by Chao Wang

Printed by ProefschriftMaken

An electronic version of this dissertation is available at <https://repository.tudelft.nl/>

*To my family*



## Contents

<b>Chapter 1 Introduction</b> .....	<b>1</b>
1.1 Rechargeable batteries for a sustainable future .....	2
1.2 The choice of lithium metal batteries.....	2
1.3 Dendrite in liquid lithium metal batteries .....	4
1.3.1 Mechanisms of dendrite formation.....	4
1.3.2 Approaches for dendrite suppression .....	6
1.3.3 Approaches for dendrite regulation .....	7
1.3.4 Approaches for dendrite elimination .....	10
1.4 Dendrite in solid-state lithium metal batteries .....	12
1.4.1 Dendrites in solid polymer electrolytes.....	12
1.4.2 Dendrites in inorganic solid-state electrolytes.....	16
1.5 Li-S batteries with a safe lithium metal anode .....	20
1.6 Work in this thesis .....	22
References .....	23
<b>Chapter 2 High Dielectric 3D Scaffold to Suppress Lithium-Dendrites and Increase the Reversibility of Anode-less Lithium-Metal Anodes</b> .....	<b>37</b>
Abstract .....	38
2.1 Introduction .....	39
2.2 Materials and methods .....	41
2.3 Results and discussions .....	43
2.3.1 Electrical field calculations .....	43
2.3.2 Electrode preparation .....	45
2.3.3 <i>Operando</i> solid-state NMR .....	45
2.3.4 Electrochemical evaluation half cells .....	48
2.3.5 Li-metal morphology .....	50

## Table of Contents

---

2.4 Discussion and conclusions .....	51
References .....	53
Supporting Information for Chapter 2.....	57
<b>Chapter 3 High Dielectric Barium Titanate Skeleton for All-Solid-state Lithium-Metal Battery.....</b>	<b>65</b>
Abstract .....	66
3.1 Introduction.....	67
3.2 Material and methods .....	68
3.2.1 Preparation of anode materials and solid-state electrolyte .....	68
3.2.2 Characterization of the materials and the electrodes.....	69
3.2.3 Assembly and electrochemical tests of the cells.....	69
3.2.4 Electrical field calculations .....	70
3.3 Results and discussions .....	70
3.3.1 Electrical field calculations .....	70
3.3.2 Electrode preparation .....	73
3.3.3 Electrochemical evaluation of the composite electrodes in symmetrical cells.....	74
3.3.4 Li metal morphology after cycling .....	78
3.3.5 Full cell cycling when paired with a $\text{Li}_4\text{Ti}_5\text{O}_{12}$ cathode.....	79
3.3.6 Solid-state NMR.....	81
3.4 Conclusion and outlook .....	82
References .....	83
Supporting Information for Chapter 3.....	87
<b>Chapter 4 Controlling the Lithium-Metal Growth To Enable Low-Lithium-Metal-Excess All-Solid-State Lithium-Metal Batteries .....</b>	<b>97</b>
Abstract .....	98
4.1 Introduction.....	99

## Table of Contents

---

4.2 Results and discussions .....	100
4.2.1 Characterization of electrochemical performance and Li deposition morphology .....	100
4.2.2 Neutron depth profiling.....	103
4.2.3 Full cell performance of prelithiated ZnO@Cu anode and LiFePO <sub>4</sub> cathode.....	105
4.3 Conclusions.....	106
4.4 Experimental section .....	106
References.....	108
Supporting Information for Chapter 4.....	112
<b>Chapter 5 Quantifying the local Li-ion diffusion over the grain boundaries of a protective coating, revealing the impact on the macroscopic Li-ion transport in an all-solid-state battery .....</b>	<b>115</b>
Abstract .....	116
5.1 Introduction.....	117
5.2 Methods .....	119
5.2.1 Solid electrolyte and cathode active materials preparation .....	119
5.2.2 Material characterization .....	119
5.2.3 Solid-state lithium battery preparation and electrochemical performance .....	120
5.2.4 Solid-state <sup>6</sup> Li NMR measurements.....	120
5.3 Results and discussion .....	120
5.3.1 Stability of solid electrolytes, nanosized versus micronized .....	120
5.3.2 Electrode and Lil coating synthesis and characterization .....	123
5.3.3 Li-ion conductivity and role of Lil in the Li-ion transport mechanism.....	124
5.3.4 Electrochemical performance .....	128
5.4 Conclusions.....	129
References.....	131



## Table of Contents

---

Supporting Information for Chapter 5.....	136
<b>Summary .....</b>	<b>142</b>
<b>Samenvatting.....</b>	<b>145</b>
<b>Acknowledgements.....</b>	<b>149</b>
<b>List of Publications .....</b>	<b>151</b>
<b>Curriculum Vitae .....</b>	<b>154</b>

## Chapter 1 Introduction

## 1.1 Rechargeable batteries for a sustainable future

Rechargeable Li-ion cells are key components of portable, entertainment, computing and telecommunication equipment required by today's information-rich, mobile society. Despite the impressive growth in sales of batteries worldwide, the science underlying battery technology is often criticized for its slow advancement.<sup>1</sup> Many mobile phones cannot make it through a day without being recharged. Most electric cars can travel for only 300 kilometres or less before they have to be plugged in for hours to recharge.<sup>2</sup> The challenge to develop batteries that last longer, charge more quickly and cost less is to store as much lithium ions per gram of electrode as possible and get them to flow back and forth between the anode and cathode as easily as possible, without losing them on the way. Among the diverse existing systems (**Figure 1.1**),<sup>3</sup> Li-based batteries currently outperform other systems due to their high energy density and design flexibility which draws the attention at both fundamental and industrial levels. Today research of rechargeable batteries plays an important role in a sustainable future.

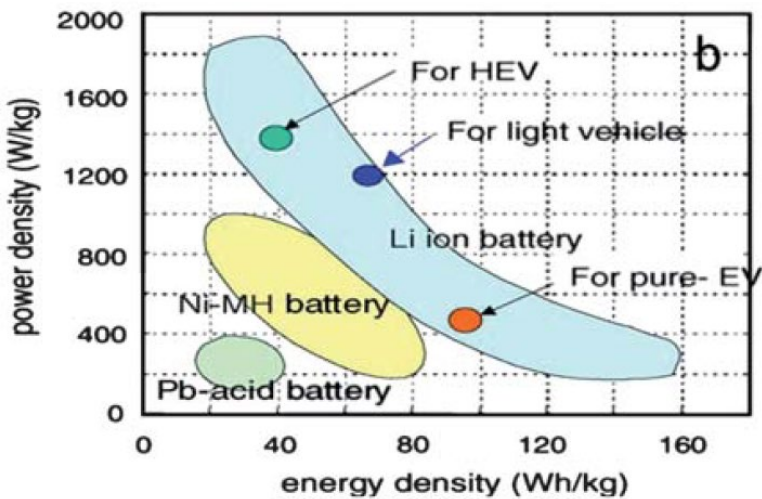


**Figure 1.1** Comparison of the different battery technologies in terms of power density and gravimetric energy density. Reproduced from ref. 3 with permission from The Royal Society of Chemistry, Copyright 2011.

## 1.2 The choice of lithium metal batteries

A battery is composed of several components (anode, cathode, separator, electrolyte, etc.) and can be connected in series and/or in parallel to provide the required voltage and capacity, respectively. Once two electrodes are connected externally with a device, the

chemical reactions proceed in tandem at both electrodes, thereby liberating electrons and enabling the current to be tapped by the user. With the increasing demand for state-of-the-art portable electronics, electric vehicles, and grid energy storage stations, rechargeable batteries with ultra-high energy density and safe operation have gained increasing attention.<sup>4</sup> Insertion-type lithium-ion batteries (LIBs) have demonstrated great success in consumer electronic devices in the past 20 years. However, they are now approaching their energy density limit and cannot satisfy the progressive requirements of advanced energy storage applications.<sup>5</sup> Compared with commercialized LIBs, lithium metal batteries (LMBs) can achieve higher energy densities due to the ultrahigh theoretical capacity ( $3860 \text{ mA h g}^{-1}$ ) and low electrochemical potential ( $-3.04 \text{ V}$  vs the standard hydrogen electrode) of lithium metal anodes (LMAs).<sup>6-7</sup> In fact, LMAs were employed in the 1970s, but they have been quickly discarded owing to the growth of ramified and dendritic Li morphologies in combination with liquid electrolytes.<sup>2, 8</sup> The uncontrollable dendrite growth continuously consumes the electrolyte and the lithium and can puncture the separator, resulting in the repeated formation of a solid electrolyte interphase (SEI), irreversible capacity loss, short circuits, and safety hazards.<sup>9-11</sup> The dendrite formation becomes more serious under high current densities and long cycling operation.<sup>12</sup> Compared to liquid electrolytes, solid-state electrolytes (SSEs) are considered to be able to inhibit Li dendrites and build safe solid Li-metal batteries. This non-liquid system is suggested to tolerate both high voltages and temperatures, which should enable solid-state Li-metal batteries to be safer and possess higher energy densities than liquid electrolyte systems. SSEs possess a high shear modulus based on which it has been suggested that dendrite suppression can be effectively achieved.<sup>13</sup> Besides, SSEs are single-ion conductors, and thus have a high Li-ion transference number close to unity, suppressing Li-ion depletion and subsequent inhomogeneous Li-metal deposition.<sup>14</sup> However, many challenges remain at the interface between SSEs and electrodes due to thermodynamic and electrochemical instability in contact with Li-metal anodes, penetration of Lithium metal through solid electrolyte facilitated by the electronic conductivity,<sup>15</sup> and the reliance of ionic diffusion on the contact of solid particles, slowing down the development of solid-state Li-metal batteries. Therefore, to unlock the full potential of LMBs with high energy density and safe operation, it is imperative to devote efforts in alleviating and even eradicating dendrite growth in both liquid and solid-state batteries.

## 1.3 Dendrite in liquid lithium metal batteries

### 1.3.1 Mechanisms of dendrite formation

In order to solve the dendrite problem in lithium metal batteries in combination with a liquid electrolyte, the dendrite growth mechanisms are intensively investigated. Several models (**Table 1.1**)<sup>12</sup> describing dendrite formation have been proposed, including the space-charge model, deposition and dissolution model, heterogeneous nucleation model, and stress-driven dendrite growth model.

**Table 1.1** Theoretical Models for Dendrite Formation and Corresponding Strategies, Reproduced from ref. 12 with permission from American Chemical Society, Copyright 2019.

Models	Mechanisms	Strategy	Reference
Space-charge model	Ion diffusion and depletion	Dendrite suppression	16
Heterogeneous nucleation model	Nuclei formation and growth	Dendrite regulation	17
Deposition and dissolution model	Surface tension regulation	Dendrite suppression	18
Stress-driven model	Residual stress release	Dendrite elimination	19

Among these four models, the space charge model is most widely accepted to promote Lithium dendrite formation. Chazalviel verified that the occurrence of tree-like lithium was mainly caused by the formation of a space-charge layer in dilute solutions.<sup>16</sup> The model predicts that dendrites would appear when the Li-ion concentration near the electrode decreases sharply under a high current density, where the onset time of dendrite growth is called Sand's time ( $\tau$ ) (equation 1.1):

$$\tau = \pi D \frac{eC_0(\mu_a + \mu_{Li^+})^2}{2J\mu_a^2} \quad (\text{equation 1.1})$$

where  $D$  is the ambipolar diffusion coefficient,  $e$  is the electronic charge,  $C_0$  is the initial electrolyte concentration,  $J$  is the effective current density, and  $\mu_a$  and  $\mu_{Li^+}$  are the anionic and  $Li^+$  mobility, respectively. According to the model by Chazalviel, Sand's time  $\tau$  empirically relies on the electron and Li-ion transfer number. A prolonged Sand's time can

be achieved by dissipating the effective current density ( $J$ ) or accelerating Li-ion mobility ( $\mu_{Li^+}$ ). Therefore, strategies which can help to homogenize the electric field distribution and facilitate Li-ion diffusion are promising in inhibiting dendrite formation. The heterogeneous nucleation model was used to predict the early stages of nucleation and growth for reaction rate limited systems. Ely and García analysed the heterogeneous nucleation process and distinguished five regimes: the nucleation suppression regime, the long incubation time regime, the short incubation time regime, the early growth regime, and the late growth regime.<sup>17</sup> Based on this model, the dendrites can be suppressed by engineering the anode electrode surface roughness, adjusting anode particle size, limiting the plating potential and controlling the wetting properties of the electrodeposits. The deposition and dissolution model indicated that whisker growth occurs from the base. Yamaki proposed that a protective layer with a large surface tension could lead to even lithium deposition.<sup>18</sup> Recently, a stress-driven dendrite growth model was brought forward by Jiang<sup>19</sup> showing that the presence of compressive stress during Li plating and stripping will promote Li dendrite initiation and that Li dendrites can be effectively suppressed by counteracting the residual stress using soft substrates (**Figure 1.2**). According to this model, a stress-relieving mechanism can be utilized to design desirable dendrite-free Li plating in LMAs.

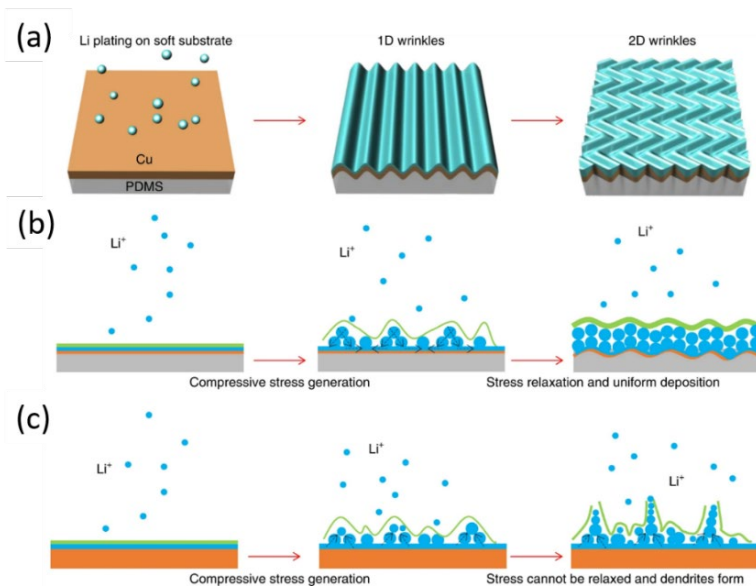


**Figure 1.2** Schematic figures of Li plating on different substrates. (a) Lithium plating on a Cu thin film. (b) Li electroplating process on a soft substrate. (c) Lithium plating process on a thick Cu foil. Orange, blue, green and grey represent Cu, Li, SEI and PDMS, respectively. Reproduced from ref. 19 with permission from Springer Nature, Copyright 2018.

### 1.3.2 Approaches for dendrite suppression

The space-charge, deposition, dissolution and stress-driven models of dendrite formation presented above have inspired strategies to dissipate the effective deposition current densities ( $\mu_{\text{Li}^+}$ ) and release the surface tension ( $\gamma$ ) to achieve safe LMA. The inhomogeneous Li-ion flux distribution usually leads to non-uniform Li nucleation initiating inhomogeneous Li deposition and dendrite proliferation on planar Li foil electrodes.<sup>20</sup> Owing to the “hostless” structure of Li metal electrodes the anode suffers from volume changes which can induce crack formation in the battery configuration, ultimately causing a short-circuit. Therefore, rational 3D electrode frameworks with novel architectures have been designed to control the Li plating/stripping behaviour and improve the Li-metal anode stability. Among the various skeleton materials, carbon-based materials or metallic frameworks are widely chosen to build the 3D structure as a lithium host. These electrically conductive substrates with 3D structures can offer a network of free electron pathways and provide sufficient contact with Li-ion flux in liquid electrolytes, enabling fast charge transfer and uniform Li nucleation. In addition, the Li host substrate should possess mechanical and electrochemical stability, high electrical or ionic conductivity for fast electron/ion transfer, and a low gravimetric density for a high energy density.<sup>21-22</sup>

Recently, Luo et al<sup>23</sup> reported a conducting, lightweight, and lithiophilic scaffold that can stabilize high loading of Li during cycling and avoid its dendritic filament growth. The crumpled paper ball-like graphene scaffold (CGB) was synthesized through the isotropic capillary compression method with high Li loading up to 10 mA h cm<sup>-2</sup> within tolerable volume fluctuations (**Figure 1.3**). High Coulombic efficiency of 97.5% over 750 cycles was achieved at a current density of 0.5 mA cm<sup>-2</sup>. Scanning electronic microscopy (SEM) images show that plating/stripping Li up to 10 mA h cm<sup>-2</sup> on crumpled graphene scaffold does not suffer from dendrite growth, which is mainly ascribed to the dissipated current density, decreased mechanical stress, and confined hollow volumes.

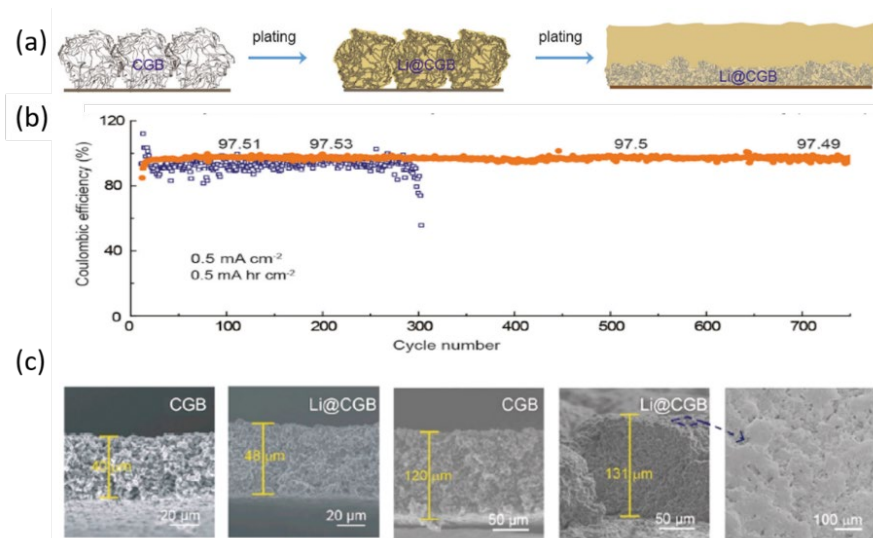


**Figure 1.3** (a) Schematic of the CGB scaffold with high Li metal loading. (b) Coulombic efficiency of CGB electrodes and bare Cu electrodes with Li deposition capacity of  $0.5 \text{ mA h cm}^{-2}$  at a current density of  $0.5 \text{ mA cm}^{-2}$ . (c) Thickness variation of CGB electrodes after plating 3.75 and  $10 \text{ mA h cm}^{-2}$  Li and surface morphology of  $120 \mu\text{m}$  thick CGB after plating  $10 \text{ mA h cm}^{-2}$  Li. Reproduced from ref. 23 with permission from Elsevier, Copyright 2018.

Another 3D porous current collector for lithium metal anodes was designed by He and co-workers by means of an easily manipulated and low-cost chemical dealloying approach.<sup>24</sup> The interconnected 3D Cu framework was fabricated by the complete dissolution of Zn from the Cu-Zn alloy tape, and the simultaneously generated pore structure can effectively accommodate the deposited Li metal, alleviates the severe volume change of Li metal, and suppresses the formation of lithium dendrites. The excellent electrochemical performance was achieved by this 3D porous current collector with a high Coulombic efficiency of 97% for 250 cycles at the current density of  $0.5 \text{ mA cm}^{-2}$  for 1000 h.

### 1.3.3 Approaches for dendrite regulation

Extending Sand's time or physically blocking the dendrite growth is an effective way for dendrite suppression at small current densities and low areal capacities.<sup>25</sup> However, when it comes to high mass loadings and current densities, the above methods become invalid because the lithium dendrite formation is a kinetically and thermodynamically favourable process.<sup>26-27</sup> Thus, methods to regulate dendrite formation and growth are considered to solve these problems. Dendrite regulation means that dendrite formation and growth is allowed during plating, controlled by dendrite nucleation sites, the electric field distribution, and ion transport directions to achieve a well-deposited Li layer. Here, two representative



strategies to regulate and confine dendrite growth are introduced as follows: (i) regulating Li nucleation sites and (ii) controlling Li growth pathways and directions.<sup>12</sup>

Li nucleation is the initial state for Li dendrite growth. Once Li nuclei are generated, Li ions prefer to deposit on these active sites because of the lowered interface energy. Recently, Guo showed that a 3D Cu foil current collector with a submicron skeleton and high electroactive surface area can improve lithium deposition behaviour without the formation of uncontrollable Li dendrites (**Figure 1.4**).<sup>28</sup> This 3D substrate can run at least 600 h without a short circuit and suppresses the growth of lithium dendrites. Because of the rational design of the 3D current collector, this special lithium host can accommodate a high areal capacity and can achieve a high coulombic efficiency of 98.5%. The exceptional electrochemical performance of the Li-metal anode in the 3D current collector highlights the importance of regulating the lithium plating bringing forward new avenues for developing Li anodes with a long lifespan.

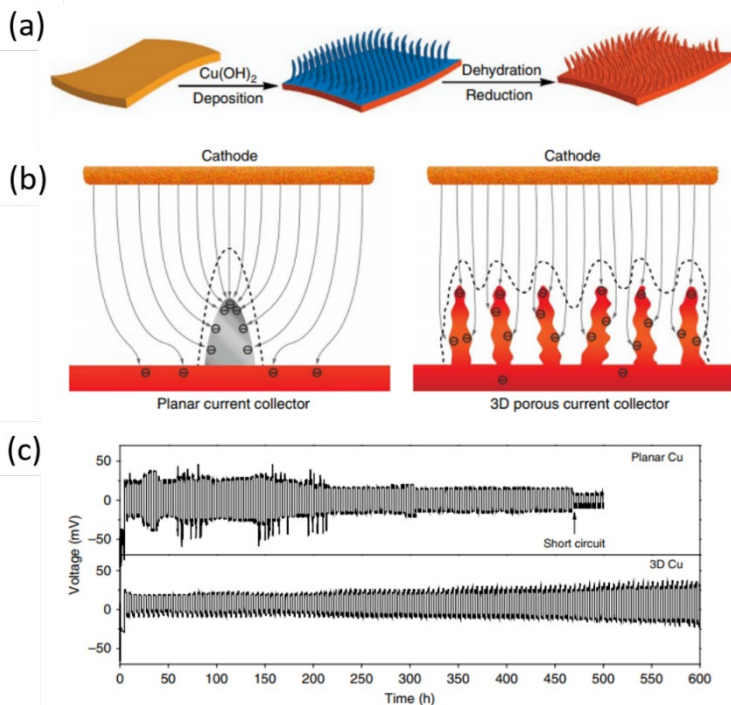


**Figure 1.4** (a) Schematic of the processes to prepare a 3D porous Cu foil from a planar Cu foil. (b) Electrochemical deposition behaviour of lithium metal on a planar current collector and 3D current collector. (c) Voltage profiles of Li metal plating/stripping at  $0.2 \text{ mA cm}^{-2}$  in symmetric Li|Li@Cu cells with planar or 3D Cu foil as the current collector. Reproduced from ref. 28 with permission from Nature Publishing Group, Copyright 2015.

Hu and co-workers designed and fabricated a 3D porous skeleton with well-aligned channels for a homogeneous and stable lithium plating/stripping (**Figure 1.5**).<sup>29</sup> Due to carbonized wood (C-wood)'s 3D porous conductive framework structure, lithium metal can be accommodated in the host without volume fluctuations during long-term cycling. Moreover, the channel structure of Li/C-wood electrodes effectively guides and confines the Li stripping/plating process in the channels. As a result, a long lifespan of cycling stability with a small overpotential of Li/C-wood electrodes was achieved under a high current density of  $3 \text{ mA cm}^{-2}$  using the normal carbonate-based electrolyte. The strategy using aligned channels from wood to guide the lithium plating and stripping activity and confine the volume change of lithium metal motivates future research in framework design for high-capacity, dendrite-free Li metal anodes.

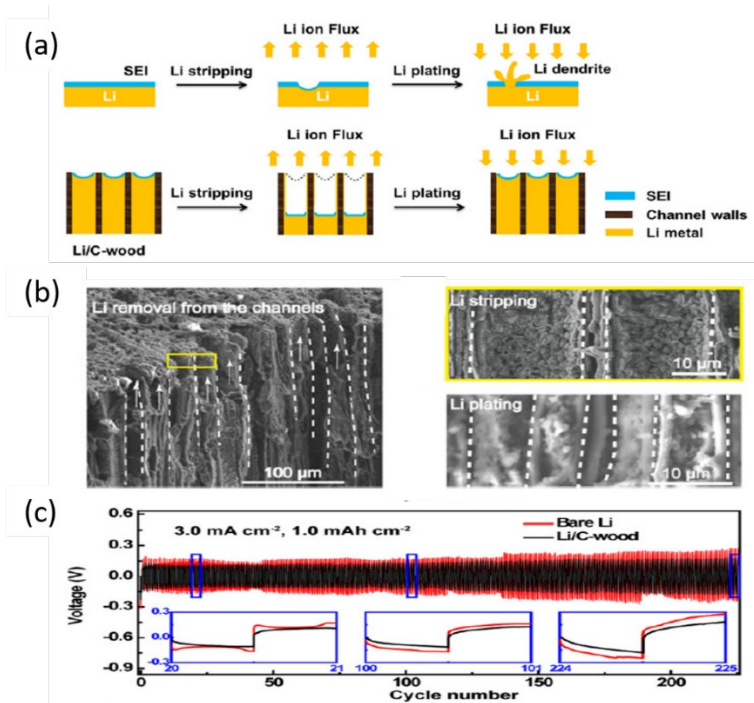


**Figure 1.5** (a) Schematic of Li stripping/plating for bare Li metal electrodes and Li/C-wood electrodes with well-aligned channels. (b) Cross-sectional SEM images of the Li/C-wood after stripping Li and subsequent plating. (c) Voltage profiles of the Li/C-wood cell and bare Li metal cell at current densities of  $3 \text{ mA cm}^{-2}$  with an areal capacity of  $1 \text{ mA h cm}^{-2}$ . Reproduced from ref. 29 with permission from National Academy of Sciences, Copyright 2017.

### 1.3.4 Approaches for dendrite elimination

Dendrite elimination is an arduous challenge and is the ultimate goal for dendrite control to achieve safe LMAs. It was mentioned already above that the stress-driven dendrite growth model predicts that filament-like dendrite grows under compressive stress. Thus methods to release the stress or eliminate filamentary dendrites through mechanical force has drawn the attention of researchers.

Tip dendrite growth is easy to be observed on planar Cu current collectors with a rough surface due to the inhomogeneous local electric field.<sup>30-31</sup> It is also common sense that the migration of charged particles could be affected by the Lorentz force if the trajectory cuts magnetic induction lines. Thus, the  $\text{Li}^+$  concentration around the tips, caused by the uneven electric field distribution, can be taken away by manipulating the Lorentz force using an applied magnetic field such that the tip dendrite growth can be eliminated (**Figure 1.6**).<sup>32</sup> In ether electrolytes, Li tends to grow into microspheres, and their size increase in accordance with the increase of magnetic field intensity. The relationship between current density and magnetic flux intensity is simulated by COMSOL Multiphysics simulation, and the results are also confirmed by monitoring the deposited lithium morphology as well as the electrochemical performance. Lu et al also found that the Lorentz force could help in eliminating dendrite growth.<sup>33</sup>

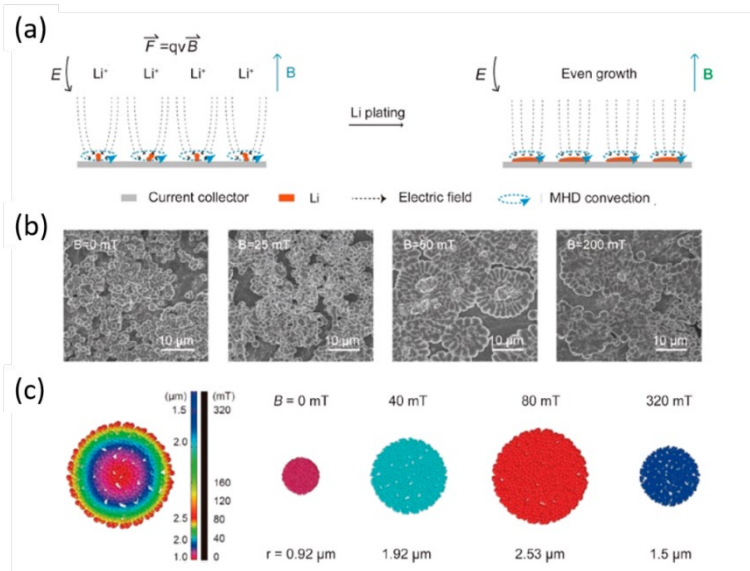


**Figure 1.6** (a) Schematic of the dendrite elimination process by applying a Lorentz force by introducing a magnetic field. (b) Morphology difference of the anode plated at different magnetic fields. (c) Simulation results of the Li

deposition area as a function of the magnetic field strength by the COMSOL finite element analysis. Reproduced from ref. 32 with permission from Wiley-VCH, Copyright 2019.

Electrode pulverization is another notorious problem in LMAs that always causes low coulombic efficiencies and subsequent anode failure. In metallurgy, bulk nanocomposite materials with refined nanostructures are designed to release lattice stresses while enhancing the integrated yield stress, which also can be used for LMAs.<sup>34</sup> Lu et al. transplanted the concept into constructing a stable  $\text{Al}_2\text{O}_3$ -based inorganic framework with lithium aluminium oxide interphase by reacting Li with  $\text{Al}_2\text{O}_3$  nanoparticles (Figure 1.7).<sup>35</sup> The  $\text{Al}_2\text{O}_3$ -based inorganic nanocomposites can serve as a stable Li “host,” reducing the volume expansion and reducing the ion concentration gradient near the surface protrusion, thus reducing uneven lithium electrodeposition and keeping an integrate anode structure. Cycling performance with this 3D composite electrode can be achieved under a current of  $8 \text{ mA cm}^{-2}$  over 480 cycles. Lithium dendrites were absent after cycling under  $8 \text{ mA cm}^{-2}$  as compared to bare Lithium electrodes. Thus, mechanical force plays an important role in strategies to eliminate dendrite formation.

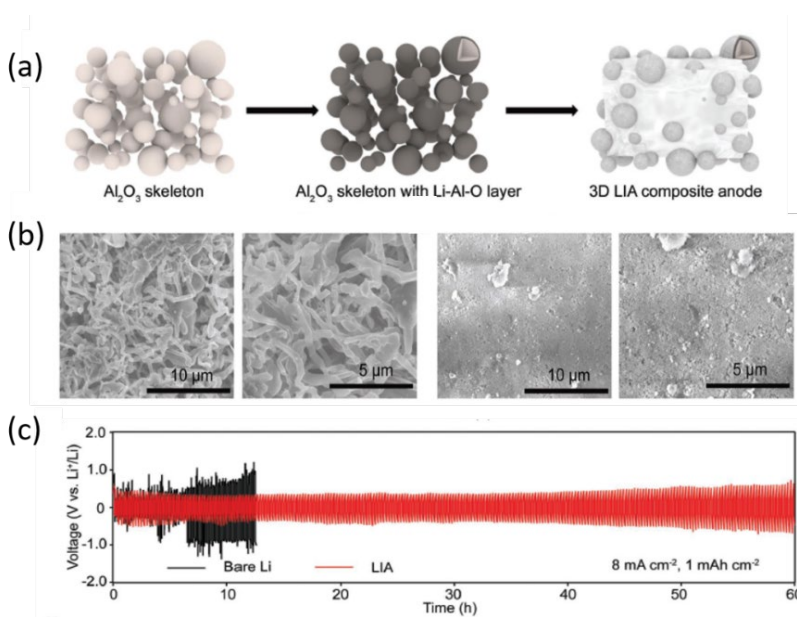


**Figure 1.7** (a) Schematic of  $\text{Al}_2\text{O}_3$  nanoparticles and a lithium/aluminum oxide (LIA) nanocomposite electrode. (b) SEM images of the surface of a bare Li electrode and the LIA composite electrode. (c) Voltage profiles of the bare Li and LIA electrodes under a current density of  $8 \text{ mA cm}^{-2}$  with a fixed capacity of  $1 \text{ mA h cm}^{-2}$ . Reproduced from ref. 35 with permission from Wiley-VCH, Copyright 2018.

Except for the aforementioned strategies of engineering the LMA, great efforts have also been devoted to suppressing the lithium dendrite growth such as improving the properties of LMA interface<sup>36-40</sup> and optimizing the electrolyte components.<sup>41-43</sup> However, the optimal solution may be in SSEs which benefits from an inflammable electrolyte and improved mechanical properties.<sup>44-46</sup>

### 1.4 Dendrite in solid-state lithium metal batteries

A solid-state electrolyte with a high shear modulus is regarded as an effective “medicine” to suppress lithium filament growth.<sup>47-48</sup> Besides, the merits of nonflammability, non-leakage, high-oxidation voltage and low reduction voltage render the SSEs a promising candidate to build the high-energy-density and high-safety cells.<sup>49-50</sup> Thus, SSEs are widely believed to be the ultimate remedy to solve the issues of filament growth which has hindered the development of high-energy-density and highly safe LMBs. However, experiments did not work out as the reports predicted, the aforementioned hypothesis has been disproven with different electrolyte compositions and testing conditions. For instance, the shear modulus criterion is intended for polymer electrolytes and SSEs with a smooth surface and no defects. Filament lithium can be observed at the interface or along the boundaries and gaps of the SSE systems even under a small capacity and current density. The critical current density (CCD), which is used to identify the short-circuit caused by dendrite piercing, of SSEs is even smaller compared to that for liquid electrolytes.<sup>15, 51</sup> These reports contradicted the hypothesis that the dendrites can be suppressed by SSEs due to their Li-ion transference number close to unity and the larger shear modulus than lithium metal.<sup>52-53</sup> The detailed mechanism for dendrite formation in SSEs is different from the liquid electrolyte and is not fully studied yet.<sup>54-55</sup> Several assumptions are proposed to explain the counterintuitive filament growth in SSEs, such as a small packing pressure, low ionic conductivity at the grain boundaries, high electronic conductivity of electrolytes, inhomogeneities and defects during SSE preparation, soft parts of the SSEs, and poor interfacial contact between two solid electrodes.<sup>56</sup> Therefore, a better understanding of the dendrite growth behavior is imperative for next-generation SSBs with lithium metal anodes.<sup>57-58</sup>

#### 1.4.1 Dendrites in solid polymer electrolytes

Solid polymer electrolytes (SPEs) having properties between inorganic and nonaqueous electrolytes are considered as potential candidates for lithium metal batteries for practical application.<sup>59-61</sup> However, the electrolyte’s ionic transference number, mechanical

properties, surface impurities of Li metal, etc. also render the Li filament growth at the SPE interface.

Ionic transport in SPEs is similar to that in liquid electrolytes and can be precisely described by the concentrated solution theory based on the Onsager–Stefan–Maxwell formalism.<sup>62</sup> Thus, current flux consists of ion transport under both concentration and potential gradients in the SPE, with the cation transference number less than unity.<sup>63</sup> Based on equation 1.1 when the cationic concentration goes to zero at Sand’s time, the unmitigated dendrite growth will be engendered,<sup>64</sup> and therefore, single-ion SPEs are considered stable against Li filament growth in theory.<sup>65–66</sup> Recently, Cao et al proposed a novel SPE by the copolymerization of maleic anhydride and lithium 4-styrenesulfonyl(phenyl sulfonyl)imide with a high Li-ion transference number of  $t_{Li^+} = 0.97$  and excellent ionic conductivity of  $3.08 \times 10^{-4} \text{ S cm}^{-1}$  (**Figure 1.8**).<sup>67</sup> The Li symmetric cell with SPE manifests a stable cycle performance without any short-circuits, suggesting the ability of the novel SPE to suppress the growth of Li dendrites, due to its minimal concentration gradient near the anode. When pairing lithium metal with a  $\text{LiFePO}_4$  cathode using this SPE membrane, the battery shows stable cycling performance. Consequently, this novel SPE membrane is an effective substitution to lower the driving force for dendrite initiation and has the potential for the application in LMBs.

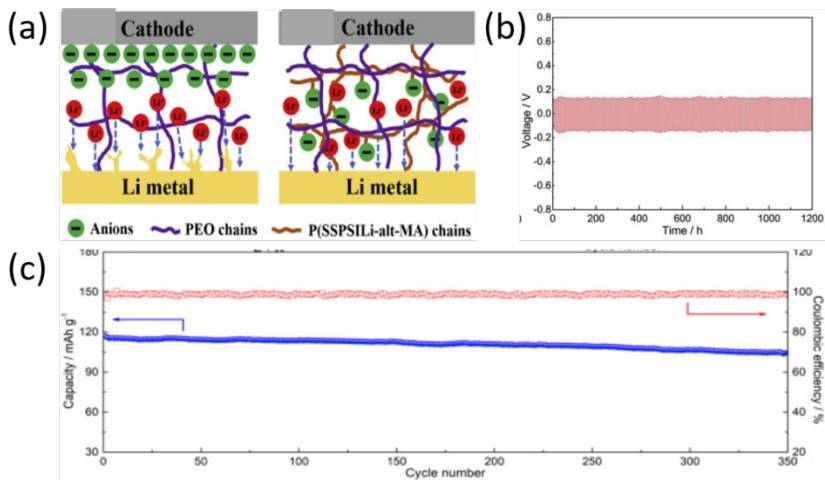


**Figure 1.8** (a) Schematic of the SPE with a high transference number to suppress dendrite growth. (b) Voltage profile of the Li symmetric cell with a 20 wt% SPE membrane. (c) Cycling performance of LFP/20 wt% SPE membrane/Li cell under a current density of 0.1C. Reproduced from ref. 67 with permission from Elsevier, Copyright 2019.

Monroe and Newman proposed that if the shear modulus of a SPE is larger than 6 GPa, Li dendrites could not pierce through the SPE.<sup>68</sup> However, SPEs appear unable to entirely suppress the dendrite growth due to their relatively low shear modulus.<sup>53, 69</sup> Besides, most SPEs need to be cycled at high temperature to boost their low room-temperature ionic conductivity, which further decreases their elastic stiffness and increases the tendency of dendrites penetrating the SSEs, subsequently, leading to cell short circuit and battery failure.<sup>70-71</sup> The dendrites present between the Li electrode and the solid polymer electrolyte have the potential to cause complete delamination at specific spots, deteriorating the cell performance with low cycling efficiency.<sup>72</sup> A kinetic model was brought forward combining the effects of surface tension and stresses at the interface to elicit general criteria for stable Li deposition at solid–solid interfaces with SPEs. Two different stability mechanisms are brought forward from the model for stable Li deposition: pressure-driven in SSEs with a high molar volume ratio and density-driven stability in SSEs with a low molar volume ratio.<sup>65</sup> However, normally SPEs have a high molar volume ratio but a shear modulus below the critical value, resulting in unstable Li deposition. Therefore, a modification of the SPEs to stabilize the working interfaces is strongly suggested to realize Li-dendrite suppression. Recently, Nan et al. proposed a novel poly(vinylidene difluoride) (PVDF)-based solid electrolytes with different Li salts to systematically explore the interface properties with Li metal anode via first-principles calculations (**Figure 1.9**).<sup>73</sup> A special nanoscale in situ formed interface layer was found between the PVDF-based SPEs and the Li anode, which can effectively increase the shear modulus and suppress Li dendrite growth. The system using PVDF-lithium bis(fluorosulfonyl)imide electrolyte enables over 2000 h cycling of Li plating–stripping under a current density of 0.1 mA cm<sup>-2</sup> during 200 cycles in an all-solid-state LiCoO<sub>2</sub> || Li cell under a current density of 0.15 mA cm<sup>-2</sup> with high capacity retention due to the ability of dendrite suppression by the stable interface layer. These findings will suggest optimization strategies of the interfacial stability between the SPEs and Lithium metal to achieve safe all-solid-state Li metal batteries.

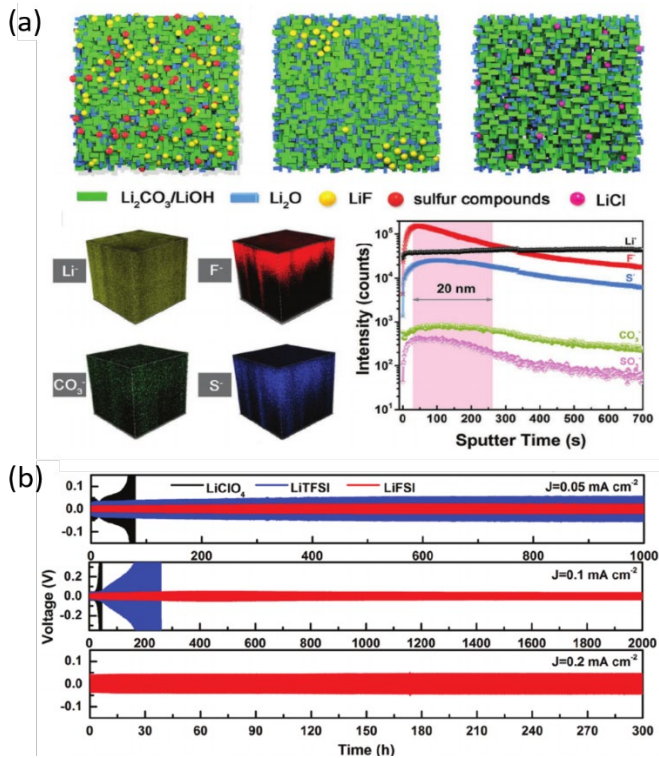


**Figure 1.9** (a) Morphological characterizations of the interface layer. (b) electrochemical characterization of PVDF–LiX electrolytes at a current density of 0.05, 0.1, and 0.2  $\text{mA cm}^{-2}$ . Reproduced from ref. 73 with permission from Wiley-VCH, Copyright 2019.

Local surface impurities prelocated at the Li/SPE interface play a critical role in the formation of dendritic Li.<sup>74-76</sup> In the model of Monroe and Newman, Li is considered as a pure metal, which may not fully represent the real interfacial composition. The impurities are  $\text{Li}_2\text{O}$ ,  $\text{Li}_3\text{N}$ , or  $\text{Li}_2\text{CO}_3$  which are electronically insulating and can cause inhomogeneities in the local current density and prevent the direct reduction of Li on the top of the Li metal.<sup>74, 77-78</sup> Instead, the Li nucleation and plating will be localized at the corner of the impurities and could lead to the formation of voids on the top of the impurities (**Figure 1.10**).<sup>76</sup> Thus, pretreatment strategies for lithium metal may be necessary for the homogeneous deposition of Li metal.<sup>79</sup>



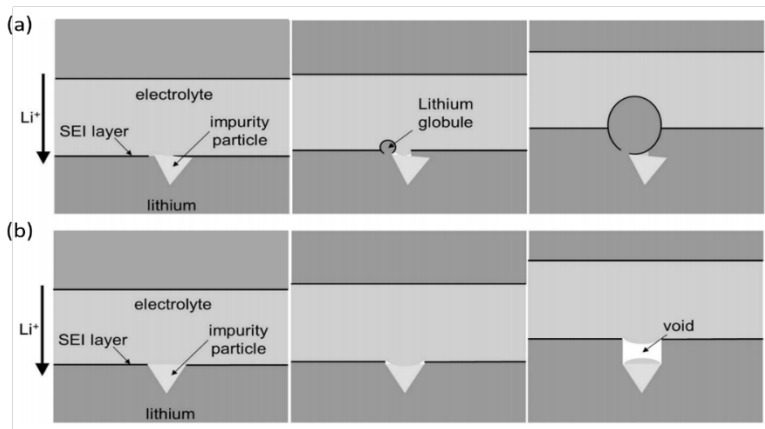


**Figure 1.10** (a) A schematic showing (a) the growth of lithium around the impurities, and (b) the formation of voids on the top of impurities. Reproduced from ref. 76 with permission from Electrochemical Society, Copyright 2015.

#### 1.4.2 Dendrites in inorganic solid-state electrolytes

Inorganic SSEs with high mechanical strength and compactness are considered as the “enabler” to suppress the penetration of lithium dendrites.<sup>80</sup> However, contrary to the normal understanding, lithium filament can be easily formed in inorganic SSEs even at super-low current densities or cycling capacities compared to liquid or solid polymer electrolytes.<sup>81-83</sup> The failure mechanisms for inorganic solid-state electrolytes are distinctly different from that of solid polymer electrolytes, which has been attributed to surface contaminants, microstructural properties of the SSE (such as grain boundaries, cracks, voids, etc.),<sup>84</sup> electronic properties of the electrolyte<sup>85</sup> and the nature of the Li-metal|SE interfacial contact.

Surface contaminants of the SSEs can be the starting point for lithium filament growth. Many ceramic electrolytes have surface contaminants where the lithium-ion diffusion rate is slower than that in SSEs.<sup>79, 86</sup> Thus, the Li-ions are diffusing away from the contaminated areas and focusing on the contact points at the interface, which further leads to the inhomogeneous current distribution and lithium deposition (**Figure 1.11a**).<sup>87</sup> In this case, a modified and cleaning SSE surface is demonstrated to achieve a high current density with no lithium penetration.<sup>79, 88</sup>

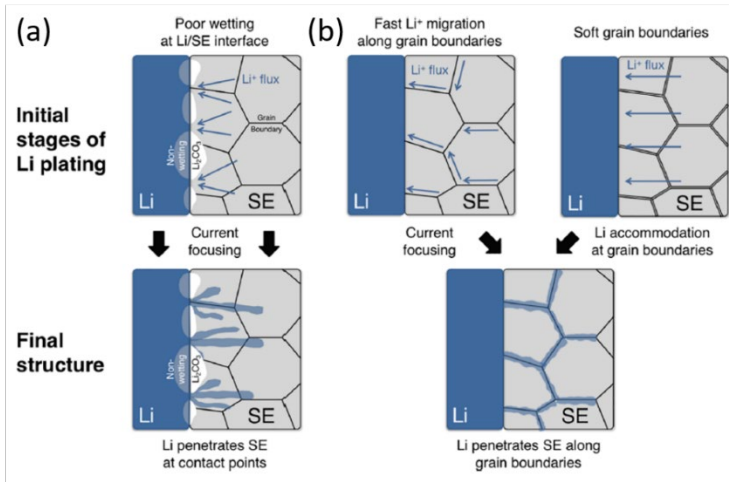


**Figure 1.11** Schematic for potential microstructural contributions to dendritic Li deposition in SSEs. (a) Surface contaminants lead to the dendrite formation in SSEs. (b) Li accumulates in the softer regions near the electrode/grain boundary junction. Reproduced from ref. 87 with permission from American Chemical Society, Copyright 2018.

The grain boundary (GB) is another hot spot for Li dendrite propagation in inorganic SSEs. Significant soft GBs are considered as the origin for dendrite growth in these sites (**Figure 1.11b**). The variations in atomic structure and density near the GB plane result in a decrease in the elastic modulus, which can be 50% lower than that in the bulk SSEs.<sup>89</sup> This inhomogeneous distribution of elastic property leads to the accumulation of deposited Li in softer regions near electrode/grain boundary junctions.<sup>90-91</sup> Consequently, Li protrusions will be generated at the hot spot for the subsequent Li deposition. The gap of ionic conductivity between bulk and GB regions in SSEs is another reason for lithium filament growing along the GBs. Based on the molecular dynamics simulations, the Li-ion mobility through the GBs is sharply reduced, and Li-ion diffusion activation energy for all GBs is significantly higher compared to the bulk SSEs.<sup>92-93</sup> Recent research shows that a severe structural and chemical deviation can be found at the GBs, which is not favourable for Li<sup>+</sup> storage and transport. Consequently, high GB resistance will lead to Li dendrites propagating along the grain boundaries.<sup>91, 94</sup> In this case, processed SSEs with low activation energy and dense GBs can efficiently suppress the lithium filament growth along with the GBs. For instance, element doping,<sup>95-96</sup> sintering,<sup>97-98</sup> and hot-pressing,<sup>99</sup> and additional Lithium,<sup>100</sup> have been demonstrated as the effective methods to control dendrite growth and improve the critical current density of SSEs.

Preexisting voids and cracks in inorganic SSEs or near the electrode/electrolyte interface are potential spots for Li dendrite nucleation. Cracks or voids in the SSE near the Li-metal electrode are favourable for dendrite growth due to the electric field amplification, inevitably penetrating the SSEs from these sites.<sup>101-102</sup> Pressure will be subsequently generated because of the insertion of Li into the voids, which will in turn continue promoting the propagation of cracks. This process will repeat and continue with dendrite growth in the newly formed cracks until the crack reaches the cathode and short-circuits the solid lithium metal battery.<sup>103</sup> Voids in Li metal near the solid interface are also suspicious nucleation spots for Li dendrites. When Li metal is stripped faster than that the Li can be replenished or Li-metal anode matches a Li-free cathode, voids will be generated and accumulated in the Li anode near the interface.<sup>104</sup> Subsequently, Lithium deposition preferentially starts at the junction where Li metal, SSE, and voids meet with an elevated local current density.<sup>105</sup> After many cycles, the extended and interconnected voids will accelerate the propagation of dendrites and further result in irreversible pulverization of Li metal.<sup>106</sup> In this case, densified SSEs and homogeneous Li metal/SSE interfaces with fewer voids and cracks are effective methods to prevent dendrite formation and growth in inorganic SSE lithium metal batteries.<sup>107</sup> Recently, Liu and his co-workers proposed a flat-surface  $\text{Li}_6\text{PS}_5\text{Cl}$  (LPSC) nanorod pellet with high density, which can eliminate the dendrite growth along the GBs and significantly improve the CCD to  $1.05 \text{ mA cm}^{-2}$  at  $25 \text{ }^\circ\text{C}$  (**Figure 1.12**).<sup>108</sup> When employing the densified  $\text{Li}_6\text{PS}_5\text{Cl}$  nanorod pellet in the  $\text{LiCoO}_2$ /pellet-sintered  $\text{Li}_6\text{PS}_5\text{Cl}/\text{Li}$  battery, the superior electrochemical performance of  $92.6 \text{ mA h g}^{-1}$  with a capacity retention of 80.3% after 100 cycles under the current density of  $0.35 \text{ mA cm}^{-2}$  at room temperature was achieved. This work sheds light on the method to suppress dendrite growth and paves the way for the utilization of lithium metal in SSE lithium metal batteries.

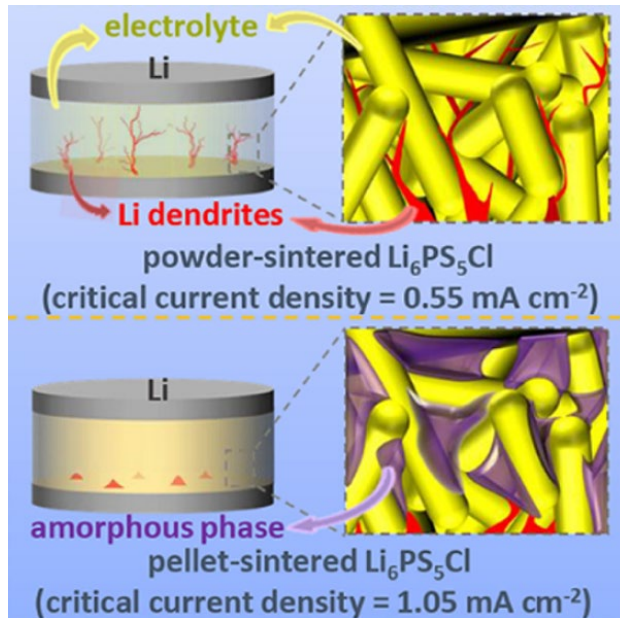


**Figure 1.12** Schematic for the powder-sintered  $\text{Li}_6\text{PS}_5\text{Cl}$  and the pellet-sintered  $\text{Li}_6\text{PS}_5\text{Cl}$  as solid electrolyte for lithium metal plating. Reproduced from ref. 108 with permission from American Chemical Society, Copyright 2020.

The high electronic conductivity of the SEEs is also a notorious factor to accelerate the Li filament growth in SSEs.<sup>109-110</sup> Li-metal dendrites grow directly within the bulk of SSEs, especially starting from the intrinsic GB/voids of the SSE, due to the relatively high electronic conductivity of the SSEs. It is much easier for  $\text{Li}^+$  to receive electrons directly inside the SSEs, rather than the vertical growth from the interface into SSE.<sup>111</sup> Recently, Han and his co-workers found that lowering the electronic conductivity is crucial for suppressing the dendrite growth in the SSEs by comparing the formation behaviour of Li filaments in  $\text{Li}_7\text{La}_3\text{Zr}_2\text{O}_{12}$  (LLZO),  $\text{Li}_2\text{S}-\text{P}_2\text{S}_5$  (LPS) and LiPON.<sup>15</sup> Based on the time-resolved operando neutron depth profiling result, lithium dendrites were observed inside the bulk LLZO and LPS electrolytes (high electronic conductivity), while no apparent changes were found in LiPON (low electronic conductivity). This work sheds light on a basic criterion for SSEs, demonstrating that lowering the electronic conductivity is crucial for dendrite-free Li plating at high current densities in all-solid-state lithium batteries.

Excluding the aforementioned reasons, another group of SSEs (including  $\text{Li}_7\text{P}_3\text{S}_{11}$ ,  $\text{Li}_6\text{PS}_5\text{X}$  ( $\text{X}=\text{Cl}, \text{Br}$ ),  $\text{Li}_{10}\text{GeP}_2\text{S}_{12}$  (LGPS),  $\text{Li}_{1.4}\text{Al}_{0.4}\text{Ge}_{1.6}(\text{PO}_4)_3$  (LAGP), etc.) is not (electro)-chemical stable against the Li-metal anode.<sup>112-114</sup> The newly formed solid electrolyte interphase (SEI) due to the side reactions between lithium metal and SSEs will change the electrical

properties, mechanical integrity, and thermal stability of SSEs and further affect the lithium filament growth in SSEs.<sup>115-116</sup> Consequently, the ideal Li/electrolyte interphase needs to possess the following properties: high ionic conductivity, low electronic conductivity, and a high (electro)-chemical stability to suppress the nucleation of Li dendrites and achieve stable and safe solid-state lithium metal batteries.

### 1.5 Li-S batteries with a safe lithium metal anode

Lithium-Sulfur batteries are regarded as one of the promising candidates for next-generation energy storage devices due to their overwhelming theoretical energy density (2500 W h kg<sup>-1</sup>), low cost, environmental friendliness the natural abundance of S source.<sup>117-118</sup> However, the practical implementation of Li-S batteries suffers from two major challenges. Firstly, the dissolution of Li polysulfide intermediates (Li<sub>2</sub>S<sub>8</sub>-Li<sub>2</sub>S<sub>4</sub>, LiPS) and consequential shuttle effect in liquid organic electrolytes causes severe loss of active material, reducing the life span of Li-S batteries. Secondly, uncontrollable dendrite growth on lithium metal surface induces continuously depletion of the Li anode and electrolyte, resulting in a low Coulombic efficiency (CE) and cycling stability.<sup>119-123</sup> Therefore, controlling the shuttle effect and the dendrite growth simultaneously during the long-term operating lifespan has become a formidable scientific and technical challenge for the practical utilization of Li-S batteries.<sup>25</sup> Recent researches for Li-S batteries and methods are summarized as follows:

1. Electrolyte additives. LiNO<sub>3</sub> as an additive has a high impact on controlling Li dendrite growth and side reactions in Li-S batteries due to the formation of a stable and homogeneous SEI film, resulting from the reaction of LiNO<sub>3</sub> with electrolyte and Li metal. This SEI can effectively isolate the fresh Lithium metal from organic electrolyte and LiPS and eliminate the dendrite growth to achieve a high-performance Li-S battery.<sup>124</sup> However, when increasing the sulphur loading in the pouch cell, the role of LiNO<sub>3</sub> will decay and a progressive reduction will occur between LiNO<sub>3</sub> and Li anode.<sup>125</sup> Therefore, other electrolyte modifications and interface designs are required to stabilize Li metal for the commercial high loading Li-S batteries.

2. Anode coating. Surface coating on the anode is another effective method.<sup>126</sup> Recently, Wang and his co-workers proposed a facile and easy to a scale-up method to modify the lithium metal with a stable and homogenous LiPON coating by nitrogen plasma-assisted deposition of electron-beam reaction evaporation (**Figure 1.13**).<sup>127</sup> The LiPON coating layer can effectively inhibit the corrosion reaction with electrolytes and suppress lithium dendrite growth due to its high ionic conductivity, chemical stability and robust mechanical

properties. Li-S pouch cell could achieve a specific energy density of about  $300 \text{ W h kg}^{-1}$  and a relatively stable CE of about 91% with a high sulfur loading ( $7 \text{ mg cm}^{-2}$ ). This facile and effective approach sheds light on stabilizing the Li metal anode and could result in the practical application of rechargeable Li-S batteries.

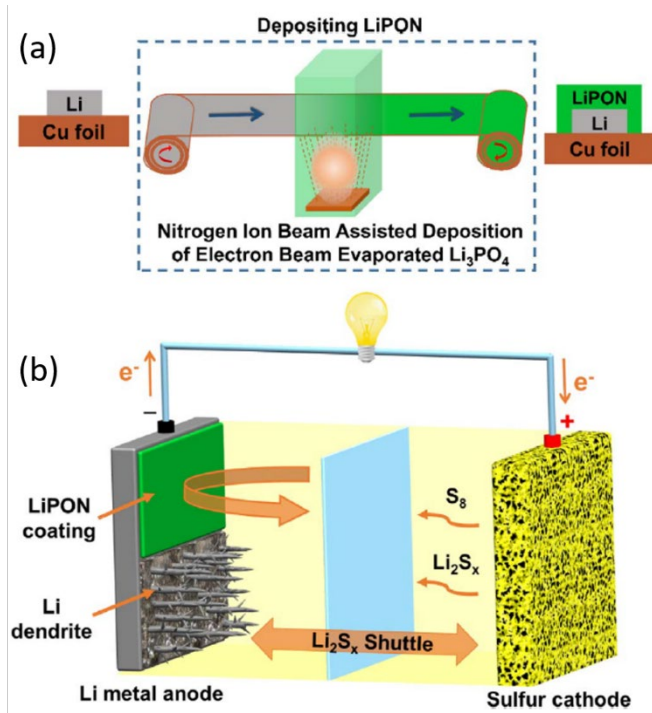


**Figure 1.13** Schematic of (a) the mass production of LiPON-coated Li metal foils and (b) the cycling processes of a LiPON-coated Li metal anode or bare lithium metal anode in Li-S battery configurations. Reproduced from ref. 127 with permission from Elsevier, Copyright 2019.

3. Nanocarbon in the anode. Huang et al. proposed a creative lithium–sulphur battery using an electrically connected graphite as lithium host to eliminate the dendrite growth and suppress the surface side reactions on Li metal.<sup>128</sup> A lithiated graphite layer in front of the lithium metal acted as an artificial and self-regulated SEI layer that can effectively suppress the dendrite growth and minimize the side reactions, rendering a dramatic performance improvement. Li-S batteries operating with this hybrid anode shows capacities of  $> 800 \text{ mA h g}^{-1}$  for 400 cycles under a high current density of  $1737 \text{ mA g}^{-1}$ , with 89% capacity retention and a Coulombic efficiency  $> 99\%$ . This simple and hybrid concept may also provide technical protocols for protecting metal anodes in other energy-storage devices.

4. Solid-state electrolytes are also promising candidates for all-solid-state Li-S batteries. Particularly, sulfide electrolytes, such as glass-type  $P_2S_5-Li_2S$  or argyrodites, which have similar chemical potential with sulfur or sulfide cathode materials could achieve a rechargeable Li-S battery with lower interfacial resistance.<sup>129</sup> Tao and his coworkers proposed a solid-state Li-S battery which can achieve a high capacity of  $900 \text{ mA h g}^{-1}$  under the temperature of  $37^\circ\text{C}$  with a LLZO coating layer on S using LLZO and Poly(ethylene oxide) (PEO) composite electrolyte.<sup>130</sup> Yamada et al. used the glass-type  $P_2S_5-Li_2S$  as the SSE for all-solid-state Li-S batteries which shows a high capacity of  $1600 \text{ mA h g}^{-1}$  in the first cycle with a high coulombic efficiency of 99%.<sup>131</sup>

### 1.6 Work in this thesis

To summarize, a major challenge for lithium metal batteries is the low efficiency of electrochemical Li-metal plating and stripping, which is due to the mutual amplification of dendritic/mossy Li-metal growth and the electrolyte decomposition reactions that occur upon contact with Li-metal. This thesis aims to search effective methods to suppress and eliminate lithium dendrites in both liquid and solid-state electrolytes for the development of safe and high-energy-density lithium metal batteries.

In **Chapter 2**, we investigate the impact of a high dielectric porous scaffold, aiming to take away the fundamental driver for dendritic and mossy Li-metal growth, the large electrical field gradients at the inhomogeneities of the anode surface. In a Li-metal free high dielectric porous scaffold, thus an anode-less configuration, this promotes dense plating in the porous scaffold as observed by operando solid-state NMR. Even in a simple carbonate electrolyte, 1M LiPF<sub>6</sub> in EC/DMC, this improves the plating/stripping efficiency drastically up to 99.82%, extending the cycle life, indicating that electrolyte decomposition is minimized by the high dielectric induced compact Li-metal plating. The large porosity of these non-optimized and easy to prepare scaffolds enables a specific capacity exceeding  $2000 \text{ mA h g}^{-1}$ , including the high dielectric scaffold weight. Thereby the impact of the high dielectric scaffold on Li-metal plating is demonstrated, confiscating the driving force of dendritic/mossy Li-metal growth, presenting a facile approach to promote compact Li-metal plating to improve Li-metal anode efficiency and safety.

In **Chapter 3**, a 3D high dielectric matrix for solid-state Li metal battery was studied to optimize the focused electric field and intrinsically alleviate the dendrites growth. Symmetrical Li-metal cycling in this barium titanate (BTO) based high dielectric skeleton results in an ultra-small overpotential of 48 mV at high current densities of  $1 \text{ mA cm}^{-2}$  for  $2 \text{ mA h cm}^{-2}$  over 1700 hours. Moreover, much higher Coulombic efficiency of full cells with

this 3D matrix was achieved, which proved successful in restricting the electrolyte decomposition, as examined by solid-state NMR, which is crucial to improve solid-state battery performance. Above, results show promise for the practical application of composite Li metal anodes with solid electrolytes for the development of all-solid-state batteries.

In **Chapter 4**, we explore a potential strategy to improve the hybrid solid electrolyte (HSE)/Cu interface by introducing a 100-nm thin film of ZnO on the copper current collector with atomic layer deposition (ALD), effectively making the current collector lithium-philic. During the first charge, this results in more homogeneous lithium-metal growth, rationalized by the formation of a Zn–Li alloy that acts as seed crystals for the lithium metal. The resulting more-homogeneous lithium-metal growth maintains better contact with the solid electrolyte, leading to more reversible cycling of lithium metal. Minor prelithiating of the ZnO/Cu anode with  $1 \text{ mA h cm}^{-2}$  further improves the cycling performance, as demonstrated in a full all-solid-state cell using  $\text{LiFePO}_4$  as a cathode, resulting in an average Coulombic efficiency of  $>95\%$ . These findings mark the first steps in an interface strategy to overcome the challenges at the solid electrolyte/lithium-metal interface in solid-state lithium-metal batteries.

In **Chapter 5**, we propose a simple solvent method to deposit  $\text{LiI}$  at the interfaces between the sulphur cathode and the argyrodite solid electrolyte to achieve facile Li-ion transport in combination with improved stability in solid-state-batteries. Two-dimensional exchange NMR reveals that  $\text{LiI}$  enhances the  $\text{Li}^+$  transfer between the sulphur cathode and solid electrolyte. This allows the abandonment of commonly applied nanosizing approaches that compromise the stability over extended battery cycling. The improved interface stability and ionic transport enables facile sulphur activation and prevents argyrodite solid electrolyte decomposition. This results in a cycling capacity of  $600 \text{ mA h g}^{-1}$  for more than 100 cycles with an average Coulombic efficiency of 99.2% under mild pressure conditions (2MPa). Thereby the present low contact area interface strategy unites facile  $\text{Li}^+$  transportation and stability, enhancing the solid-state battery performance.

## References

1. Tarascon, J.-M.; Armand, M., Issues and challenges facing rechargeable lithium batteries. In *Materials for sustainable energy: a collection of peer-reviewed research and review articles from Nature Publishing Group* World Scientific: 2011; pp 171-179.
2. Evarts, E. C., Lithium batteries: To the limits of lithium. *Nature* **2015**, 526 (7575), S93.



- Etacheri, V.; Marom, R.; Elazari, R.; Salitra, G.; Aurbach, D., Challenges in the development of advanced Li-ion batteries: a review. *Energy Environ. Sci.* **2011**, *4* (9), 3243-3262.
- Palacin, M. R.; de Guibert, A., Why do batteries fail? *Science* **2016**, *351* (6273), 1253292.
- Lin, D.; Liu, Y.; Cui, Y., Reviving the lithium metal anode for high-energy batteries. *Nat. Nanotech.* **2017**, *12* (3), 194-206.
- Armand, M.; Tarascon, J.-M., Building better batteries. *Nature* **2008**, *451*, 652-657.
- Wang, D.; Zhang, W.; Zheng, W.; Cui, X.; Rojo, T.; Zhang, Q., Towards high-safe lithium metal anodes: suppressing lithium dendrites via tuning surface energy. *Adv. Sci.* **2017**, *4* (1), 1600168.
- Mukhopadhyay, A.; Jangid, M. K., Li metal battery, heal thyself. *Science* **2018**, *359* (6383), 1463.
- Albertus, P.; Babinec, S.; Litzelman, S.; Newman, A., Status and challenges in enabling the lithium metal electrode for high-energy and low-cost rechargeable batteries. *Nat. Energy* **2017**, *3* (1), 16-21.
- Cheng, X. B.; Zhang, R.; Zhao, C. Z.; Wei, F.; Zhang, J. G.; Zhang, Q., A review of solid electrolyte interphases on lithium metal anode. *Adv. Sci.* **2016**, *3* (3), 1500213.
- Tarascon, J.-M.; Armand, M., Issues and challenges facing rechargeable lithium batteries. *Nature* **2001**, *414*, 359-367.
- Zhang, X.; Wang, A.; Liu, X.; Luo, J., Dendrites in lithium metal anodes: suppression, regulation, and elimination. *Acc. Chem. Res.* **2019**, *52* (11), 3223-3232.
- Xu, W.; Wang, J.; Ding, F.; Chen, X.; Nasybulin, E.; Zhang, Y.; Zhang, J.-G., Lithium metal anodes for rechargeable batteries. *Energy Environ. Sci.* **2014**, *7* (2), 513-537.
- Yang, C.; Fu, K.; Zhang, Y.; Hitz, E.; Hu, L., Protected lithium-metal anodes in batteries: from liquid to solid. *Adv. Mater.* **2017**, *29* (36), 1701169.
- Han, F.; Westover, A. S.; Yue, J.; Fan, X.; Wang, F.; Chi, M.; Leonard, D. N.; Dudney, N. J.; Wang, H.; Wang, C., High electronic conductivity as the origin of lithium dendrite formation within solid electrolytes. *Nat. Energy* **2019**, *4* (3), 187-196.
- Chazalviel, J.-N., Electrochemical aspects of the generation of ramified metallic electrodeposits. *Phys. Rev. A* **1990**, *42* (12), 7355.

17. Ely, D. R.; García, R. E., Heterogeneous nucleation and growth of lithium electrodeposits on negative electrodes. *J. Electrochem. Soc.* **2013**, *160* (4), A662.
18. Yamaki, J.-i.; Tobishima, S.-i.; Hayashi, K.; Saito, K.; Nemoto, Y.; Arakawa, M., A consideration of the morphology of electrochemically deposited lithium in an organic electrolyte. *J. Power Sources* **1998**, *74* (2), 219-227.
19. Wang, X.; Zeng, W.; Hong, L.; Xu, W.; Yang, H.; Wang, F.; Duan, H.; Tang, M.; Jiang, H., Stress-driven lithium dendrite growth mechanism and dendrite mitigation by electroplating on soft substrates. *Nat. Energy* **2018**, *3* (3), 227.
20. Yang, C.; Fu, K.; Zhang, Y.; Hitz, E.; Hu, L., Protected lithium-metal anodes in batteries: from liquid to solid. *Adv. Mater.* **2017**, *29* (36), 1701169.
21. Liang, Z.; Lin, D.; Zhao, J.; Lu, Z.; Liu, Y.; Liu, C.; Lu, Y.; Wang, H.; Yan, K.; Tao, X., Composite lithium metal anode by melt infusion of lithium into a 3D conducting scaffold with lithiophilic coating. *Proc. Natl. Acad. Sci.* **2016**, *113* (11), 2862-2867.
22. Zhang, R.; Li, N. W.; Cheng, X. B.; Yin, Y. X.; Zhang, Q.; Guo, Y. G., Advanced micro/nanostructures for lithium metal anodes. *Adv. Sci.* **2017**, *4* (3), 1600445.
23. Liu, S.; Wang, A.; Li, Q.; Wu, J.; Chiou, K.; Huang, J.; Luo, J., Crumpled graphene balls stabilized dendrite-free lithium metal anodes. *Joule* **2018**, *2* (1), 184-193.
24. Yun, Q.; He, Y. B.; Lv, W.; Zhao, Y.; Li, B.; Kang, F.; Yang, Q. H., Chemical dealloying derived 3D porous current collector for Li metal anodes. *Adv. Mater.* **2016**, *28* (32), 6932-6939.
25. Cheng, X.-B.; Zhang, R.; Zhao, C.-Z.; Zhang, Q., Toward safe lithium metal anode in rechargeable batteries: a review. *Chem. Rev.* **2017**, *117* (15), 10403-10473.
26. Liu, Y.; Liu, Q.; Xin, L.; Liu, Y.; Yang, F.; Stach, E. A.; Xie, J., Making Li-metal electrodes rechargeable by controlling the dendrite growth direction. *Nat. Energy* **2017**, *2* (7), 1-10.
27. Zhao, Y.; Amirmaleki, M.; Sun, Q.; Zhao, C.; Codireenzi, A.; Goncharova, L. V.; Wang, C.; Adair, K.; Li, X.; Yang, X., Natural SEI-inspired dual-protective layers via atomic/molecular layer deposition for long-life metallic lithium anode. *Matter* **2019**, *1* (5), 1215-1231.

28. Yang, C.-P.; Yin, Y.-X.; Zhang, S.-F.; Li, N.-W.; Guo, Y.-G., Accommodating lithium into 3D current collectors with a submicron skeleton towards long-life lithium metal anodes. *Nat. Commun.* **2015**, *6* (1), 1-9.
29. Zhang, Y.; Luo, W.; Wang, C.; Li, Y.; Chen, C.; Song, J.; Dai, J.; Hitz, E. M.; Xu, S.; Yang, C., High-capacity, low-tortuosity, and channel-guided lithium metal anode. *Proc. Natl. Acad. Sci.* **2017**, *114* (14), 3584-3589.
30. Barton, J. L.; Bockris, J. O. M., The electrolytic growth of dendrites from ionic solutions. *Proceedings of the Royal Society of London. Series A. Math. Phys. Sci.* **1962**, *268* (1335), 485-505.
31. Xu, W.; Wang, J.; Ding, F.; Chen, X.; Nasybulin, E.; Zhang, Y.; Zhang, J.-G., Lithium metal anodes for rechargeable batteries. *Energy Environ. Sci.* **2014**, *7* (2), 513-537.
32. Wang, A.; Deng, Q.; Deng, L.; Guan, X.; Luo, J., Eliminating tip dendrite growth by Lorentz force for stable lithium metal anodes. *Adv. Funct. Mater.* **2019**, *29* (25), 1902630.
33. Shen, K.; Wang, Z.; Bi, X.; Ying, Y.; Zhang, D.; Jin, C.; Hou, G.; Cao, H.; Wu, L.; Zheng, G., Magnetic field-suppressed lithium dendrite growth for stable lithium-metal batteries. *Adv. Energy Mater.* **2019**, *9* (20), 1900260.
34. Koch, C.; Langdon, T.; Lavernia, E., Bulk nanostructured materials. *Metall. Mater. Trans. A* **2017**, *48* (11), 5181-5199.
35. Fan, L.; Li, S.; Liu, L.; Zhang, W.; Gao, L.; Fu, Y.; Chen, F.; Li, J.; Zhuang, H. L.; Lu, Y., Enabling stable lithium metal anode via 3D inorganic skeleton with superlithiophilic interphase. *Adv. Energy Mater.* **2018**, *8* (33), 1802350.
36. Lee, J.; Kitchaev, D. A.; Kwon, D.-H.; Lee, C.-W.; Papp, J. K.; Liu, Y.-S.; Lun, Z.; Clément, R. J.; Shi, T.; McCloskey, B. D., Reversible  $Mn^{2+}/Mn^{4+}$  double redox in lithium-excess cathode materials. *Nature* **2018**, *556* (7700), 185-190.
37. Wang, X.; Zhuang, J.; Liu, M.; Wang, C.; Zhong, Y.; Wang, H.; Cheng, X.; Liu, S.; Cao, G.; Li, W., Facile and scalable engineering of a heterogeneous microstructure for uniform, stable and fast lithium plating/stripping. *J. Mater. Chem. A* **2019**, *7* (32), 19104-19111.
38. Zhang, H.; Liao, X.; Guan, Y.; Xiang, Y.; Li, M.; Zhang, W.; Zhu, X.; Ming, H.; Lu, L.; Qiu, J., Lithiophilic-lithiophobic gradient interfacial layer for a highly stable lithium metal anode. *Nat. Commun.* **2018**, *9* (1), 1-11.

39. Liao, K.; Wu, S.; Mu, X.; Lu, Q.; Han, M.; He, P.; Shao, Z.; Zhou, H., Developing a “Water-defendable” and “Dendrite-free” lithium-metal anode using a simple and promising  $\text{GeCl}_4$  pretreatment method. *Adv. Mater.* **2018**, *30* (36), 1705711.
40. Xu, Y.; Li, T.; Wang, L.; Kang, Y., Interlayered dendrite-free lithium plating for high-performance lithium-metal batteries. *Adv. Mater.* **2019**, *31* (29), 1901662.
41. Zhou, B.; Guo, L.; Zhang, Y.; Wang, J.; Ma, L.; Zhang, W. H.; Fu, Z.; Peng, Z., A high-performance  $\text{Li-O}_2$  battery with a strongly solvating hexamethylphosphoramide electrolyte and a LiPON-protected lithium anode. *Adv. Mater.* **2017**, *29* (30), 1701568.
42. Jiao, S.; Ren, X.; Cao, R.; Engelhard, M. H.; Liu, Y.; Hu, D.; Mei, D.; Zheng, J.; Zhao, W.; Li, Q., Stable cycling of high-voltage lithium metal batteries in ether electrolytes. *Nat. Energy* **2018**, *3* (9), 739-746.
43. Cheng, X.-B.; Zhao, M.-Q.; Chen, C.; Pentecost, A.; Maleski, K.; Mathis, T.; Zhang, X.-Q.; Zhang, Q.; Jiang, J.; Gogotsi, Y., Nanodiamonds suppress the growth of lithium dendrites. *Nat. Commun.* **2017**, *8* (1), 1-9.
44. Duan, J.; Wu, W.; Nolan, A. M.; Wang, T.; Wen, J.; Hu, C.; Mo, Y.; Luo, W.; Huang, Y., Lithium-graphite paste: An interface compatible anode for solid-state batteries. *Adv. Mater.* **2019**, *31* (10), 1807243.
45. Mauger, A.; Julien, C. M.; Paoletta, A.; Armand, M.; Zaghbi, K., Building better batteries in the solid state: a review. *Materials* **2019**, *12* (23), 3892.
46. Delaporte, N.; Guerfi, A.; Demers, H.; Lorrmann, H.; Paoletta, A.; Zaghbi, K., Facile Protection of lithium metal for all-solid-state batteries. *ChemistryOpen* **2019**, *8* (2), 192-195.
47. Xu, H.; Chien, P.-H.; Shi, J.; Li, Y.; Wu, N.; Liu, Y.; Hu, Y.-Y.; Goodenough, J. B., High-performance all-solid-state batteries enabled by salt bonding to perovskite in poly (ethylene oxide). *Proc. Natl. Acad. Sci.* **2019**, *116* (38), 18815-18821.
48. Hou, L.-P.; Yuan, H.; Zhao, C.-Z.; Xu, L.; Zhu, G.-L.; Nan, H.-X.; Cheng, X.-B.; Liu, Q.-B.; He, C.-X.; Huang, J.-Q., Improved interfacial electronic contacts powering high sulfur utilization in all-solid-state lithium-sulfur batteries. *Energy Stor. Mater.* **2020**, *25*, 436-442.
49. Samson, A. J.; Hofstetter, K.; Bag, S.; Thangadurai, V., A bird's-eye view of Li-stuffed garnet-type  $\text{Li}_7\text{La}_3\text{Zr}_2\text{O}_{12}$  ceramic electrolytes for advanced all-solid-state Li batteries. *Energy Environ. Sci.* **2019**, *12* (10), 2957-2975.

50. Cortes, F. J. Q.; Lewis, J. A.; Tippens, J.; Marchese, T. S.; McDowell, M. T., How metallic protection layers extend the lifetime of NASICON-based solid-state lithium batteries. *J. Electrochem. Soc.* **2019**, *167* (5), 050502.
51. Li, G.; Monroe, C. W., Dendrite nucleation in lithium-conductive ceramics. *Phys. Chem. Chem. Phys.* **2019**, *21* (36), 20354-20359.
52. Zhang, H.; Li, C.; Piszcz, M.; Coya, E.; Rojo, T.; Rodriguez-Martinez, L. M.; Armand, M.; Zhou, Z., Single lithium-ion conducting solid polymer electrolytes: advances and perspectives. *Chem. Soc. Rev.* **2017**, *46* (3), 797-815.
53. Monroe, C.; Newman, J., The impact of elastic deformation on deposition kinetics at lithium/polymer interfaces. *J. Electrochem. Soc.* **2005**, *152* (2), A396.
54. Ma, J.; Chen, B.; Wang, L.; Cui, G., Progress and prospect on failure mechanisms of solid-state lithium batteries. *J. Power Sources* **2018**, *392*, 94-115.
55. Albertus, P.; Babinec, S.; Litzelman, S.; Newman, A., Status and challenges in enabling the lithium metal electrode for high-energy and low-cost rechargeable batteries. *Nat. Energy* **2018**, *3* (1), 16-21.
56. Luo, C.; Ji, X.; Chen, J.; Gaskell, K. J.; He, X.; Liang, Y.; Jiang, J.; Wang, C., Solid-state electrolyte anchored with a carboxylated azo compound for all-solid-state lithium batteries. *Angew. Chem. Int. Ed.* **2018**, *57* (28), 8567-8571.
57. Liu, M.; Cheng, Z.; Ganapathy, S.; Wang, C.; Haverkate, L. A.; Tułodziecki, M.; Unnikrishnan, S.; Wagemaker, M., Tandem interface and bulk Li-Ion transport in a hybrid solid electrolyte with micro-sized active filler. *ACS Energy Lett.* **2019**, *4* (9), 2336-2342.
58. Liu, H.; Cheng, X.-B.; Huang, J.-Q.; Yuan, H.; Lu, Y.; Yan, C.; Zhu, G.-L.; Xu, R.; Zhao, C.-Z.; Hou, L.-P.; He, C.; Kaskel, S.; Zhang, Q., Controlling dendrite growth in solid-state electrolytes. *ACS Energy Lett.* **2020**, *5* (3), 833-843.
59. Zhao, C.; Liang, J.; Zhao, Y.; Luo, J.; Sun, Q.; Liu, Y.; Lin, X.; Yang, X.; Huang, H.; Zhang, L., Engineering a “nanonet”-reinforced polymer electrolyte for long-life Li-O<sub>2</sub> batteries. *J. Mater. Chem. A* **2019**, *7* (43), 24947-24952.
60. Wu, H.; Xu, Y.; Ren, X.; Liu, B.; Engelhard, M. H.; Ding, M. S.; El-Khoury, P. Z.; Zhang, L.; Li, Q.; Xu, K., Polymer-in-“quasi-ionic liquid” electrolytes for high-voltage lithium metal batteries. *Adv. Mater.* **2019**, *9* (41), 1902108.

61. Wang, C.; Wang, T.; Wang, L.; Hu, Z.; Cui, Z.; Li, J.; Dong, S.; Zhou, X.; Cui, G., Differentiated lithium salt design for multilayered PEO electrolyte enables a high-voltage solid-state lithium metal battery. *Adv. Sci.* **2019**, *6* (22), 1901036.
62. Onsager, L., Theories and problems of liquid diffusion. *Ann. N. Y. Acad. Sci.* **1945**, *46* (5), 241-265.
63. Barai, P.; Higa, K.; Srinivasan, V., Lithium dendrite growth mechanisms in polymer electrolytes and prevention strategies. *Phys. Chem. Chem. Phys.* **2017**, *19* (31), 20493-20505.
64. Bai, P.; Li, J.; Brushett, F. R.; Bazant, M. Z. J. E.; Science, E., Transition of lithium growth mechanisms in liquid electrolytes. *Energy Environ. Sci.* **2016**, *9* (10), 3221-3229.
65. Ahmad, Z.; Viswanathan, V., Stability of electrodeposition at solid-solid interfaces and implications for metal anodes. *Phys. Rev. Lett.* **2017**, *119* (5), 056003.
66. Li, S.; Mohamed, A. I.; Pande, V.; Wang, H.; Cuthbert, J.; Pan, X.; He, H.; Wang, Z.; Viswanathan, V.; Whitacre, J. F., Single-ion homopolymer electrolytes with high transference number prepared by click chemistry and photoinduced metal-free atom-transfer radical polymerization. *ACS Energy Lett.* **2017**, *3* (1), 20-27.
67. Cao, C.; Li, Y.; Feng, Y.; Peng, C.; Li, Z.; Feng, W., A solid-state single-ion polymer electrolyte with ultrahigh ionic conductivity for dendrite-free lithium metal batteries. *Energy Stor. Mater.* **2019**, *19*, 401-407.
68. Monroe, C.; Newman, J., The effect of interfacial deformation on electrodeposition kinetics. *J. Electrochem. Soc.* **2004**, *151* (6), A880.
69. Harry, K. J.; Higa, K.; Srinivasan, V.; Balsara, N. P., Influence of electrolyte modulus on the local current density at a dendrite tip on a lithium metal electrode. *J. Electrochem. Soc.* **2016**, *163* (10), A2216.
70. Geng, H.; Rosen, R.; Zheng, B.; Shimoda, H.; Fleming, L.; Liu, J.; Zhou, O., Fabrication and properties of composites of poly (ethylene oxide) and functionalized carbon nanotubes. *Adv. Mater.* **2002**, *14* (19), 1387-1390.
71. Rosso, M.; Brissot, C.; Teyssoit, A.; Dollé, M.; Sannier, L.; Tarascon, J.-M.; Bouchet, R.; Lascaud, S., Dendrite short-circuit and fuse effect on Li/polymer/Li cells. *Electrochim. Acta* **2006**, *51* (25), 5334-5340.

72. Dollé, M.; Sannier, L.; Beaudoin, B.; Trentin, M.; Tarascon, J.-M., Live scanning electron microscope observations of dendritic growth in lithium/polymer cells. *Electrochem. Solid-State Lett.* **2002**, *5* (12), A286.
73. Zhang, X.; Wang, S.; Xue, C.; Xin, C.; Lin, Y.; Shen, Y.; Li, L.; Nan, C. W., Self-suppression of lithium dendrite in all-solid-state lithium metal batteries with poly(vinylidene difluoride)-based solid electrolytes. *Adv. Mater.* **2019**, *31* (11), 1806082.
74. Brissot, C.; Rosso, M.; Chazalviel, J.-N.; Lascaud, S., Dendritic growth mechanisms in lithium/polymer cells. *J. Power Sources* **1999**, *81*, 925-929.
75. Rosso, M.; Gobron, T.; Brissot, C.; Chazalviel, J.-N.; Lascaud, S., Onset of dendritic growth in lithium/polymer cells. *J. Power Sources* **2001**, *97*, 804-806.
76. Harry, K. J.; Liao, X.; Parkinson, D. Y.; Minor, A. M.; Balsara, N. P., Electrochemical deposition and stripping behavior of lithium metal across a rigid block copolymer electrolyte membrane. *J. Electrochem. Soc.* **2015**, *162* (14), A2699.
77. Harry, K. J.; Hallinan, D. T.; Parkinson, D. Y.; MacDowell, A. A.; Balsara, N. P., Detection of subsurface structures underneath dendrites formed on cycled lithium metal electrodes. *Nat. Mater.* **2014**, *13* (1), 69-73.
78. Schausser, N. S.; Harry, K. J.; Parkinson, D. Y.; Watanabe, H.; Balsara, N. P., Lithium dendrite growth in glassy and rubbery nanostructured block copolymer electrolytes. *J. Electrochem. Soc.* **2014**, *162* (3), A398.
79. Sharafi, A.; Kazyak, E.; Davis, A. L.; Yu, S.; Thompson, T.; Siegel, D. J.; Dasgupta, N. P.; Sakamoto, J., Surface chemistry mechanism of ultra-low interfacial resistance in the solid-state electrolyte  $\text{Li}_7\text{La}_3\text{Zr}_2\text{O}_{12}$ . *Chem. Mater.* **2017**, *29* (18), 7961-7968.
80. Xie, H.; Bao, Y.; Cheng, J.; Wang, C.; Hitz, E. M.; Yang, C.; Liang, Z.; Zhou, Y.; He, S.; Li, T., Flexible garnet solid-state electrolyte membranes enabled by tile-and-grout design. *ACS Energy Lett.* **2019**, *4* (11), 2668-2674.
81. Li, Q.; Yi, T.; Wang, X.; Pan, H.; Quan, B.; Liang, T.; Guo, X.; Yu, X.; Wang, H.; Huang, X., In-situ visualization of lithium plating in all-solid-state lithium-metal battery. *Nano Energy* **2019**, *63*, 103895.
82. Wang, S.; Xu, H.; Li, W.; Dolocan, A.; Manthiram, A., Interfacial chemistry in solid-state batteries: formation of interphase and its consequences. *J. Am. Chem. Soc.* **2018**, *140* (1), 250-257.

83. Han, F.; Yue, J.; Zhu, X.; Wang, C., Suppressing Li dendrite formation in  $\text{Li}_2\text{S-P}_2\text{S}_5$  solid electrolyte by LiI incorporation. *Adv. Energy Mater.* **2018**, 8 (18), 1703644.
84. Raj, R.; Wolfenstine, J., Current limit diagrams for dendrite formation in solid-state electrolytes for Li-ion batteries. *J. Power Sources* **2017**, 343, 119-126.
85. Ansell, R. O., The chemical and electrochemical stability of beta-alumina. *J. Mater. Sci.* **1986**, 21, 365-379.
86. Sharafi, A.; Yu, S.; Naguib, M.; Lee, M.; Ma, C.; Meyer, H. M.; Nanda, J.; Chi, M.; Siegel, D. J.; Sakamoto, J., Impact of air exposure and surface chemistry on  $\text{Li-Li}_7\text{La}_3\text{Zr}_2\text{O}_{12}$  interfacial resistance. *J. Mater. Chem. A* **2017**, 5 (26), 13475-13487.
87. Yu, S.; Siegel, D. J., Grain boundary softening: a potential mechanism for lithium metal penetration through stiff solid electrolytes. *ACS Appl. Mater. Interfaces* **2018**, 10 (44), 38151-38158.
88. Han, X.; Gong, Y.; Fu, K. K.; He, X.; Hitz, G. T.; Dai, J.; Pearse, A.; Liu, B.; Wang, H.; Rubloff, G., Negating interfacial impedance in garnet-based solid-state Li metal batteries. *Nat. Mater.* **2017**, 16 (5), 572-579.
89. Adams, J. B.; Wolfer, W. G.; Foiles, S. M., Elastic properties of grain boundaries in copper and their relationship to bulk elastic constants. *Phys. Rev. B* **1989**, 40 (14), 9479.
90. Lewis, J. A.; Tippens, J.; Cortes, F. J. Q.; McDowell, M. T., Chemo-mechanical challenges in solid-state batteries. *Trends Chem.* **2019**, 1 (9), 845-857.
91. Cheng, E. J.; Sharafi, A.; Sakamoto, J., Intergranular Li metal propagation through polycrystalline  $\text{Li}_{6.25}\text{Al}_{0.25}\text{La}_3\text{Zr}_2\text{O}_{12}$  ceramic electrolyte. *Electrochim. Acta* **2017**, 223, 85-91.
92. Yu, S.; Siegel, D. J., Grain boundary contributions to Li-ion transport in the solid electrolyte  $\text{Li}_7\text{La}_3\text{Zr}_2\text{O}_{12}$  (LLZO). *Chem. Mater.* **2017**, 29 (22), 9639-9647.
93. Dawson, J. A.; Canepa, P.; Famprakis, T.; Masquelier, C.; Islam, M. S., Atomic-scale influence of grain boundaries on Li-ion conduction in solid electrolytes for all-solid-state batteries. *J. Am. Chem. Soc.* **2018**, 140 (1), 362-368.
94. Ren, Y.; Shen, Y.; Lin, Y.; Nan, C.-W., Direct observation of lithium dendrites inside garnet-type lithium-ion solid electrolyte. *Electrochem. Commun.* **2015**, 57, 27-30.



95. Pesci, F. M.; Brugge, R. H.; Hekselman, A. O.; Cavallaro, A.; Chater, R. J.; Aguadero, A., Elucidating the role of dopants in the critical current density for dendrite formation in garnet electrolytes. *J. Mater. Chem. A* **2018**, *6* (40), 19817-19827.
96. Im, C.; Park, D.; Kim, H.; Lee, J., Al-incorporation into  $\text{Li}_7\text{La}_3\text{Zr}_2\text{O}_{12}$  solid electrolyte keeping stabilized cubic phase for all-solid-state Li batteries. *J. Energy Chem.* **2018**, *27* (5), 1501-1508.
97. Li, Y.; Chen, X.; Dolocan, A.; Cui, Z.; Xin, S.; Xue, L.; Xu, H.; Park, K.; Goodenough, J. B., Garnet electrolyte with an ultralow interfacial resistance for Li-metal batteries. *J. Am. Chem. Soc.* **2018**, *140* (20), 6448-6455.
98. Ban, C. W.; Choi, G. M., The effect of sintering on the grain boundary conductivity of lithium lanthanum titanates. *Solid State Ion.* **2001**, *140* (3-4), 285-292.
99. David, I. N.; Thompson, T.; Wolfenstine, J.; Allen, J. L.; Sakamoto, J., Microstructure and Li-ion conductivity of hot-pressed cubic  $\text{Li}_7\text{La}_3\text{Zr}_2\text{O}_{12}$ . *J. Am. Chem. Soc.* **2015**, *98* (4), 1209-1214.
100. Chung, H.; Kang, B., Increase in grain boundary ionic conductivity of  $\text{Li}_{1.5}\text{Al}_{0.5}\text{Ge}_{1.5}(\text{PO}_4)_3$  by adding excess lithium. *Solid State Ion.* **2014**, *263*, 125-130.
101. Krauskopf, T.; Mogwitz, B.; Rosenbach, C.; Zeier, W. G.; Janek, J., Diffusion limitation of lithium metal and Li-Mg alloy anodes on LLZO type solid electrolytes as a function of temperature and pressure. *Adv. Energy Mater.* **2019**, *9* (44), 1902568.
102. Swamy, T.; Park, R.; Sheldon, B. W.; Rettenwander, D.; Porz, L.; Berendts, S.; Uecker, R.; Carter, W. C.; Chiang, Y.-M., Lithium metal penetration induced by electrodeposition through solid electrolytes: example in single-crystal  $\text{Li}_6\text{La}_3\text{ZrTaO}_{12}$  garnet. *J. Electrochem. Soc.* **2018**, *165* (16), A3648.
103. Klinsmann, M.; Hildebrand, F. E.; Ganser, M.; McMeeking, R. M., Dendritic cracking in solid electrolytes driven by lithium insertion. *J. Power Sources* **2019**, *442*, 227226.
104. Liu, H.; Cheng, X. B.; Xu, R.; Zhang, X. Q.; Yan, C.; Huang, J. Q.; Zhang, Q., Plating/stripping behavior of actual lithium metal anode. *Adv. Energy Mater.* **2019**, *9* (44), 1902254.
105. Kasemchainan, J.; Zekoll, S.; Spencer Jolly, D.; Ning, Z.; Hartley, G. O.; Marrow, J.; Bruce, P. G., Critical stripping current leads to dendrite formation on plating in lithium anode solid electrolyte cells. *Nat. Mater.* **2019**, *18* (10), 1105-1111.

106. Lu, Y.; Huang, X.; Song, Z.; Rui, K.; Wang, Q.; Gu, S.; Yang, J.; Xiu, T.; Badding, M. E.; Wen, Z., Highly stable garnet solid electrolyte based Li-S battery with modified anodic and cathodic interfaces. *Energy Stor. Mater.* **2018**, *15*, 282-290.
107. Lu, Y.; Huang, X.; Ruan, Y.; Wang, Q.; Kun, R.; Yang, J.; Wen, Z., An in situ element permeation constructed high endurance Li-LLZO interface at high current densities. *J. Mater. Chem. A* **2018**, *6* (39), 18853-18858.
108. Liu, G.; Weng, W.; Zhang, Z.; Wu, L.; Yang, J.; Yao, X., Densified Li<sub>6</sub>PS<sub>5</sub>Cl nanorods with high ionic conductivity and improved critical current density for all-solid-state lithium batteries. *Nano Lett.* **2020**, *20* (9), 6660-6665.
109. Song, Y.; Yang, L.; Zhao, W.; Wang, Z.; Zhao, Y.; Wang, Z.; Zhao, Q.; Liu, H.; Pan, F., Revealing the short-circuiting mechanism of garnet-based solid-state electrolyte. *Adv. Energy Mater.* **2019**, *9* (21), 1900671.
110. Cheng, X.-B.; Yan, C.; Zhang, X.-Q.; Liu, H.; Zhang, Q., Electronic and ionic channels in working interfaces of lithium metal anodes. *ACS Energy Lett.* **2018**, *3* (7), 1564-1570.
111. Mo, F.; Ruan, J.; Sun, S.; Lian, Z.; Yang, S.; Yue, X.; Song, Y.; Zhou, Y. N.; Fang, F.; Sun, G., Inside or outside: origin of lithium dendrite formation of all solid-state electrolytes. *Adv. Energy Mater.* **2019**, *9* (40), 1902123.
112. Wenzel, S.; Leichtweiss, T.; Krüger, D.; Sann, J.; Janek, J., Interphase formation on lithium solid electrolytes-An in situ approach to study interfacial reactions by photoelectron spectroscopy. *Solid State Ion.* **2015**, *278*, 98-105.
113. Pervez, S. A.; Cambaz, M. A.; Thangadurai, V.; Fichtner, M., Interface in solid-state lithium battery: challenges, progress, and outlook. *ACS Appl. Mater. Interfaces* **2019**, *11* (25), 22029-22050.
114. Chen, S.; Xie, D.; Liu, G.; Mwiszerwa, J. P.; Zhang, Q.; Zhao, Y.; Xu, X.; Yao, X., Sulfide solid electrolytes for all-solid-state lithium batteries: structure, conductivity, stability and application. *Energy Stor. Mater.* **2018**, *14*, 58-74.
115. Lewis, J. A.; Cortes, F. J. Q.; Boebinger, M. G.; Tippens, J.; Marchese, T. S.; Kondekar, N.; Liu, X.; Chi, M.; McDowell, M. T., Interphase morphology between a solid-state electrolyte and lithium controls cell failure. *ACS Energy Lett.* **2019**, *4* (2), 591-599.
116. Tippens, J.; Miers, J. C.; Afshar, A.; Lewis, J. A.; Cortes, F. J. Q.; Qiao, H.; Marchese, T. S.; Di Leo, C. V.; Saldana, C.; McDowell, M. T., Visualizing chemomechanical

- degradation of a solid-state battery electrolyte. *ACS Energy Lett.* **2019**, *4* (6), 1475-1483.
117. Liang, X.; Rangom, Y.; Kwok, C. Y.; Pang, Q.; Nazar, L. F., Interwoven MXene nanosheet/carbon-nanotube composites as Li-S cathode hosts. *Adv. Mater.* **2017**, *29* (3), 1603040.
118. Wu, F.; Yushin, G., Conversion cathodes for rechargeable lithium and lithium-ion batteries. *Energy Environ. Sci.* **2017**, *10* (2), 435-459.
119. Luo, C.; Hu, E.; Gaskell, K. J.; Fan, X.; Gao, T.; Cui, C.; Ghose, S.; Yang, X.-Q.; Wang, C., A chemically stabilized sulfur cathode for lean electrolyte lithium sulfur batteries. *Proc. Natl. Acad. Sci.* **2020**, *117* (26), 14712-14720.
120. Zhao, M.; Li, B.-Q.; Zhang, X.-Q.; Huang, J.-Q.; Zhang, Q., A perspective toward practical lithium-sulfur batteries. *ACS Cent. Sci.* **2020**, *6* (7), 1095-1104.
121. Liu, F.; Sun, G.; Wu, H. B.; Chen, G.; Xu, D.; Mo, R.; Shen, L.; Li, X.; Ma, S.; Tao, R., Dual redox mediators accelerate the electrochemical kinetics of lithium-sulfur batteries. *Nat. Commun.* **2020**, *11* (1), 1-10.
122. Hu, A.; Zhou, M.; Lei, T.; Hu, Y.; Du, X.; Gong, C.; Shu, C.; Long, J.; Zhu, J.; Chen, W., Optimizing redox reactions in aprotic lithium-sulfur batteries. *Adv. Energy Mater.* **2020**, *10* (42), 2002180.
123. Wang, J.; Yi, S.; Liu, J.; Sun, S.; Liu, Y.; Yang, D.; Xi, K.; Gao, G.; Abdelkader, A.; Yan, W., Suppressing the shuttle effect and dendrite growth in lithium-sulfur batteries. *ACS Nano* **2020**, *14* (8), 9819-9831.
124. Aurbach, D.; Pollak, E.; Elazari, R.; Salitra, G.; Kelley, C. S.; Affinito, J., On the surface chemical aspects of very high energy density, rechargeable Li-sulfur batteries. *J. Electrochem. Soc.* **2009**, *156* (8), A694.
125. Zhang, S. S. J. E. A., Role of LiNO<sub>3</sub> in rechargeable lithium/sulfur battery. *Electrochim. Acta* **2012**, *70*, 344-348.
126. Cao, Y.; Meng, X.; Elam, J. W., Atomic layer deposition of Li<sub>x</sub>Al<sub>y</sub>S solid-state electrolytes for stabilizing lithium-metal anodes. *ChemElectroChem* **2016**, *3* (6), 858-863.
127. Wang, W.; Yue, X.; Meng, J.; Wang, J.; Wang, X.; Chen, H.; Shi, D.; Fu, J.; Zhou, Y.; Chen, J., Lithium phosphorus oxynitride as an efficient protective layer on lithium

- metal anodes for advanced lithium-sulfur batteries. *Energy Stor. Mater.* **2019**, *18*, 414-422.
128. Huang, C.; Xiao, J.; Shao, Y.; Zheng, J.; Bennett, W. D.; Lu, D.; Saraf, L. V.; Engelhard, M.; Ji, L.; Zhang, J., Manipulating surface reactions in lithium-sulphur batteries using hybrid anode structures. *Nat. Commun.* **2014**, *5* (1), 1-8.
129. Xia, S.; Wu, X.; Zhang, Z.; Cui, Y.; Liu, W., Practical challenges and future perspectives of all-solid-state lithium-metal batteries. *Chem* **2019**, *5* (4), 753-785.
130. Tao, X.; Liu, Y.; Liu, W.; Zhou, G.; Zhao, J.; Lin, D.; Zu, C.; Sheng, O.; Zhang, W.; Lee, H.-W., Solid-state lithium-sulfur batteries operated at 37 °C with composites of nanostructured  $\text{Li}_7\text{La}_3\text{Zr}_2\text{O}_{12}$ /carbon foam and polymer. *Nano Lett.* **2017**, *17* (5), 2967-2972.
131. Yamada, T.; Ito, S.; Omoda, R.; Watanabe, T.; Aihara, Y.; Agostini, M.; Ulissi, U.; Hassoun, J.; Scrosati, B., All solid-state lithium-sulfur battery using a glass-type  $\text{P}_2\text{S}_5$ - $\text{Li}_2\text{S}$  electrolyte: benefits on anode kinetics. *J. Electrochem. Soc.* **2015**, *162* (4), A646.



## Chapter 2 High Dielectric 3D Scaffold to Suppress Lithium-Dendrites and Increase the Reversibility of Anode-less Lithium-Metal Anodes

**This chapter is based on:**

**Chao Wang**, Ming Liu, Michel Thijs, Frans G.B. Ooms, Swapna Ganapathy and Marnix Wagemaker, High Dielectric 3D Scaffold to Suppress Lithium-Dendrites and Increase the Reversibility of Anode-less Lithium-Metal Anodes, Submitted.

### Abstract

The lithium metal anode is intensively investigated because it considerably increases Li-battery energy density. However, the formation of dendritic/mossy Li-metal microstructures amplifies electrolyte decomposition and Li deactivation. Here we investigate the impact of a high-dielectric porous scaffold, aiming to eliminate the fundamental driver for dendritic/mossy Li-metal growth, the large electrical field gradients at inhomogeneities at the anode surface. In an anode-less (Li-metal free) high-dielectric porous scaffold, this promotes dense plating as observed by operando solid-state NMR. Even in a simple carbonate electrolyte, 1M LiPF<sub>6</sub> in EC/DMC, the high-dielectric scaffold improves the plating/stripping efficiency up to 99.82%, extending the cycle life, indicating that electrolyte decomposition is minimized by the induced compact Li-metal plating. The large porosity of the scaffolds, non-optimized and easy to prepare, enables a specific capacity beyond 2000 mA h g<sup>-1</sup>, presenting a facile approach to promote compact Li-metal plating to improve Li-metal anode efficiency and safety.

### 2.1 Introduction

The development of high energy density batteries beyond current Li-ion battery technology is necessary to meet the increasing demand for mobile applications such as electric vehicles.<sup>1-5</sup> Lithium metal is considered the ultimate anode material because it possesses the highest theoretical specific capacity,  $3860 \text{ mA h g}^{-1}$ , approximately ten times that of current graphite-based anodes, and low redox potential that endows it with a high battery output voltage ( $-3.040 \text{ V}$  vs standard hydrogen electrode).<sup>6-10</sup> However, upon repeated battery charging and discharging, the plating and stripping of Li-metal induces irreversible processes that lead to fast capacity decay which drastically limits the Li-metal battery cycle life.<sup>6-10</sup> The formation of high surface area dendritic and mossy Li-metal morphologies, in combination with the vicious reactivity of Li-metal towards common electrolytes, leads to an irreversible loss of active Li towards solid electrolyte interface products as well as the formation of inactive Li-metal. The latter is often referred to as “dead” Li, which has lost contact with the current collector.<sup>11-14</sup> Additionally, dendritic structures may penetrate the separator/electrolyte and reach the cathode, causing an internal short-circuit that may induce rapid spontaneous discharge and consequential safety hazards.<sup>6-10</sup> Loss of active Li is in research cells often masked by the excess of Li-metal present, but in practical cells, the amount of excess Li should be minimized to maximize the energy density.<sup>15</sup> Ultimately, all active Li is stored in the cathode in the discharged state. This so-called “anode-less” or “anode free” design, has the additional advantage of not necessitating Li-metal handling.

Strategies that aim to suppress, prevent and block dendrite formation are intensively investigated,<sup>6-10,16,17</sup> typically guided by our current understanding of dendrite nucleation and growth. The space charge model of Chazalviel predicts that when the Li-ion concentration on the surface of the anode drops to zero, after the characteristic Sand’s time, plating becomes inhomogeneous and self-amplified growth of dendrites is induced.<sup>18</sup> This motivates the use of strategies that enhance ion mobility, increase the transference number and introduce a large anode surface area to promote a homogenous Li-ion flux and to prevent ion depletion at the anode surface.<sup>6-10,16,17</sup> Modelling of the early stages of nucleation and growth under heterogeneous electrodeposition indicates that the anode surface inhomogeneities, particle size and wettability play a critical role in facilitating dendrite formation.<sup>19</sup> This implies that dendrite growth can be steered by controlling these parameters on the anode, as experimentally demonstrated.<sup>20</sup> The comparison with Mg metal, that does not favour dendrite formation, indicates that both the high surface diffusion barriers for Li and the low surface energy density promote dendrite formation. This is because Li-metal diffusion away from the tip where it is initially deposited is hindered



and large surface area morphologies are allowed.<sup>21</sup> To regulate these issues, strategies are employed which aim to control the Li-metal-electrolyte interface via the SEI composition.<sup>22</sup> Residual stress within the Li-metal appears to be another driving force for Li-metal growth.<sup>23</sup> This motivates the design of substrates that can release this stress.<sup>10,23</sup> Finally, investigations of how mechanical forces affect dendrite nucleation and growth, have shown that electrolytes with a shear modulus, at least 2 times larger than that of Li-metal, can prevent dendrite growth.<sup>24</sup> This has given rise to research where mechanically strong separators, solid electrolytes and protective films are investigated.<sup>6-10,16,17</sup>

3D scaffolds are an interesting approach, as they provide the possibility to control the interface, the local interface environment and to a large extent the charge transport. They can also provide a route to mitigate delamination due to their ability to accommodate large volumetric changes upon Li-metal plating and stripping. In a 3D scaffold that is electronically conducting, the electric field is roughly uniform and the local current density is reduced, suppressing dendrite growth.<sup>25-30</sup> However, the 3D porous conductive matrix is equipotential, due to which Li-metal can also be deposited on top of the 3D matrix, thus negating its targeted function.<sup>31</sup>

Here we explore an alternative approach through the introduction of a material with a high dielectric constant (which we will refer to as a high dielectric material) as a 3D scaffold. Due to the polarizing power of high dielectric material, an effective immobile surface (space) charge density  $\rho_{charge}$  is established, opposing the applied field in the battery (ferroelectric effect), that scales with the dielectric constant ( $\nabla \cdot D = \rho_{charge}$  where  $D = \epsilon_0 \epsilon_r E$ ,  $\epsilon_0$  and  $\epsilon_r$  the vacuum and relative permittivity and  $E$  the electrical field). As a consequence, the electrical field lines are drawn towards the high dielectric material (dictated by Gauss Law) which leads to lowering of the divergence of the electrical field in the vicinity of the Li-metal deposition. At the tip of a dendrite near a high dielectric material, this effectively leads to a decrease in the electrical field divergence, and thus to a lower local electrical field gradient. This is shown in **Figure 2.1**, where the calculated electrical field gradient near a dendrite with, and without high dielectric blocks in the vicinity of a dendrite are compared. This is proposed to lower the driving force for the plating of Li-ions at the tip of an inhomogeneity near to the high dielectric material. Indeed more homogeneous deposits have been recently observed, due to the presence of high dielectric materials.<sup>32</sup> Based on this simple principle, we prepared porous 3D barium titanate (henceforth denoted as BTO) scaffolds which have an ultra-high dielectric constant. The impact of this high dielectric based 3D scaffold is examined by direct comparison with an  $\text{Al}_2\text{O}_3$  3D scaffold having a low dielectric constant and a comparable 3D scaffold morphology. These Li-metal free scaffolds (anode-less) are

cycled versus a Li-metal anode to evaluate the Li-metal morphology and cycling efficiency. To highlight the impact of this approach, cycling is performed in combination with a conventional electrolyte (1M LiPF<sub>6</sub> in 1:1 v/v EC: DMC), presenting the worst-case scenario as this electrolyte is well known for leading to uncontrolled SEI formation. In combination with the high dielectric BTO scaffold, this results in a Coulombic Efficiency (CE) in excess of 99.82% and small overpotential of 68 mV, reaching 240 cycles in half cells at 2 mA cm<sup>-2</sup> cycled to 1 mA h cm<sup>-2</sup>. In addition, when combined with an NMC cathode, the BTO scaffold anode leads to a strongly improved CE and cycle life. Its high porosity, about 60%, leads to a specific capacity of more than 2000 mA h g<sup>-1</sup>, taking into account the weight of the 3D scaffold. The high relative permittivity is shown to suppress dendrite growth, promote homogeneous plating, thus damping the self-amplifying cycle of SEI formation and dendritic growth. Nevertheless, several challenges remain, one of which is the reactivity of the scaffold. Though very limited, it contributes to the initial capacity loss, and the cycling of these anode-less scaffolds, still appears to terminate via a short circuit. This prompts the investigation of combinatorial approaches, especially utilizing optimized electrolytes and binders to improve performance. The proposed scaffolds are attractive from a practical standpoint, as they are prepared by means of regular electrode casting. Thereby, the proposed strategy presents new insights into the role of the permittivity on Li-metal deposition and a promising approach for the design of (anode-less) scaffolds to achieve efficient Li-metal anodes.

### 2.2 Materials and methods

Preparation of electrodes and electrochemical tests. Commercial BaTiO<sub>3</sub> (Euro Support Advanced Materials B.V., denoted as BTO) and Al<sub>2</sub>O<sub>3</sub> (Sigma-Aldrich, denoted as AO) powder were used to prepare 3D scaffolds on Cu current collectors having a high relative permittivity ( $\epsilon_r \approx 4000$ ) and a low relative permittivity ( $\epsilon_r \approx 8$ ) respectively. Firstly, BTO and AO were ball-milled at 450 rpm, 6 hours using 10 ZrO<sub>2</sub> balls to achieve relatively small particles and similar particle size distribution. Both materials were mixed with polyvinylidene fluoride (PVDF) and NH<sub>4</sub>HCO<sub>3</sub> (ratio at 5:1:4) using N-methyl-2-pyrrolidone (NMP) solvent to obtain a slurry which is cast on copper. The NH<sub>4</sub>HCO<sub>3</sub> acts as a template to achieve a high porosity<sup>33</sup> to increase the specific capacity of the anode (BTO scaffold). After that, the electrodes were dried under vacuum at 80 °C to remove the NH<sub>4</sub>HCO<sub>3</sub> template. The resulting electrodes were cut into round electrodes with a diameter of 12.7 mm. Coin cells were assembled using as-prepared electrodes with lithium metal as a counter electrode, a PE (Celgard 2300) separator and 150  $\mu$ l conventional carbonate electrolyte (1M LiPF<sub>6</sub> in 1:1 v/v EC: DMC). Galvanostatic cycling was performed by

deposition of Li onto the bare Cu working electrode or AO/BTO coated Cu scaffolds with different current densities ( $2 \text{ mA cm}^{-2}$  to  $8 \text{ mA cm}^{-2}$ ) to a fixed capacity ( $1 \text{ mA h cm}^{-2}$  or  $4 \text{ mA h cm}^{-2}$ ), followed by complete Li stripping at different current densities up to a voltage cutoff of  $1.0 \text{ V vs Li/Li}^+$ . A rest time of 2-30 minutes was set between plating and stripping. Full cells composed of a porous BTO scaffold on a Cu current collector (denoted as BTOCu) in combination with a  $\text{LiNi}_{0.8}\text{Co}_{0.1}\text{Mn}_{0.1}\text{O}_2$  (Umicore N.V., denoted as NCM) cathode were assembled. The BTO scaffold anode was firstly cycled versus Li-metal for two cycles to minimize initial irreversible Li consumption. NCM and  $\text{LiCoO}_2$  (Sigma-Aldrich, denoted as LCO) cathodes were prepared by mixing the active material with Super P and PVDF in a mass ratio of 8:1:1, and NMP was used as a solvent. The mass loading of the NCM/LCO electrode was about  $5 \text{ mg cm}^{-2}$ . Li/NCM and BTOCu/NCM cells were cycled within the potential range of  $3.0 - 4.2 \text{ V (vs. Li/Li}^+)$  at room temperature. Galvanostatic cycling was conducted on a Maccor battery testing system. The impedance measurements of the coin cells were carried out on Autolab between  $100 \text{ kHz}$  and  $0.01 \text{ Hz}$ . Cyclic voltammograms (CVs) were recorded using the same electrochemical workstation at a scan rate of  $1 \text{ mV s}^{-1}$  in the range of  $-0.5 \text{ V} - 3 \text{ V}$ .

Characterization of the Materials and the Electrodes. SEM images were obtained of the 3D scaffolds after a discharge capacity of  $1 \text{ mA h cm}^{-2}$ . Before SEM imaging, the electrodes were rinsed with dimethyl carbonate in a glove box to remove lithium salts and dried several times in a vacuum chamber. Cross-section SEM samples were prepared by cutting with scissors in the glove box. Subsequently, samples were transferred into an SEM (JEOL JSM-6010LA) machine under dry Argon conditions, and images were taken using an accelerating voltage of  $2-10 \text{ kV}$  (secondary electron). Nitrogen adsorption-desorption isotherms were recorded using an automatic surface area and porosity analyzer (Micromeritics) at  $77 \text{ K}$ . The particle size distribution of BTO and AO after ball milling was measured using Microtrac S3500.

LCO/Cu and LCO/BTOCu cells (in a plastic cell capsule suitable for operando NMR measurements and reported in detail elsewhere)<sup>39</sup> with a conventional carbonate electrolyte were assembled in the glove box and studied by operando  $^7\text{Li}$ -NMR to monitor the microstructural evolution of Li deposits. Measurements were done on a wide bore Bruker Ascend 500 system equipped with a NEO console with a magnetic field strength of  $11.7\text{T}$  and a  $^7\text{Li}$  resonance frequency of  $194.37 \text{ MHz}$ . Operando static  $^7\text{Li}$  NMR experiments were performed at room temperature with an NMR Service ATMC operando NMR probe, and the electrochemical cell was simultaneously controlled by a portable Maccor battery testing system. During the 1D static  $^7\text{Li}$  NMR measurements the cells were charged to  $1 \text{ mA cm}^{-2}$  at  $0.2 \text{ mA cm}^{-2}$  to deposit Li to the anode and subsequently discharged  $2.5 \text{ V}$  to stripped

the Li-metal from the anode, while the NMR spectra were continuously acquired. Each spectrum took about 2 minutes to acquire. The chemical shifts are referenced to a 0.1M LiCl solution. Bruker Topspin 4.0.6 as well as Mestrenova were used for raw data processing and analysis.

Electrical field calculations. All simulations were done in COMSOL Multiphysics 5.4. Using the electrostatics software, the electric field around a simulated dendrite was calculated. The electrodes used were copper and lithium which were taken from the COMSOL material's library. Three different electrodes are considered, bare Cu and Cu with different insulator blocks (BTO, AO). Two electrodes (Cu ( $2\ \mu\text{m} \times 250\ \mu\text{m}$ ) versus BTO on Cu, or AO on Cu ( $2\ \mu\text{m} \times 250\ \mu\text{m}$ )) were placed at two sides of the electrolyte (EC/DMC,  $50\ \mu\text{m} \times 250\ \mu\text{m}$ ). The BTO and AO blocks on the electrode have the dimensions  $8\ \mu\text{m} \times 8\ \mu\text{m}$  with a gap of  $2\ \mu\text{m}$ . For the simulations, a dendrite is represented as a rectangular shape ( $0.1\ \mu\text{m} \times 0.2\ \mu\text{m}$ ) with a hemispherical top. The dielectric constants or equivalent the relative permittivity of the BTO, AO and the electrolyte EC/DMC is 4000, 8 and 40, respectively.

## 2.3 Results and discussions

### 2.3.1 Electrical field calculations

To understand the impact of the dielectric constant of a dielectric block on the electrical field gradient at a nearby Li-metal dendrite, the electrical field is simulated in two dimensions. This is performed for both a bare Cu current collector with a Li-metal dendrite, and a Cu current collector in combination with high dielectric BaTiO<sub>3</sub> (BTO) and low dielectric Al<sub>2</sub>O<sub>3</sub> (AO) blocks surrounding the dendrite as shown in **Figure 2.1**. The relative permittivity's of BTO, AO and the electrolyte are 4000, 8 and 40, respectively. These Cu, BTO/Cu and AO/Cu electrodes are placed against a counter electrode at a distance of  $250\ \mu\text{m}$  separated by the electrolyte to approximate the situation in a battery. The BTO and AO blocks are taken as  $8\ \mu\text{m} \times 8\ \mu\text{m}$  with a gap of  $2\ \mu\text{m}$  in which a lithium dendrite is placed, represented by a rectangular shape ( $0.1\ \mu\text{m} \times 0.2\ \mu\text{m}$ ) with a hemispherical tip.

In **Figure 2.1a** and **2.1b**, the simulated electrical field around a single dendrite in the electrolyte is shown. Near the tip of the Li-metal, the electrical field gradient increases, demonstrating that the electrical field lines are focused to the tip of the electronically conducting Li-metal dendrite. This is driven by the larger surface charge density present at the sharp electronically conducting features. This promotes the preferential deposition of Li-ions from the electrolyte on the tip of the dendrite, representing the fundamental driving force for dendrite formation in a homogeneous medium.

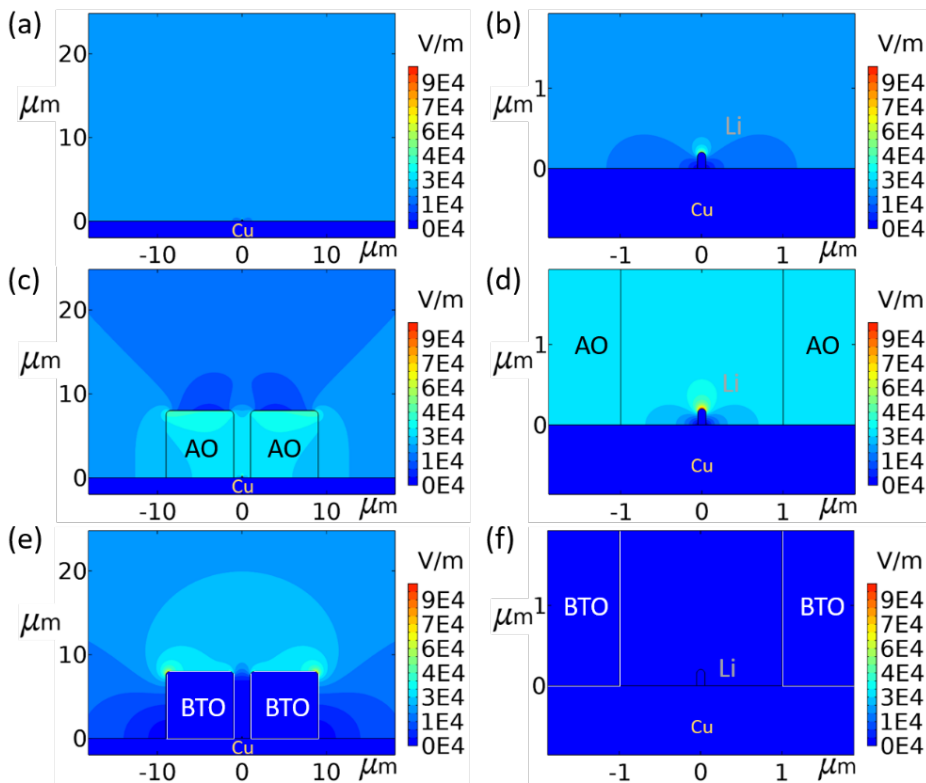


**Figure 2.1** Electrical field simulations around a Li-metal deposit with and without the presence of low and high dielectric blocks. Li-metal deposit (a) on bare Cu planar copper and (b) zoomed-in figure, (c) in combination with low dielectric AO block (d) zoomed-in figure, (e) in combination with high dielectric BTO block (f) zoomed-in figure.

As shown in **Figure 2.1c** and **2.1d**, blocks of AO (relative permittivity 8, smaller than that of the electrolyte) and in **Figure 2.1e** and **2.1f**, blocks of BTO (relative permittivity 4000, much higher than that of the electrolyte) are added on both sides of the Li-dendrite. For AO, the electrical field gradient near the tip of the dendrite increases (**Figure 2.1d**) when compared to its presence in the electrolyte alone (**Figure 2.1b**), whereas for BTO, the electrical field gradient at the tip of the dendrite disappears (**Figure 2.1e**). The low polarizability of the AO “leaves” the electrical field gradient at the Li-metal tip, whereas the high polarizability of the BTO “pulls” the electrical field lines away from the Li-metal tip towards the surface of the BTO itself. This suggests that the presence of high dielectric blocks in the vicinity of a Li-metal growth takes away the driving force for Li deposition at the tip of sharp features, thus taking away the driving force for tip driven dendrite growth. Several geometries were simulated, such as different block distances, different dendrite lengths to name a few, provided in the Supplementary Information **Figure S2.1-S2.3**, showing similar results. Based

on this it can be postulated that a high dielectric scaffold can suppress dendrite growth and promote a homogeneous and more dense Li-metal filling of the pores of the scaffold. This can be expected to lead to less “dead” Li-metal forming as well as a smaller Li-metal electrolyte interface, thus less electrolyte decomposition, enabling higher cycling efficiencies and longer cycle life of the Li-metal anode.

### 2.3.2 Electrode preparation

To evaluate the impact of the BTO and AO porous scaffolds, both materials were cast on a Cu current collector, similar to what is done in the preparation of regular Li-ion insertion electrodes. Commercial BTO and AO were ball-milled at 450 rpm for 20 hours to obtain a comparable size distribution of both materials. **Figure S2.4 a, c** shows the morphology of the BTO and AO particles obtained via a scanning electron microscopy (SEM) analysis. Both materials have an average particle size of approximately 8  $\mu\text{m}$  as seen from the SEM images (**Figure S2.4**) and via a Dynamic Light Scattering (**Figure S2.5**) analysis. According to the nitrogen adsorption/desorption isotherms (**Figure S2.6**), their Brunauer-Emmette-Teller (BET) specific surface areas are also comparable, amounting 23.59 and 23.08  $\text{m}^2 \text{g}^{-1}$  for BTO and AO, respectively. The similar surface area and particle size distribution of BTO and AO are crucial to allow us to distinguish the impact of the dielectric constant on Li-metal deposition from that of the scaffold morphology. These ball-milled materials were used to build the scaffold for lithium metal plating on a Cu current collector. Both materials were mixed with polyvinylidene fluoride (PVDF) and  $\text{NH}_4\text{HCO}_3$  (ratio at 5:1:4) using an N-methyl-2-pyrrolidone (NMP) solvent to obtain a slurry that was cast on a regular Cu current collector. The  $\text{NH}_4\text{HCO}_3$  acts as a template to achieve a high porosity<sup>33</sup> which is required to achieve high specific anode capacities, taking into account the weight of the scaffold. After that, the electrodes were dried under vacuum at 80  $^\circ\text{C}$  to remove the  $\text{NH}_4\text{HCO}_3$  template. The resulting porosity of the AO and BTO scaffolds is 62% and 64%, respectively and thus comparable. The thickness of these two electrodes is around 45  $\mu\text{m}$ , including 10  $\mu\text{m}$  copper foil. When this porous volume is completely filled by Li-metal, the specific capacity of the anode is approximately 2240  $\text{mA h g}^{-1}$ . Aiming to expose the impact of a high dielectric scaffold on the cycle life of anode-less configuration of these electrodes, a blank 1M  $\text{LiPF}_6$  in EC/DMC electrolyte was used. As mentioned earlier, this represents a worst-case scenario because it is well known that this electrolyte formulation leads to uncontrolled dendrite and SEI formation.<sup>9,34</sup>

### 2.3.3 Operando solid-state NMR

To test the hypothesis that the Li-metal deposition is less dendritic and more homogeneous in the pores of the high dielectric scaffold, and that this leads to better reversibility,

operando  $^7\text{Li}$  solid-state NMR is performed, the results of which are shown in **Figure 2.2**. Operando  $^7\text{Li}$  solid-state NMR is a direct probe of Li in realistic cell conditions and allows to distinguish differences in the Li-metal microstructure.<sup>12,35,36</sup> As shown in Supplementary **Figure S2.7**, the signals from Li-species in the SEI and electrolyte are in the expected region of diamagnetic materials (-10 to 10 ppm), Li in the  $\text{LiCoO}_2$  (cathode) in the wide region of -50 to 50 ppm, which both can be readily separated from the Li-metal chemical shift which is dominated by its knight shift.<sup>35</sup> The NMR radiofrequency (RF) has a limited penetration depth into the Li-metal, referred to as skin depth, which at the presently employed  $B_0$  field of 11.7 T amounts to approximately 11  $\mu\text{m}$ .<sup>13</sup> As a consequence, for deposited Li-microstructures such as dendrites and mossy structures, typically smaller than a few micrometers, the RF penetration can thus be expected to be complete. A Li-metal strip<sup>13,35</sup> gives rise to a resonance at about 245 ppm when placed perpendicular to the fixed magnetic field  $B_0$  and at about 270 ppm when the strip is parallel to  $B_0$ , a consequence of the bulk magnetic susceptibility effect.<sup>13</sup> An anode-less design (absence of Li-metal at the anode in the initial state) is investigated by operando solid-state NMR, utilizing  $\text{LiCoO}_2$  as the counter electrode (and Li source), such that the observed Li-metal signal arises only due to the deposition at the anodes of interest, similar to a recently reported study.<sup>37</sup>

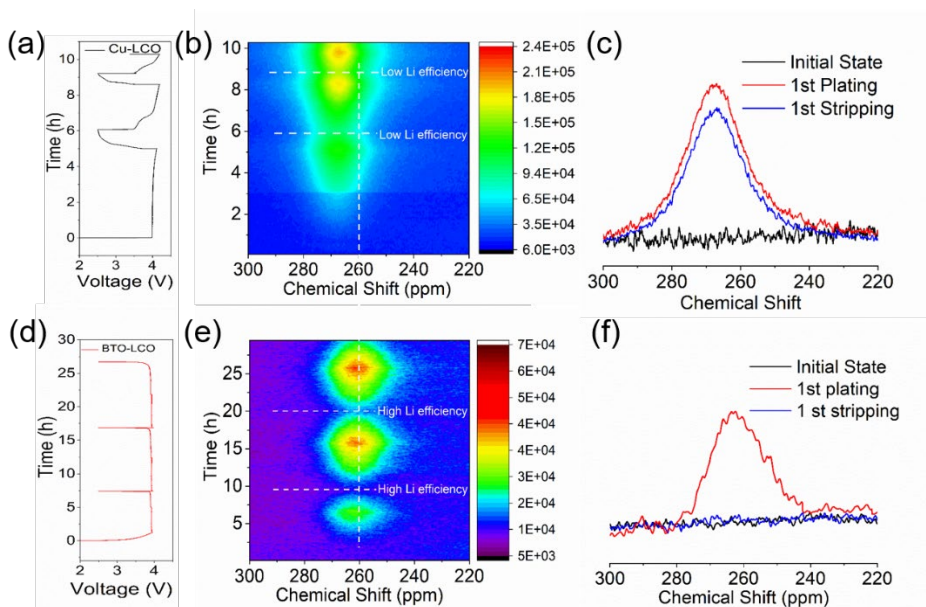


**Figure 2.2** Operando  $^7\text{Li}$  solid-state NMR of Li-metal plating/stripping on bare Cu and the anode-less BTO porous scaffold in a full cell versus  $\text{LiCoO}_2$ . (a-c) Bare Cu versus a  $\text{LiCoO}_2$  cathode with a 1M  $\text{LiPF}_6$  EC/DMC electrolyte cycled at  $0.2 \text{ mA cm}^{-2}$  to  $1 \text{ mA cm}^{-2}$  charge capacity and discharge to 2.5 V cut-off (a) voltage profile, (b) 2D operando NMR spectra as a function of cycling, (c) 1D  $^7\text{Li}$  solid-state NMR spectra at selected conditions. (d-f)

Anode-less BTO scaffold on Cu versus a  $\text{LiCoO}_2$  cathode with a 1M  $\text{LiPF}_6$  EC/DMC electrolyte cycled at  $0.2 \text{ mA cm}^{-2}$  to  $1 \text{ mA cm}^{-2}$  charge capacity and discharge to 2.5 V cut-off (d) voltage profile, (e) 2D  $^7\text{Li}$  operando NMR spectra as a function of cycling, (f) 1D  $^7\text{Li}$  solid-state NMR spectra at selected conditions.

During charge (plating) on the bare Cu current collector, the  $^7\text{Li}$  metal resonance appears at approximately 266 ppm as shown in **Figure 2.2b** and **2.2c**. On the other hand for the Li-metal deposits in the BTO scaffold, it occurs at approximately 260 ppm shown in **Figure 2.2e** and **2.2f**. Dendritic microstructures, growing perpendicular to Cu have been associated with a narrow chemical-shift-range centered at around 270 ppm whereas mossy microstructures encompass broader resonances covering a chemical shift range of 262-274 ppm.<sup>12</sup> Not surprisingly, the present results demonstrate that on a bare Cu current collector, in combination with a regular carbonate electrolyte, mossy/dendritic Li-metal growth is initiated already during the first plating cycle. Interestingly, the Li-metal chemical shift in the BTO scaffold is similar to that observed for dense Li-metal plated in the separator when plated under pressure.<sup>12</sup> The density of the BTO scaffold (64 %) is similar to that of the separators, thus the operando  $^7\text{Li}$  solid-state NMR indicates that Li-metal plating fills the BTO scaffold pores, preventing the growth of mossy and dendritic microstructures. Discharge (Li-metal stripping) of the bare Cu current collector results in high overpotentials, indicating a strongly increased internal resistance, which is associated with severe SEI formation that hinders Li-ion transport as seen in **Figure 2.2a**. The intensity of the  $^7\text{Li}$  metal NMR resonance hardly decreases during discharge (**Figure 2.2b** and **2.2c**), reflecting the difficulty to strip the Li-metal deposits from the Cu, which upon cycling results in rapid accumulation of inactive “dead” Li-metal (see **Figure 2.2b**) comprehensively studied recently using operando NMR.<sup>37</sup> In contrast, the voltage during discharge (Li-metal stripping) for the BTO scaffold is nearly the same as during charge, indicating that the internal resistance is practically unaffected by the SEI formation. Concurrently, the  $^7\text{Li}$  metal resonance completely disappears upon the charge, as confirmed in **Figure 2.2f**, demonstrating that all Li-metal can be completely stripped from the BTO scaffold, and thus that a high Li-metal stripping/plating efficiency is achieved. The large increase in Li-metal signal after the first cycle can be explained by a low first cycle efficiency, where a significant fraction of the capacity is lost in the formation of SEI products by introducing Li-metal at the anode. In summary, operando  $^7\text{Li}$  solid-state NMR demonstrates that the presence of the high dielectric anode-less BTO scaffold results in more compact and less dendritic/mossy Li-metal, in line with the suggested impact of a high dielectric scaffold on the electrical field gradients shown in **Figure 2.1**, which reduces the amount of observed “dead” Li-metal and SEI formation, even in a conventional 1 M  $\text{LiPF}_6$  EC/DMC electrolyte.



## 2.3.4 Electrochemical evaluation half cells

Galvanostatic cycling in a half-cell is carried out to compare the reversibility of anode-less bare Cu with the porous BTO and AO scaffolds deposited on the Cu current collector, all in combination with a  $\text{LiPF}_6$  in EC/DMC electrolyte. Coin cells were assembled using lithium foil as the counter-electrode to evaluate the cycling stability as expressed by the Coulombic Efficiency (CE) *i.e.* the ratio of the Li stripping capacity to the plating capacity, the results of which are shown in **Figure 2.3**.

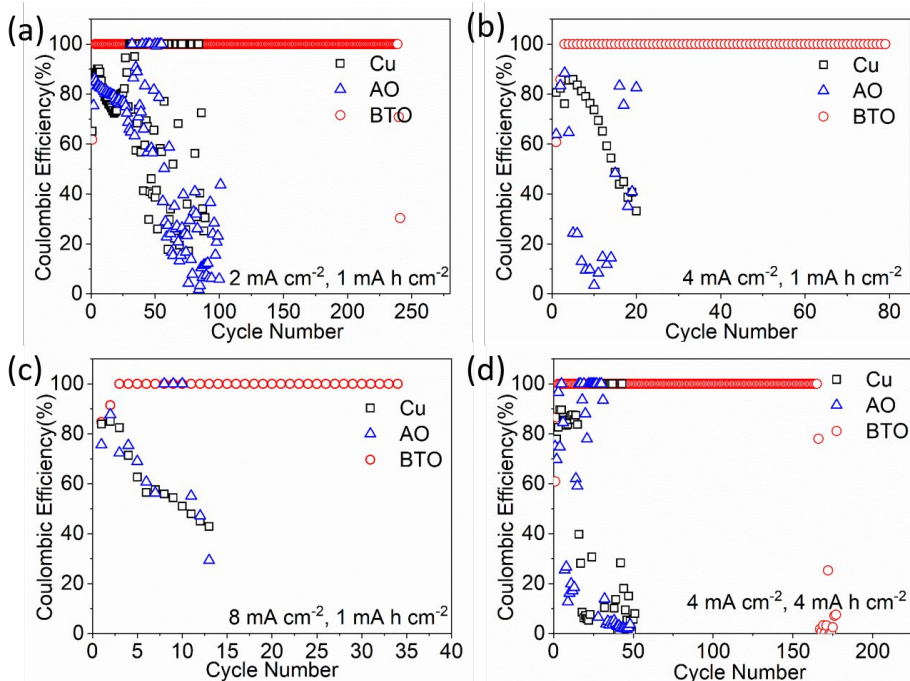


**Figure 2.3** Half-cell performance of the anode-less Cu and AO and BTO scaffolds versus a Li-metal anode. (a-c) Lithium Coulombic efficiencies at a fixed areal capacity of  $1 \text{ mA h cm}^{-2}$  at various current densities (a)  $2 \text{ mA cm}^{-2}$ , (b)  $4 \text{ mA cm}^{-2}$ , (c)  $8 \text{ mA cm}^{-2}$  using three different electrodes. (d) Lithium Coulombic efficiency at a current density of  $4 \text{ mA cm}^{-2}$  with a high areal capacity of  $4 \text{ mA h cm}^{-2}$ . For all experiments, the Li-metal stripping was cut off at  $1.0 \text{ V vs Li/Li}^+$ .

The CE is an essential parameter to evaluate the reversibility of the lithium metal anode, reflecting the irreversible loss of Li to both “dead” Li (Li-metal electrically isolated from the current collector) and to the formation of the SEI species during each cycle. Cycling is performed to a fixed Li-metal capacity of  $1 \text{ mA h cm}^{-2}$  at rates of 2, 4 and  $8 \text{ mA cm}^{-2}$  as shown in **Figure 2.3a-c**, and to a lithium metal capacity of  $4 \text{ mA h cm}^{-2}$  at a rate of  $4 \text{ mA cm}^{-2}$ , as shown in **Figure 2.3d**. Li-metal stripping is always limited by a  $1.0 \text{ V vs Li/Li}^+$  cut-off voltage.

The two initial cycles are always performed at a current density of  $0.5 \text{ mA cm}^{-2}$  to form the SEI, leading to a relatively low CE in the order of about 60% and about 85%. As shown in the cyclic voltammetry curves in **Figure S2.8**, the BTO scaffold shows a small peak at 1.2 V (and no activity is observed for AO). However, there is no obvious structural change of the BTO scaffold after the 1<sup>st</sup> and 100<sup>th</sup> cycles as verified by XRD (**Figure S2.9**). Therefore the BTO scaffold does contribute to the initial capacity loss. It does not, however, show degradation in contact with Li-metal and upon over cycling. Although both BTO and AO can be reduced by Li-metal, it appears that this process is passivated, most likely only occurring at the BTO/AO surface region. Under all cycling conditions, the BTO scaffold results in a dramatically improved CE and cycle life as compared to the bare Cu and the AO scaffold. After the two initial cycles, cycling to  $1 \text{ mA h cm}^{-2}$  at 2.0, 4.0 and  $8.0 \text{ mA cm}^{-2}$  results in a dramatically improved CE of 99.82%, 99.35%, and 99.30% for the cells with the BTO scaffold during 240, 80 and 30 cycles, respectively (**Figure 2.3a-c**). In sharp contrast, the cells with bare Cu and the AO scaffold show rapid decay in the cycling efficiency, leading to early cell death before reaching 20 cycles. Nevertheless, the BTO scaffold can maintain this for a limited number of cycles as indicated in **Figure 2.3**, which is remarkable given the non-optimized  $\text{LiPF}_6$  EC/DMC electrolyte used. Also cycling towards a larger (practical) capacity of  $4 \text{ mA h cm}^{-2}$  at  $4 \text{ mA cm}^{-2}$ , which including the BTO scaffold equals to a specific capacity of  $2000 \text{ mA h g}^{-1}$ , results in a CE of 99.68% that can be maintained for more than 160 cycles (**Figure 2.3d**). This is equivalent to a specific capacity above  $2000 \text{ mA h g}^{-1}$ , which in combination with a sulphur-carbon cathode would yield a cell level energy density above  $500 \text{ Wh kg}^{-1}$ .

The evolution of the voltage during cycling shown in **Figure 2.4** and **Figure S2.10** provides more insight into the evolution of the CE seen for the different anodes (**Figure 2.3**). Under all cycling conditions tested, the anode-less Cu and AO scaffold result in a rapid increase in the plating and stripping potentials as shown in **Figure 2.4a-d**. This can be associated with the SEI formation, amplified by mossy/dendritic Li-metal growth, leading a high internal resistance until no cycling capacity remains, or a short circuit results. The BTO scaffold can maintain much lower overpotentials for more cycles, *i.e.* approximately 68, 220 and 375 mV at current densities of 2, 4 and  $8 \text{ mA cm}^{-2}$ , respectively. Nevertheless, also for the BTO scaffold, the overpotentials increase, indicating that upon extended cycling, these cells also fail due to SEI growth. These conclusions are further supported by electrochemical impedance spectroscopy (EIS) measurements shown in **Figure 2.4e-g**. The total resistance of the cells with the Cu and AO scaffold anode shows a strong increase after 100 cycles at  $2 \text{ mA cm}^{-2}$  shown in **Figure 2.4g**, associated with the SEI formation driven by mossy/dendritic Li-metal growth. At the same conditions, the BTO scaffold has a much lower interfacial

resistance, indicating less SEI formation. In addition to half-cells, full cells were assembled using the BTO scaffold as a lithium free anode (anode-less), or a Li-metal anode, both paired with an NCM cathode, again in combination with a conventional 1 M LiPF<sub>6</sub> EC/DMC electrolyte (as shown in **Figure S2.11** and **S2.12**). The BTO scaffold outperforms the Li-metal anode in cycling rate and stability demonstrating a high average CE of 99.37%.

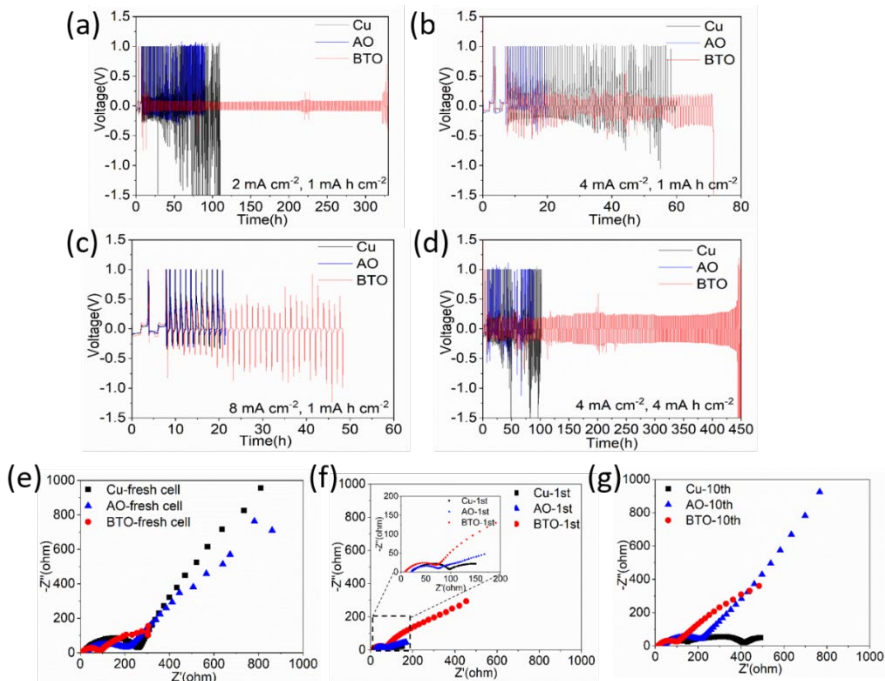


**Figure 2.4** Half-cell voltage evolution and impedance of the anode-less Cu and AO and BTO scaffolds vs a Li-metal anode. Evolution of the voltage during Li plating/stripping for the bare Cu and the AO and BTO scaffolds at different current densities (a) 2 mA cm<sup>-2</sup>, (b) 4 mA cm<sup>-2</sup>, (c) 8 mA cm<sup>-2</sup> with a fixed areal capacity of 1 mA h cm<sup>-2</sup>, and (d) an increased areal capacity of 4 mA h cm<sup>-2</sup> at a current density of 4 mA cm<sup>-2</sup>. Electrochemical impedance spectra of the half-cells for the bare Cu and the AO and BTO scaffolds (e) fresh cells, (f) the 1<sup>st</sup> cycle and (g) the 100<sup>th</sup> cycle measured at a current density of 2 mA cm<sup>-2</sup>.

### 2.3.5 Li-metal morphology

A SEM analysis is performed before and after cycling the cells at a current density of 2 mA cm<sup>-2</sup> to a specific capacity of 1 mA h cm<sup>-2</sup>, comparing bare Cu, the low dielectric constant AO scaffold and the high dielectric constant BTO scaffold, shown in **Figure 2.5**. On comparison, the BTO scaffold appears to lead to a more uniform lithium deposition, as no dendritic/mossy structures are observed (**Figure 2.5b, e**). The cross-sectional SEM image of

the BTO scaffold electrode(**Figure S2.13a**) also taken after plating to  $1 \text{ mA h cm}^{-2}$  at a current density of  $2 \text{ mA cm}^{-2}$ , suggests that the deposited Li-metal is dense and well-confined in the 3D scaffold of the BTO layer consistent with the operando  $^7\text{Li}$  solid-state NMR measurements depicted in **Figure 2.2**. In contrast, Li deposition on the bare Cu foil exhibits islands of accumulated dendritic structures (**Figure 2.5a, d**) and at the surface of the AO scaffold, dendrites are observed (**Figure 2.5c, f**).

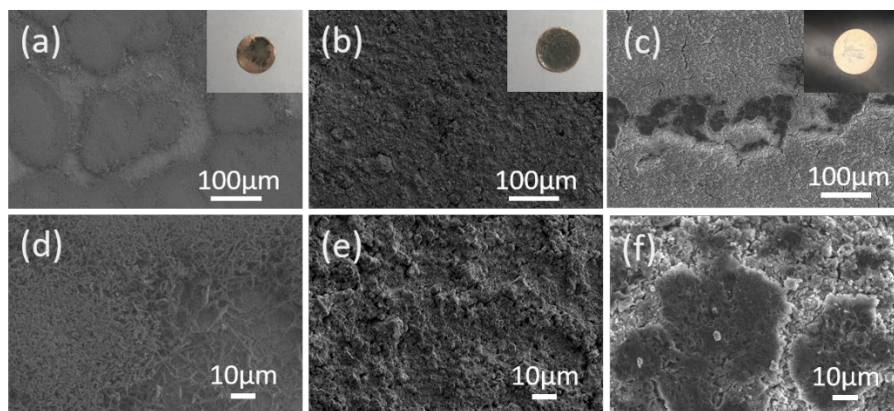


**Figure 2.5** SEM images after plating to  $1 \text{ mA h cm}^{-2}$  at  $2 \text{ mA cm}^{-2}$  of the bare Cu, low dielectric AO scaffold and high dielectric BTO scaffold. (a, d) Bare copper electrode and zoomed-in figure, (b, e) high dielectric BTO scaffold and zoomed-in figure, (c, f) low dielectric AO scaffold and zoomed-in figure. Insets show the digital images of the complete electrodes.

### 2.4 Discussion and conclusions

As schematically shown in **Figure 2.6a**, a fundamental driving force for the formation of dendritic/mossy Li-metal are large gradients in the electrical field lines caused by surface inhomogeneities. This acts as the starting point for uncontrolled SEI formation which in turn amplifies further inhomogeneous mossy/dendritic Li-metal deposition and the accumulation of inactive Li-metal, as demonstrated by the operando solid-state NMR (**Figure 2.2**) and the SEM results (**Figure 2.5**). This drives up the internal resistance (**Figure 2.4**), eventually leading to cell death. A comparison of the high dielectric BTO scaffold ( $\epsilon_r \approx 4000$ ) and the low dielectric AO scaffold ( $\epsilon_r \approx 8$ ), having a similar morphology (in terms of loading, particle size distribution and porosity), makes it possible to distinguish between the impact of a non-conducting scaffold morphology and the impact of the dielectric constant of the scaffold on the Li-metal plating.

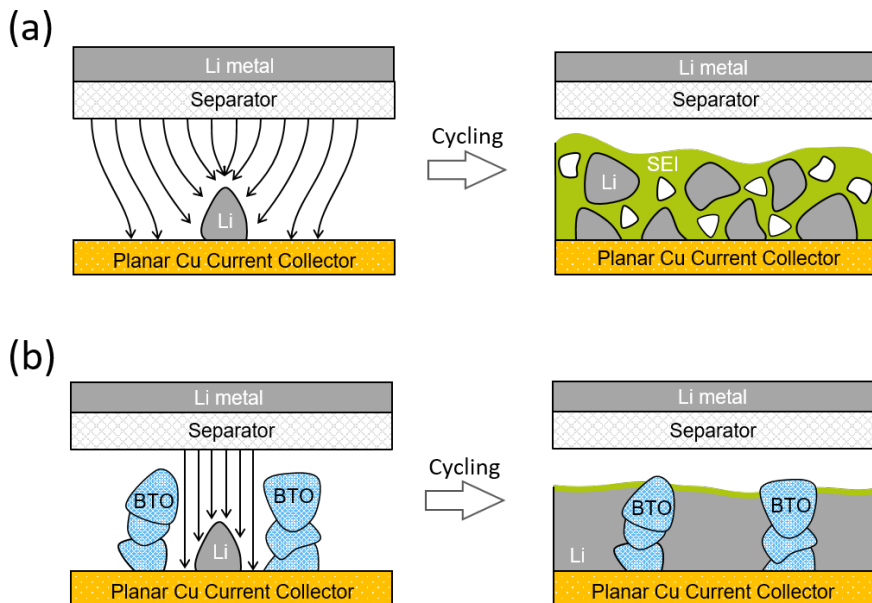


**Figure 2.6** Schematic diagram of lithium metal plating and stripping with and without the presence of the high dielectric BTO porous scaffold. (a) lithium metal plating/stripping process on planer copper, (b) lithium metal plating/stripping process on BTO coated copper foil.

As schematically shown in **Figure 2.6b**, the 3D high-dielectric BTO scaffold takes away the electrical field gradients at the tip of uneven Li-metal deposits, as supported by electrical field calculations (**Figure 2.1**). This leads to a more homogeneous Li-ion flux, and thus to less mossy/dendritic and more homogeneous Li-metal deposits as recently shown by Guo<sup>32</sup> and as evidenced by operando solid-state NMR (**Figure 2.2**) and SEM (**Figure 2.5**). This prevents the accumulation of deactivated Li-metal which is responsible for the highly improved cycling efficiency (**Figure 2.3**) and lowers the exposed Li-metal-electrolyte area, minimizing SEI formation and thus preventing the uncontrolled and self-amplified growth of the SEI and dendritic Li-metal deposits, rationalizing the low overpotentials during extended cycling observed in **Figure 2.4**. As a result, the presented strategy enhances the cycle of life and lowers safety concerns associated with dendrite growth.<sup>38</sup> Notably, these results are achieved under the challenging conditions of an anode-less design i.e. the initial absence of Li-metal in the BTO scaffold, and in combination with a non-optimized carbonate electrolyte (1 M LiPF<sub>6</sub> EC/DMC).

In conclusion, the challenge faced by Li-metal anodes is to prevent dendritic and mossy Li-metal growth that catalyze electrolyte decomposition and lead to low electrochemical

plating/stripping efficiencies. Electrical field calculations show that through the dielectric effect, the presence of a high dielectric material takes away the electrical field gradient at the tip of nearby Li-metal deposits, suggesting that the Li-metal dendritic and mossy microstructure growth can be suppressed by an anode comprising of a high dielectric porous scaffold. 3D porous scaffolds are prepared through a facile casting approach using both a high dielectric scaffold material, BaTiO<sub>3</sub> (BTO) and a low dielectric scaffold material, Al<sub>2</sub>O<sub>3</sub> (AO), to distinguish between the impact of a porous scaffold and the high dielectric constant on the electrochemical Li-metal plating. These electronically insulating scaffolds show minimal electrochemical activity, and the added weight leads to specific capacities exceeding 2000 mA h g<sup>-1</sup>. Operando <sup>7</sup>Li solid-state NMR of an anode-less BTO scaffold-LiCoO<sub>2</sub> full cell demonstrates that the high dielectric scaffold induces compact plating and efficient stripping. Half-cells with a BTO scaffold cycled against Li-metal exhibits 99.82% CE after the first two initial cycles, low overpotentials and an extended cycle life even when the worst-case scenario 1 M LiPF<sub>6</sub> EC/DMC electrolyte is used, under different current and capacity conditions. With the same basic electrolyte, full cells also demonstrate improved performance with an average CE of 99.37%. These results demonstrate the use of high dielectric scaffolds that take away the driving force for inhomogeneous Li-metal deposition as a strategy to improve the reversibility and safety of Li-metal anodes in an anode-less configuration. The next avenues to explore are combinations with more stable SEI forming electrolytes and additives, optimization of the high dielectric scaffold, to minimize the capacity loss during the first cycles and to further extend the cycle life.

### References

- 1 Armand, M. & Tarascon, J.-M. Building better batteries. *Nature* **451**, 652-657 (2008).
- 2 Goodenough, J. B. & Park, K. S. The Li-ion rechargeable battery: a perspective. *J. Am. Chem. Soc.* **135**, 1167-1176 (2013).
- 3 Dunn, B., Kamath, H. & Tarascon, J.-M. Electrical energy storage for the grid: a battery of choices. *Science* **334**, 928-935 (2011).
- 4 Tarascon, J.-M. & Armand, M. Issues and challenges facing rechargeable lithium batteries. *Nature* **414**, 359-367 (2001).
- 5 Qiao, Y., Deng, H., He, P. & Zhou, H. A 500 Wh/kg Lithium-Metal Cell Based on Anionic Redox. *Joule* **4**, 1445-1458 (2020).
- 6 Xu, W. *et al.* Lithium metal anodes for rechargeable batteries. *Energy Environ. Sci.* **7**, 513-537 (2014).

- 7 Lin, D., Liu, Y. & Cui, Y. Reviving the lithium metal anode for high-energy batteries. *Nat. Nanotech.* **12**, 194 (2017).
- 8 Guo, Y., Li, H. & Zhai, T. Reviving lithium-metal anodes for next-generation high-energy batteries. *Adv. Mater.* **29**, 1700007 (2017).
- 9 Cheng, X.-B., Zhang, R., Zhao, C.-Z. & Zhang, Q. Toward safe lithium metal anode in rechargeable batteries: a review. *Chem. Rev.* **117**, 10403-10473 (2017).
- 10 Zhang, X., Wang, A., Liu, X. & Luo, J. Dendrites in lithium metal anodes: suppression, regulation, and elimination. *Acc. Chem. Res.* **52**, 3223-3232 (2019).
- 11 Hsieh, Y.-C. *et al.* Quantification of Dead Lithium via In Situ Nuclear Magnetic Resonance Spectroscopy. *Cell Rep. Phys. Sci.* **1**, 100139 (2020).
- 12 Chang, H. J. *et al.* Investigating Li microstructure formation on Li anodes for lithium batteries by in situ  $^6\text{Li}/^7\text{Li}$  NMR and SEM. *J. Phys. Chem. C* **119**, 16443-16451 (2015).
- 13 Bhattacharyya, R. *et al.* In situ NMR observation of the formation of metallic lithium microstructures in lithium batteries. *Nat. Mater.* **9**, 504-510 (2010).
- 14 Märker, K., Xu, C. & Grey, C. P. Operando NMR of NMC811/graphite lithium-ion batteries: Structure, dynamics, and lithium metal deposition. *J. Am. Chem. Soc.* **142**, 17447-17456 (2020).
- 15 Weber, R. *et al.* Long cycle life and dendrite-free lithium morphology in anode-free lithium pouch cells enabled by a dual-salt liquid electrolyte. *Nat. Energy* **4**, 683-689 (2019).
- 16 Tikekar, M. D., Choudhury, S., Tu, Z. & Archer, L. A. Design principles for electrolytes and interfaces for stable lithium-metal batteries. *Nat. Energy* **1**, 1-7 (2016).
- 17 Lang, J., Qi, L., Luo, Y. & Wu, H. High performance lithium metal anode: progress and prospects. *Energy Stor. Mater.* **7**, 115-129 (2017).
- 18 Chazalviel, J.-N. Electrochemical aspects of the generation of ramified metallic electrodeposits. *Phys. Rev. A* **42**, 7355 (1990).
- 19 Ely, D. R. & García, R. E. Heterogeneous nucleation and growth of lithium electrodeposits on negative electrodes. *J. Electrochem. Soc.* **160**, A662 (2013).
- 20 Yan, K. *et al.* Selective deposition and stable encapsulation of lithium through heterogeneous seeded growth. *Nat. Energy* **1**, 1-8 (2016).

- 21 Ling, C., Banerjee, D. & Matsui, M. Study of the electrochemical deposition of Mg in the atomic level: why it prefers the non-dendritic morphology. *Electrochim. Acta* **76**, 270-274 (2012).
- 22 Wang, J. *et al.* In Situ Self-Assembly of Ordered Organic/Inorganic Dual-Layered Interphase for Achieving Long-Life Dendrite-Free Li Metal Anodes in LiFSI-Based Electrolyte. *Adv. Funct. Mater.* 2007434 (2020).
- 23 Wang, X. *et al.* Stress-driven lithium dendrite growth mechanism and dendrite mitigation by electroplating on soft substrates. *Nat. Energy* **3**, 227 (2018).
- 24 Monroe, C. & Newman, J. Dendrite growth in lithium/polymer systems: A propagation model for liquid electrolytes under galvanostatic conditions. *J. Electrochem. Soc.* **150**, A1377 (2003).
- 25 Zhang, R. *et al.* Conductive nanostructured scaffolds render low local current density to inhibit lithium dendrite growth. *Adv. Mater.* **28**, 2155-2162 (2016).
- 26 Liu, Y. *et al.* Lithium-coated polymeric matrix as a minimum volume-change and dendrite-free lithium metal anode. *Nat. Commun.* **7**, 10992 (2016).
- 27 Liang, Z. *et al.* Composite lithium metal anode by melt infusion of lithium into a 3D conducting scaffold with lithiophilic coating. *Proc. Natl. Acad. Sci. USA* **113**, 2862 (2016).
- 28 Chi, S. S., Liu, Y., Song, W. L., Fan, L. Z. & Zhang, Q. Prestoring lithium into stable 3D nickel foam host as dendrite-free lithium metal anode. *Adv. Funct. Mater.* **27**, 1700348 (2017).
- 29 Zhang, Y. *et al.* High-capacity, low-tortuosity, and channel-guided lithium metal anode. *Proc. Natl. Acad. Sci. USA* **114**, 3584 (2017).
- 30 Yun, Q. *et al.* Chemical dealloying derived 3D porous current collector for Li metal anodes. *Adv. Mater.* **28**, 6932-6939 (2016).
- 31 Fan, L. *et al.* Stable Lithium Electrodeposition at Ultra-High Current Densities Enabled by 3D PMF/Li Composite Anode. *Adv. Energy Mater.* **8**, 1703360 (2018).
- 32 Guo, Y. *et al.* Shaping Li Deposits from Wild Dendrites to Regular Crystals via the Ferroelectric Effect. *Nano Lett.* **20**, 7680-7687 (2020).



- 33 Singh, D. P., Mulder, F. M. & Wagemaker, M. Templated spinel  $\text{Li}_4\text{Ti}_5\text{O}_{12}$  Li-ion battery electrodes combining high rates with high energy density. *Electrochem. Commun.* **35**, 124-127 (2013).
- 34 Liu, D.-H. *et al.* Developing high safety Li-metal anodes for future high-energy Li-metal batteries: strategies and perspectives. *Chem. Soc. Rev.* **49**, 5407-5445 (2020).
- 35 Marbella, L. E. *et al.*  $^7\text{Li}$  NMR chemical shift imaging to detect microstructural growth of lithium in all-solid-state batteries. *Chem. Mater.* **31**, 2762-2769 (2019).
- 36 Bayley, P. M., Trease, N. M. & Grey, C. P. Insights into electrochemical sodium metal deposition as probed with in situ  $^{23}\text{Na}$  NMR. *J. Am. Chem. Soc.* **138**, 1955-1961 (2016).
- 37 Gunnarsdóttir, A. B., Amanchukwu, C. V., Menkin, S. & Grey, C. P. Noninvasive In Situ NMR Study of “Dead Lithium” Formation and Lithium Corrosion in Full-Cell Lithium Metal Batteries. *J. Am. Chem. Soc.* (2020).
- 38 Zhang, W., Zhuang, H. L., Fan, L., Gao, L. & Lu, Y. A “cation-anion regulation” synergistic anode host for dendrite-free lithium metal batteries. *Sci. Adv.* **4**, eaar4410 (2018).
- 39 Pecher, O., Carretero-González, J., Griffith, K. J. & Grey, C. P. Materials’ methods: NMR in battery research. *Chem. Mater.* **29**, 213-242 (2017).

Supporting Information for Chapter 2

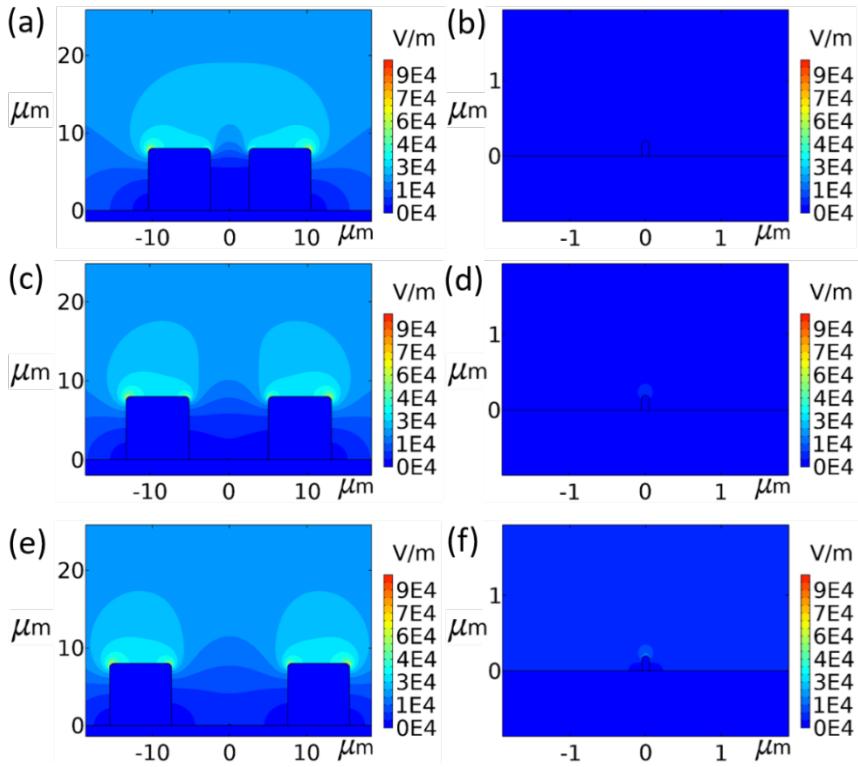


Figure S2.1 Schematic diagram of the electric field distribution of  $\text{BaTiO}_3$  (BTO) coated Cu with different block gaps. (a, b) with a distance of  $5 \mu\text{m}$  between blocks and zoomed-in figure, (c, d) with a distance of  $10 \mu\text{m}$  between blocks and zoomed-in figure, (e, f) with a distance of  $15 \mu\text{m}$  between blocks and zoomed-in figure.

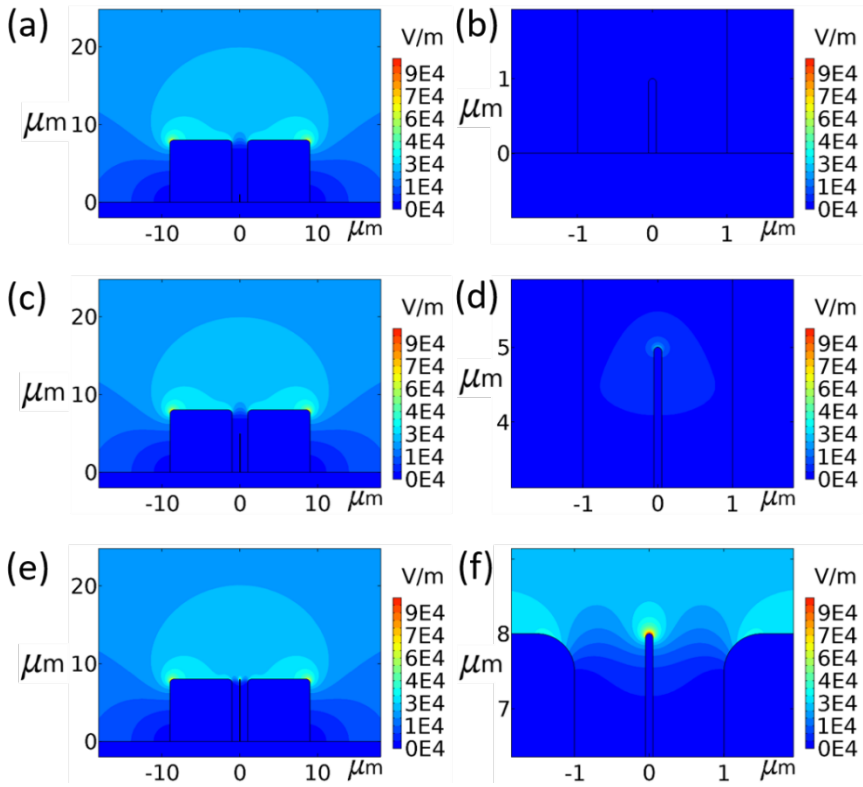


Figure S2.2 Schematic diagram of the electric field distribution of BaTiO<sub>3</sub> (BTO) coated Cu with different dendrite length. (a, b) with a dendrite length of 1  $\mu\text{m}$  and zoomed-in figure, (c, d) with a dendrite length of 5  $\mu\text{m}$  and zoomed-in figure, (e, f) with a dendrite length of 8  $\mu\text{m}$  and zoomed-in figure.

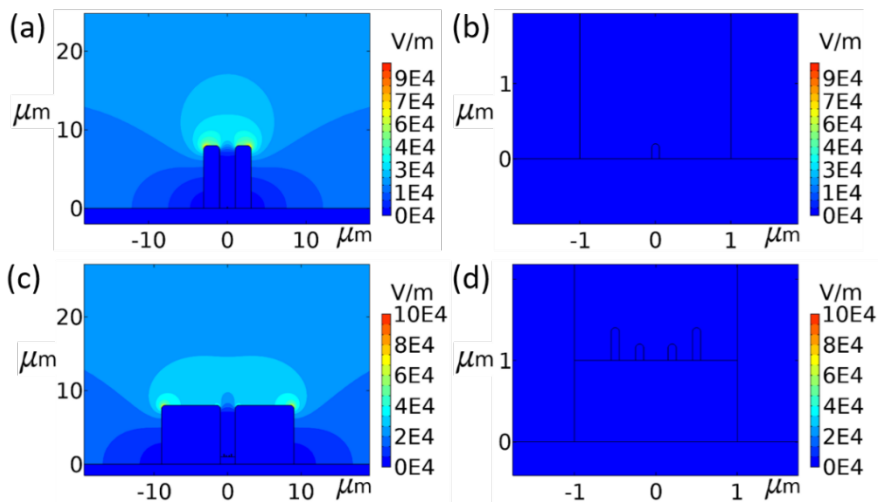


Figure S2.3 Schematic diagram of the electric field distribution of BaTiO<sub>3</sub> (BTO) coated Cu (a, b) with a block width of 2 μm and zoomed-in figure, (c, d) with multiple dendrites and zoomed-in figure.

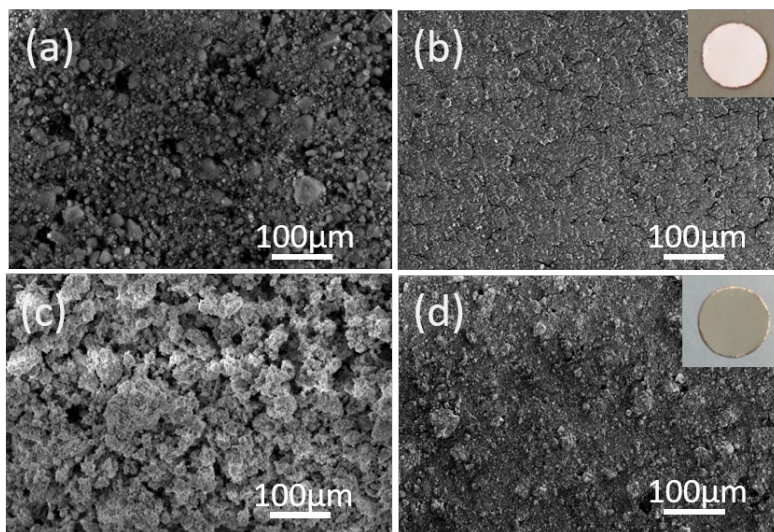


Figure S2.4 ball-milled starting materials and their coatings on copper. (a, b) AO and AO coated on Cu, (c, d) BTO and BTO coated on Cu. Insets are the digital image of the electrode.

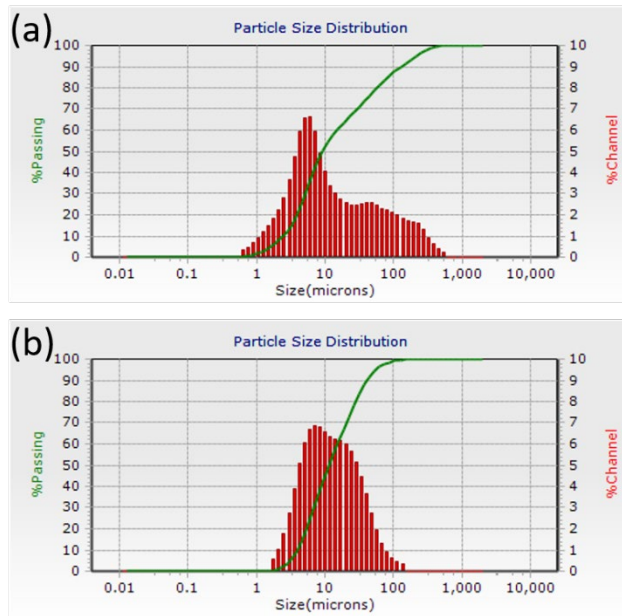


Figure S2.5 Particle size distribution of (a) BTO and (b) AO as obtained using the Dynamic Light Scattering technique.

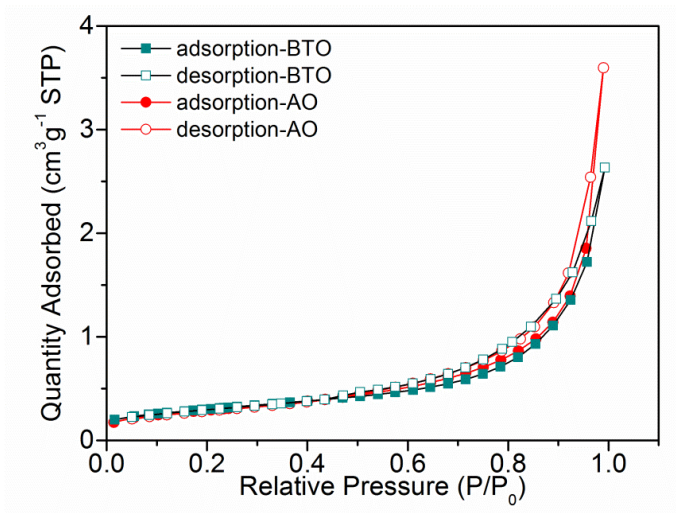


Figure S2.6 Nitrogen adsorption/desorption isotherms at 77 K of BTO and AO materials.

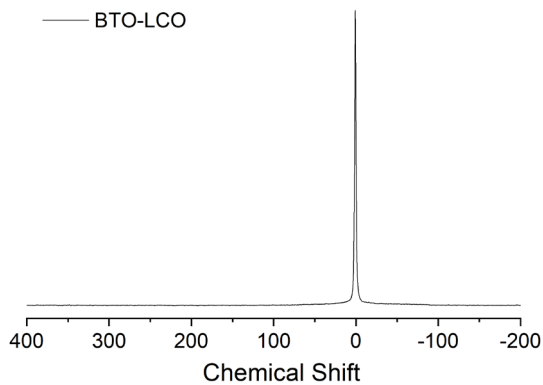


Figure S2.7 Static  $^7\text{Li}$  NMR spectrum measured with a wide spectral window of a fresh BTO-LCO battery.

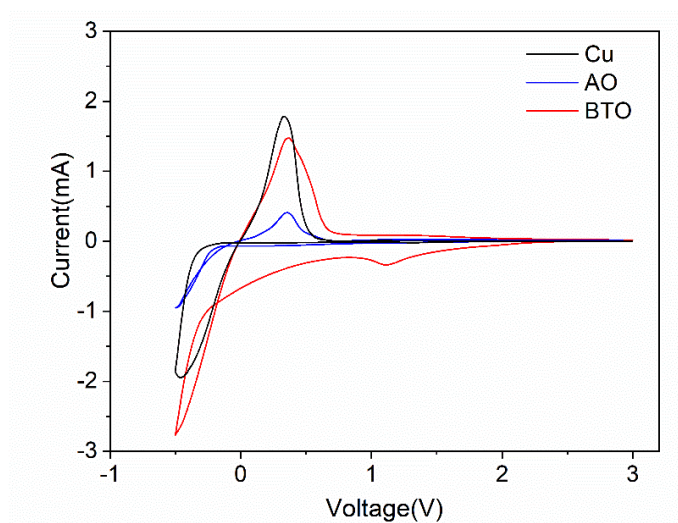


Figure S2.8 Cyclic voltammetry performance of different electrodes with a scan rate of  $1\text{mV s}^{-1}$  in the range of -0.5 V to 3 V.

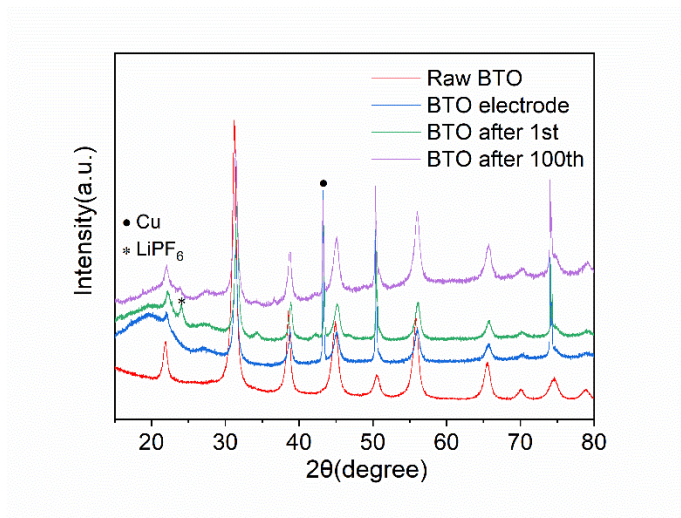


Figure S2.9 XRD patterns of BTO raw material and BTO electrodes before and after 1<sup>st</sup> and 100<sup>th</sup> cycles.

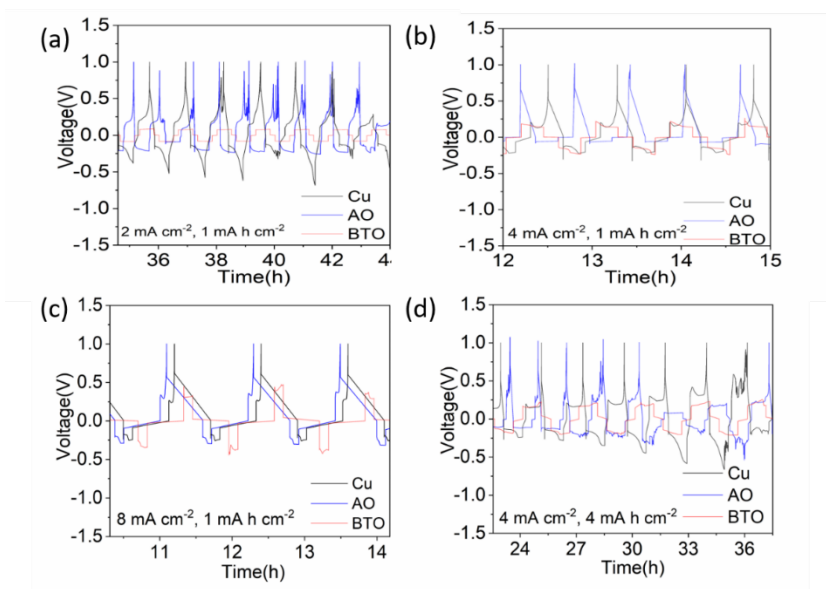


Figure S2.10 Detailed voltage profiles of the anode-less Cu, AO and BTO scaffolds vs a Li-metal anode. Evolution of the voltage during Li plating/stripping for the bare Cu and the AO and BTO scaffolds at different current densities (a)  $2 \text{ mA cm}^{-2}$ , (b)  $4 \text{ mA cm}^{-2}$ , (c)  $8 \text{ mA cm}^{-2}$  with a fixed areal capacity of  $1 \text{ mA h cm}^{-2}$ , and (d) an increased areal capacity of  $4 \text{ mA h cm}^{-2}$  at a current density of  $4 \text{ mA cm}^{-2}$ .

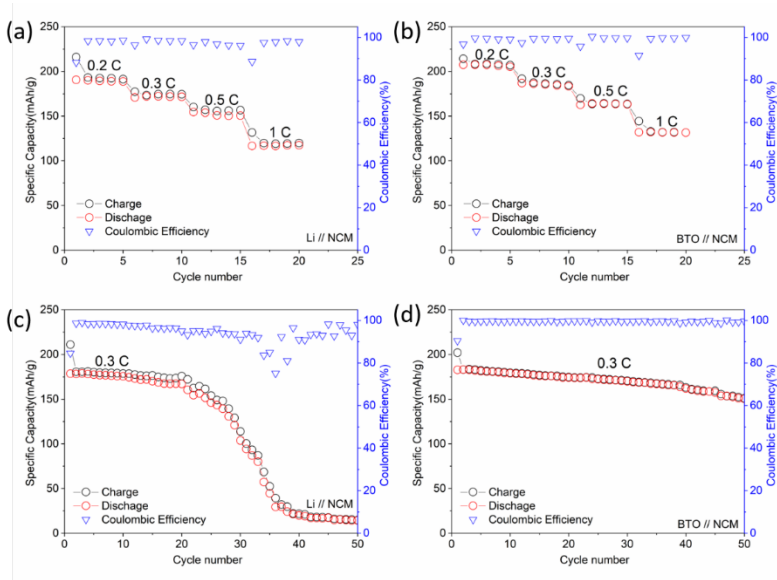


Figure S2.11 Cycling performances and coulombic efficiency of Li-metal and BTO scaffold when paired with NCM cathode. (a, b) Rate test from 0.2 C to 1 C. (c, d) Cycling test at 0.3 C.

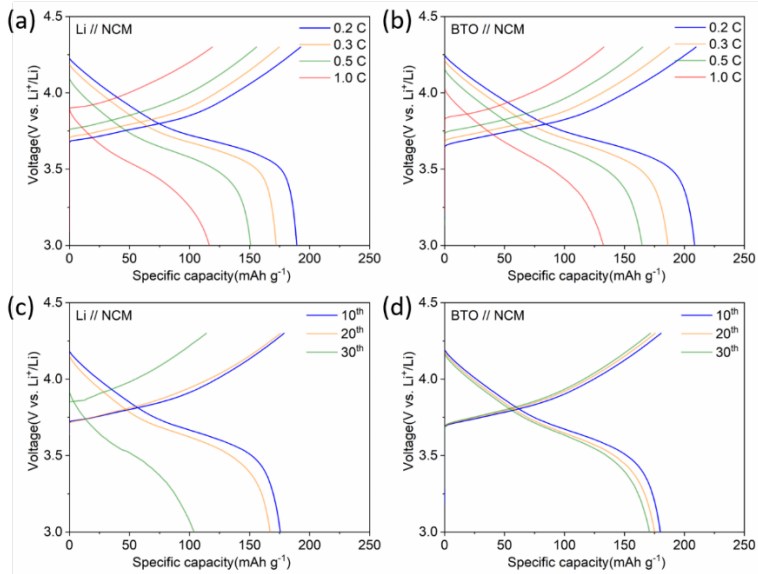
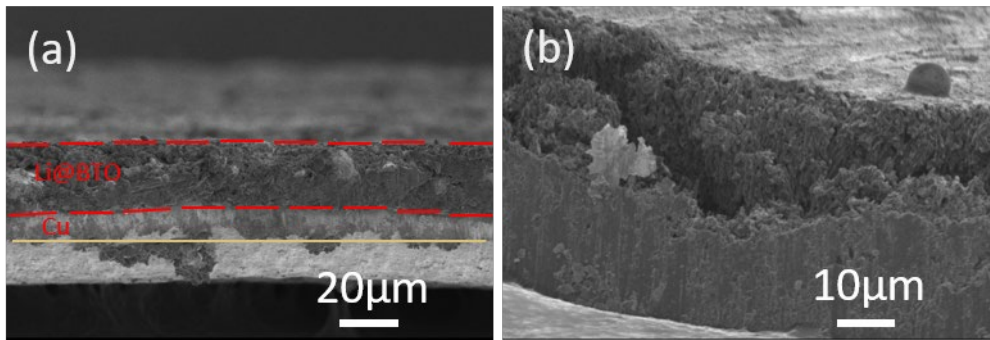


Figure S2.12 Voltage profiles of Li-metal and BTO scaffold when paired with NCM cathode. (a, b) Voltage profiles when cycled with different current densities. (c, d) Voltage profiles of different cycles when cycled at 0.3 C.





**Figure S2.13** Cross-section of BTO (a) and Cu (b) electrode after depositing 1 mA h cm<sup>-2</sup> Li-metal at a current density of 2 mA cm<sup>-2</sup>.

## Chapter 3 High Dielectric Barium Titanate Skeleton for All-Solid-state Lithium-Metal Battery

**This chapter is based on:**

**Chao Wang**, Ming Liu, Lars Bannenberg, Michel Thijs, Frans G.B. Ooms, Swapna Ganapathy and Marnix Wagemaker, High Dielectric Barium Titanate Skeleton for All-Solid-state Lithium-Metal Battery, To be submitted.

### Abstract

Lithium metal with high theoretical capacity and low negative potential is considered as the potential candidate to overcome the energy density issues for all-solid-state batteries. However, lithium filament growth and its induced solid electrolyte decomposition pose severe challenges to current solid-state Li-metal batteries. A 3D high dielectric matrix for solid-state Li metal battery is investigated, aiming to take away the focused electric field and thereby intrinsically alleviate dendrite growth. Symmetrical Li-metal cycling in the barium titanate based high dielectric skeleton results in an ultra-small over-potential of only 48 mV at a high current density of  $1 \text{ mA cm}^{-2}$  under the capacity of  $2 \text{ mA h cm}^{-2}$  over 1700 hours. Moreover, the 3D high dielectric skeleton improves the Coulombic efficiency and cycling life of full cells, which suppresses electrolyte decomposition, as examined by solid-state NMR. Thereby the high dielectric suppression of dendrites is brought forwards as a promising and practical strategy for the development of Li-metal all-solid-state batteries.

### 3.1 Introduction

With the development of the current technologies, the requirements of battery energy density and safety are rising.<sup>1,2</sup> State-of-the-art liquid-based batteries pose liquid leakage and fire hazard risks.<sup>3-5</sup> The solid-state battery is a promising candidate for next-generation battery design being intrinsically safer, however, so far the practical energy density is lower as compared with liquid-based batteries.<sup>6,7</sup> In theory, the energy density of solid-state batteries may be increased by replacing graphite with a lithium-metal anode, having a theoretical specific capacity of 3860 mA g<sup>-1</sup>.<sup>8</sup>

However, there are two interlinked challenges with Li-metal anodes: (i) inhomogeneous lithium metal deposition upon charge that drives dendrite formation, ultimately resulting in a short-circuit and (ii) electrolyte decomposition due to the strongly reducing potentials of Li-metal.<sup>8-12</sup> Early hope was that solid electrolytes, replacing liquid electrolytes, could prevent both detrimental processes, through their high shear modulus as compared to Li-metal and electrochemical stability, however, research has demonstrated that both present formidable challenges for Li-metal solid-state batteries. Direct evidence from in situ X-ray tomography has shown that lithium dendrites/filaments tend to grow along with the grains and grain boundaries of the inorganic solid-state electrolyte,<sup>13-15</sup> demonstrating that inhomogeneous lithium metal deposition causes short-circuiting even in solid-state batteries.<sup>13,16</sup> It appears that the mechanism of dendrite growth is very different in solid-electrolytes as compared to liquid electrolytes,<sup>17</sup> where one important factor appears to be the applied pressure that typically exceeds the yield strength of Li-metal (about 0.8 MPa). Dendrite growth is believed to be induced by preferential deposition on local inhomogeneities like grain boundaries and voids present at the Li-metal electrolyte interfaces, resulting in local hotspots of high current, and the much larger molar volume of Li-metal, as compared to Li in solid electrolytes,<sup>18</sup> has been suggested to cause local expansion causing cracks with Li metal deposits.<sup>19</sup> The quick polarization before a real short circuit of solid-state batteries<sup>20</sup> and the generally observed rise in battery polarization<sup>21</sup> underlines the interlinked problem that most solid electrolytes are not stable towards the low reduction potential of Li-metal. Indeed most solid electrolytes are predicted to be unstable towards Li-metal,<sup>21,22</sup> which is especially exposed through the high surface area of dendrite filaments in solid-state batteries.

This motivates strategies to prevent inhomogeneous Li-metal plating, through enhancing Li-ion mobility and/or reducing the local current density,<sup>23-31</sup> minimizing interfacial inhomogeneities,<sup>32</sup> increasing the adhesion by improving the wettability of Li-metal<sup>24</sup> and designing of SEI<sup>23</sup> and buffer layers<sup>24</sup> to promote interface adhesion and homogeneity. All

these above methods can alleviate the growth of lithium dendrites to a certain extent, however, do not take away the intrinsic driving force for dendrite growth. Under normal conditions, dendrites grow at sharp edges because of a larger surface charge density, which through Gauss law leads to focusing electrical field lines.<sup>33</sup> An alternative approach to achieve this effect is to take away these inhomogeneous electric fields, through the introduction of a high dielectric material as a 3D scaffold. The high polarizing power of a high dielectric, establishes an effective immobile surface (space) charge density  $\rho_{charge}$ , opposing the applied field in the battery, that scales with the dielectric constant ( $\nabla \cdot D = \rho_{charge}$  where  $D = \epsilon_0 \epsilon_r E$ ,  $\epsilon_0$  and  $\epsilon_r$  the vacuum and relative permittivity and  $E$  the electrical field). As a consequence, the electrical field lines focus towards the high dielectric (dictated by Gauss Law) leading to lowering of the divergence of the electrical field. At the tip of a dendrite near a high dielectric material, this effectively leads to loss of electrical field divergence, and thus to a lower local electrical field gradient.

To achieve this in practice, the high dielectric material is added to both the Li-metal electrode and solid sulfide electrolyte of a solid-state battery. Symmetrical Li-metal cycling in this high dielectric skeleton results in an ultra-low overpotential of only 48 mV at 1 mA cm<sup>-2</sup> up to 2 mA h cm<sup>-2</sup> capacity over 1700 hours. This composite anode has a specific capacity of 504 mA h g<sup>-1</sup>, taking into account both Li-metal and the dielectric material in the Li-metal anode. We demonstrate that the high permittivity of the skeleton suppresses dendrite growth, promoting homogeneous plating, thus damping the self-amplifying cycle of electrolyte decomposition and dendritic growth. Moreover, this 3D high dielectric skeleton results in an increase of Coulombic efficiency and cycle life in full cells. Solid sulphide electrolyte decomposition is restricted, as testified by the solid-state NMR experiments, rationalizing the improved performances. Thereby, this high dielectric concept is brought forwards as a strategy to suppress Li-metal dendrite formation in solid-state batteries and improve the cycle life.

## 3.2 Material and methods

### 3.2.1 Preparation of anode materials and solid-state electrolyte

Commercial BaTiO<sub>3</sub> (Euro Support B.V., denoted as BTO) and Al<sub>2</sub>O<sub>3</sub> (Sigma-Aldrich, denoted as AO) powder were used as the starting materials, because of their different dielectric constants. Firstly, metallic Lithium(20% wt) was heated in Nickel crucible at 300 °C for 0.5 h, and then BTO or AO (80% wt) powder was added in and mixed with the melted lithium metal. After 2 hrs mixing and heating, the prepared materials (BTOLi or AOLi composite) were collected for further measuring. The solid-state electrolyte Li<sub>6</sub>PS<sub>5</sub>Cl (denoted as LPSC)

was prepared by a simple solid-state reaction. The stoichiometric raw materials LiCl (Sigma-Aldrich),  $P_2S_5$  (Sigma-Aldrich), and  $Li_2S$  (Sigma-Aldrich) were used as the starting materials and were ball milled at 110 rpm, 2hrs with the  $ZrO_2$  coated jars using 18  $ZrO_2$  balls. After the ball milling, the precursor was sealed in a quartz tube with Ar and then annealed at 550 °C for 15 hours to obtain the  $Li_6PS_5Cl$  solid electrolyte. Commercial  $Li_4Ti_5O_{12}$  (denoted as LTO) was chosen as the cathode material to assemble half cells. LTO, LPSC and carbon black were ball milled in a mass ratio of 4:4:2 at 200 rpm, 6hrs to prepare the cathode mixture.

### 3.2.2 Characterization of the materials and the electrodes

Powder and pellet X-ray Diffraction (XRD) were measured with a  $2\theta$  range of 10 - 80° to identify the crystalline phases of the prepared materials using  $Cu_{K\alpha}$  X-rays (1.5406 Å at 45 kV and 40 mA) on an X'Pert Pro X-ray diffractometer (PANalytical). To prevent reaction with air, the samples were sealed in an airtight XRD sample holder in an Argon filled glove box. Ionic conductivities LPSC solid electrolyte and BTOLPSC mixture were measured by making wafers of their powder with a diameter of 10 mm. Stainless-steel current collectors were attached to both sides of the wafers and alternating current impedance measurements were conducted on an Autolab (Autolab PGSTAT302N) in the frequency range of 0.1 Hz to 100 kHz with a perturbation potential of 5 mV. Electronic conductivities of LPSC solid electrolyte and BTOLPSC mixture were measured by using Direct Current Polarization method. A one-side blocking cell (like Li-In/LPSC/Stainless steel) was assembled and tested with the Autolab. Lithium metal plating wafer electrodes for SEM test were prepared by (dis)charging the solid-state cells for several cycles. Before scanning electron microscope (SEM) imaging, the wafer electrodes were pressed out from the  $Al_2O_3$  ceramic cylinder in the glovebox. Subsequently, the samples were transferred into a SEM (JEOL JSM-6010LA) machine under dry Argon condition, and images were taken using an accelerating voltage of 2-10 kV.

### 3.2.3 Assembly and electrochemical tests of the cells

Symmetric solid-state cells (AOLi/LPSC/AOLi, BTOLi/LPSC/BTOLi, BTOLi/BTOLPSC/BTOLi, and Li/LPSC/Li) were assembled in an argon-filled glove box in the following steps: 200 mg of LPSC or BTOLPSC was pressed tightly under the pressure of 300 MPa as the electrolyte layer, and then 10 mg of BTOLi or AOLi (or Li metal disk with a diameter of 7mm, 0.5 mm thickness) was added to both sides of the electrolyte layer, separately. After that, 2 MPa pressure was used to press these three layers together. The (dis)charge processes of these symmetric cells were performed on Maccor battery tester (Model 4300) in the glovebox at room temperature. The cells were cycled in the potential range of -4.0 – 1.0 V (vs. Li/Li<sup>+</sup>)

with the current densities from  $0.1 \text{ mA cm}^{-2}$  to  $8 \text{ mA cm}^{-2}$ . The electrochemical impedance spectroscopy (EIS) of cells were measured before and after cycling on an Autolab (Autolab PGSTAT302N) in the frequency range of 0.1 Hz to 100 kHz. A perturbation of 5 mV was applied. The Li/LPSC/LTO and BTOLi/BTOLPSC/LTO half cells were assembled in the same way and were cycled within the potential range of 1.0 - 2.5 V (vs. Li/Li<sup>+</sup>) at  $0.31 \text{ mA cm}^{-2}$  at room temperature in the glovebox.

### 3.2.4 Electrical field calculations

All simulations were done in COMSOL Multiphysics 5.5. One basic 2D voltaic cell was constructed to represent a solid-state electrolyte cell. Using the electrostatics software, the electric field throughout the cell was calculated. Several materials were defined by their dielectric constant. As a standard, the electrodes used were lithium which was taken from the COMSOL material's library. This work looks at four different types of cells, each with different electrodes and electrolytes. Electrodes of lithium metal, Li-BaTiO<sub>3</sub>(BTOLi) or Li-Al<sub>2</sub>O<sub>3</sub>(AOLi) ( $10 \mu\text{m} \times 100 \mu\text{m}$ ) were placed at two sides of the solid electrolyte Li<sub>6</sub>PS<sub>5</sub>Cl(LPSC) or Li<sub>6</sub>PS<sub>5</sub>Cl and BaTiO<sub>3</sub> mixture(BTOLPSC) ( $30 \mu\text{m} \times 100 \mu\text{m}$ ) to approximate the situation of the real battery. A lithium dendrite is placed on the top of the electrode, represented by a rectangular shape ( $1 \mu\text{m} \times 2 \mu\text{m}$ ) with a hemispherical tip. A randomly distributed high dielectric material, different amounts of randomly distributed BTO and AO spheres, varying in sizes between 1 and  $8 \mu\text{m}$ , were simulated in this model. The relative permittivity's of BTO, AO and the LPSC electrolyte are 4000, 8 and 5, respectively.

## 3.3 Results and discussions

### 3.3.1 Electrical field calculations

To obtain insight in how the dielectric constant of filler particles dispersed in the Li-metal and/or solid electrolyte influence the electric field gradient, the electrical field is calculated in two dimensions in the voltage range of 0-1 V, using COMSOL Multiphysics 5.5. This is performed for Li-metal inhomogeneities (representing dendritic features) in four different cell configurations as shown in **Figure 3.1** and **Figure S3.1**. (1) Li-metal electrodes combined with Li<sub>6</sub>PS<sub>5</sub>Cl (LPSC) as solid electrolyte (**Figure 3.1a, b**), (2) Li-metal mixed with spherical particles of Al<sub>2</sub>O<sub>3</sub> (AOLi) combined with Li<sub>6</sub>PS<sub>5</sub>Cl (LPSC) as solid electrolyte (**Figure 3.1c, d**), (3) Li-metal mixed with spherical particles of BaTiO<sub>3</sub> (BTOLi) combined with Li<sub>6</sub>PS<sub>5</sub>Cl (LPSC) as solid electrolyte (**Figure 3.1e, f**) and (4) the same electrodes as (3) in combination with the Li<sub>6</sub>PS<sub>5</sub>Cl (LPSC) as solid electrolyte also mixed with BTO (**Figure 3.1g – 3.1j**). The comparison between BaTiO<sub>3</sub> (BTO) and Al<sub>2</sub>O<sub>3</sub> (AO), with a size distribution of between 1 and

8  $\mu\text{m}$  to represent the practical situation evaluated experimentally in this study, is introduced to investigate the impact of the high dielectric constant, which equals to 4000 and 8 respectively, in comparison to 5 for the LPSC solid electrolyte.

As observed in **Figure 3.1a** and **3.1b** the electrical field gradient is much larger near the tip of an inhomogeneity with a rectangular shape (1  $\mu\text{m}$  x 2  $\mu\text{m}$ ) with a hemispherical tip (representing a Li-dendrite) at the Li-metal surface. Driven by the larger surface charge density present at the sharp electronically conducting feature, the electrical field gradient increases dramatically at the tip of the Li-metal, which thus focusses the electrical field lines to the tip of the Li-metal dendrite. This facilitates Li-ions deposition at the tip of the dendrite representing the driving force for dendrite formation (independent of the thickness of the Li-metal electrode as can be confirmed by **Figure S3.1a** and **S3.1b**). As shown in **Figure 3.1c** and **3.1d**, AO spheres (relative permittivity 8, slightly higher than that of the LPSC electrolyte) and in **Figure 3.1e** and **3.1f**, BTO spheres (relative permittivity 4000, much higher than that of the LPSC electrolyte) are added into Li metal to form the AOLi or BTOLi composite electrodes. For AOLi and BTOLi, the electrical field gradient near the top of the spheres remain large (**Figure 3.1d** and **3.1f**), and thus can act as nucleation points for lithium deposition. The situation changes if the Li-metal is stripped, and the electrical field gradient is calculated for a dendritic feature in the void space of the AO or BTO matrix, as shown in **Figures S3.1c – S3.1f**. In the void space of an AO stripped electrode, the electrical field gradient near the tip of the dendrite decreases slightly (**Figure S3.1d**) in comparison with a dendrite in the solid electrolyte (**Figure S3.1b**), however, most interestingly, in the void space of a BTO matrix, the electrical field gradient at the tip of the dendrite disappears (**Figure S3.1f**). The low polarizability of the AO “leaves” the electrical field gradient at the Li-metal tip, whereas the high polarizability of the BTO “pulls” the electrical field lines away from the Li-metal tip towards the surface of the BTO itself. This suggests that the presence of high dielectric spheres in the vicinity of a Li-metal filament takes away the driving force for Li deposition at the tip or sharp features, thus taking away the driving force for tip driven dendrite growth.



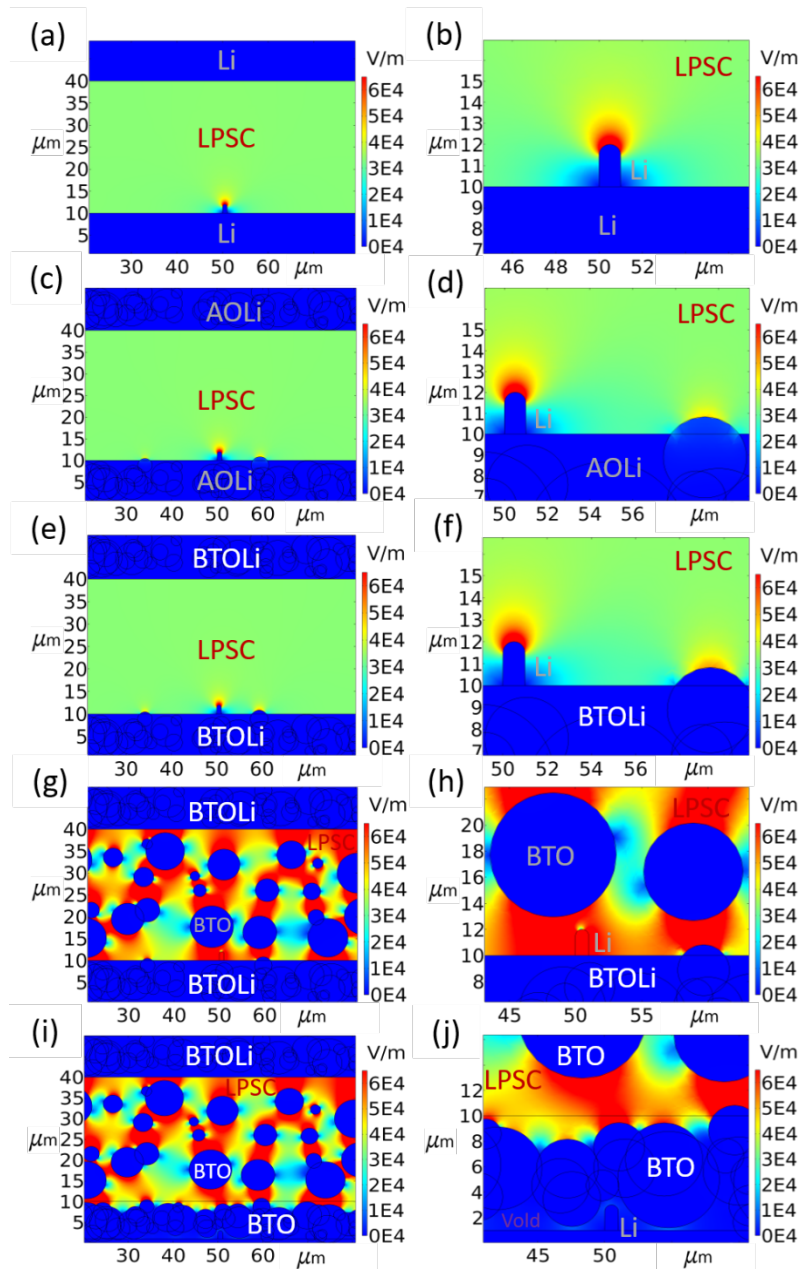


**Figure 3.1** Calculated electric field gradient around Li metal inhomogeneities in 2D models having different configurations of symmetric lithium metal cells with different dielectric materials. (a, b) Li/Li<sub>6</sub>PS<sub>4</sub>Cl(LPSC)/Li cell, (c, d) Li-Al<sub>2</sub>O<sub>3</sub>(AOLi)/LPSC/AOLi cell, (e, f) Li-BaTiO<sub>3</sub>(BTOLi)/LPSC/BTOLi cell, (g, h, i, j) BTOLi/LPSC and BTO mixture(BTOLPSC)/BTOLi cell.

In **Figure 3.1g – 3.1j**, BTO spherical volumes are also added into the solid electrolyte region. **Figure 3.1g** and **3.1h** represent the situation that a dendrite penetrates the solid electrolyte region, where the high dielectric BTO has a distinct impact on the electrical field gradient. Also in this case the high electrical field gradients are pulled towards the high dielectric, lowering the field gradient at the tip of dendritic features penetrating the solid electrolyte (**Figure 3.1h**). Based on this one could speculate that dendrites grow towards the BTO, whereby it poses a barrier for dendrites to continue their growth toward the counter electrode. Simultaneously, the electric field is also simulated in the stripped BTOLi/BTOLPC cell (**Figure 3.1i** and **3.1j**), and the electrical field gradient at the tip of the dendrite has been taken away due to the presence of high dielectric BTO material, which can facilitate the none filament growth process and longer cycling life. Based on these simulations, the hypothesis is brought forward that a high dielectric 3D matrix, with lithium metal deposited in its voids, promotes homogeneous Li-metal growth, and that the high dielectric material added to the solid electrolyte may hinder dendrite growth through the solid electrolyte region. This would lead to much less interface area between Li-metal and solid electrolyte interface, suppressing electrolyte decomposition, promoting cycle life and lowering the chance of dendrites reaching the cathode creating a short circuit.

### 3.3.2 Electrode preparation

In order to experimentally investigate the impact of high dielectric additives in Li-metal solid-state batteries, commercial AO (low dielectric constant) and BTO (high dielectric constant), having a similar particle size distribution, were prepared and compared to isolate the impact of the dielectric constant from the impact of adding an inactive filler. As shown in the scanning electron microscopy (SEM) images (**Figure 3.2a** and **3.2d**), micron-sized BTO and AO materials, having a particle size between 1 and 100  $\mu\text{m}$  were used to prepare the composite electrodes. BTOLi and AOLi composites were prepared by melting lithium metal and mixing with BTO or AO powder in a Nickel crucible at 300  $^{\circ}\text{C}$  for 2 hrs, the details of which can be found in the methods section. **Figure 3.2b** and **3.2e** indicate that the molten lithium metal wets to the surface of the BTO and AO particles due to the lower wetting energy barrier. Both materials are characterized by X-ray Diffraction (XRD) (**Figure S3.2**), indicating that BTO is stable in contact with Li-metal, whereas the AO displays some reactivity, leading to the formation of a lithiophilic Li-Al-O interface.<sup>34</sup> After pressing the as-prepared materials to a wafer layer under a mild pressure of 2 MPa, the 20%Li-BTO composite electrode (**Figure 3.2c**) shows a relatively smooth surface as compared to the 20%Li-AO pellet (**Figure 3.2f**).

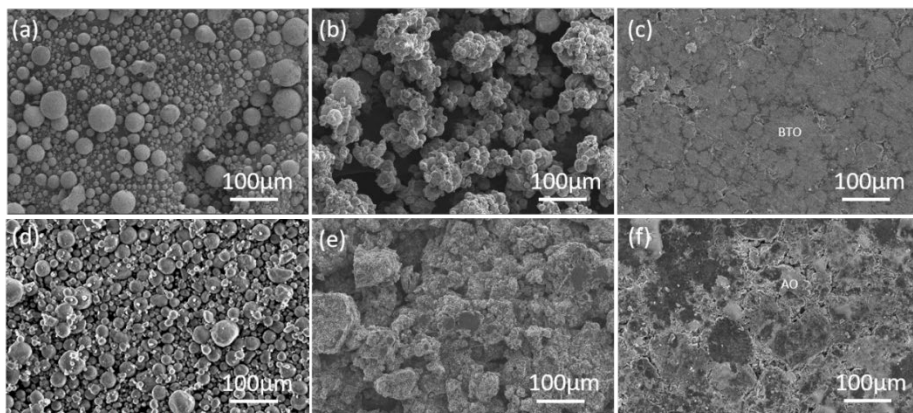


**Figure 3.2** Morphologies of pristine materials and as prepared composite Li-metal electrodes. (a-c) SEM images of pure BaTiO<sub>3</sub>(BTO), 20%Li-BTO mixture and as-prepared BTOLi electrode, respectively. (d-f) SEM images of pure Al<sub>2</sub>O<sub>3</sub>(AO), 20%Li-AO mixture and AOLi electrode, respectively.

To determine the capacity of the prepared composite electrodes, the electrodes were assembled in a solid-state battery, using argyrodite Li<sub>6</sub>PS<sub>5</sub>Cl (LPSC) as solid electrolyte (see the Methods section for the preparation and XRD of the as-prepared material in **Figure S3.3**) and Li-metal as the counter electrode. After stripping Li completely from the BTOLi and AOLi composite electrodes with a current density of 0.1 mA cm<sup>-2</sup>, a considerable specific capacity of 504 and 174 mA h g<sup>-1</sup> was obtained (cutoff voltage 1 V vs Li/Li<sup>+</sup>), respectively, taking into account the weight of the AO/BTO matrix and Li metal (**Figure S3.4 a, b**). For the 20%Li-BTO and 20%Li-AO composites (**Figure S3.4 c, d**), the smooth charging curve without second plateau indicates that the total capacity is provided by metallic lithium inside the skeleton only. In addition, the differential capacity curve further proves that the reaction has occurred around 0.02 V which was related to the lithium stripping process. This capacity could be further improved by optimizing the composites active materials to matrix ratio.

### 3.3.3 Electrochemical evaluation of the composite electrodes in symmetrical cells

To determine the critical current density of dendrite formation, symmetrical batteries were cycled under an increasing current density. In **Figure 3.3a** the results are shown for symmetrical Li/LPSC/Li, AOLi/LPSC/AOLi, BTOLi/LPSC/BTOLi and also BTOLi/BTOLPSC/BTOLi cells, cycled with a current density from 0.1 mA cm<sup>-2</sup> to 1.0 mA cm<sup>-2</sup>, followed by 0.1 mA cm<sup>-2</sup> cycling (detailed information can be found in **Table S3.1**). For the Li/LPSC/Li and AOLi/LPSC/AOLi cells, this results in a short circuit already after three cycles at 0.1 mA cm<sup>-2</sup> (detailed voltage profiles are provided in **Figure S3.5**). This cell failure is most likely due to facile dendrite formation, presumably supported by the relatively high electronic

conductivity of LPSC ( $9.12 \times 10^{-8} \text{ S cm}^{-1}$ ).<sup>30,35,36</sup> The electrical field gradient calculations, shown in **Figure 3.1** and **Figure S3.1**, suggest that the large electrical field gradient at Li-metal inhomogeneities is an important driving force for dendrite growth as commonly assumed.<sup>8,37</sup>

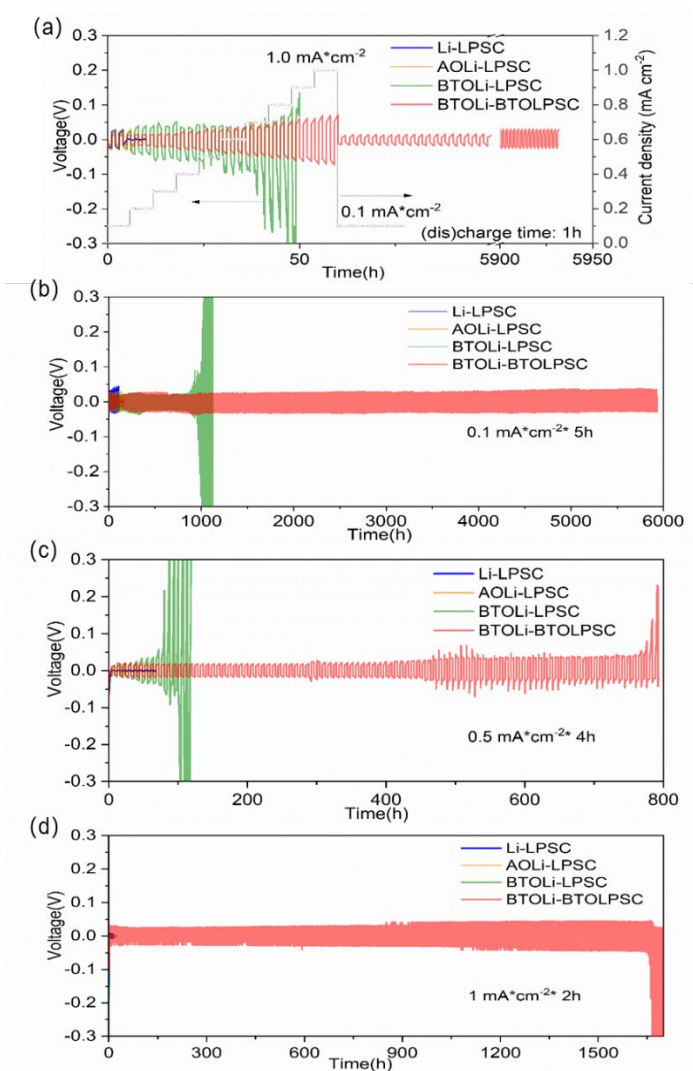


**Figure 3.3** Critical current density and cycling test of symmetric cells using bare Li electrodes, AOLI or BTOLI composite electrodes and LPSC or BTOLPSC electrolytes. (a) Voltage profile at an increasing current density from  $0.1 \text{ mA cm}^{-2}$  to  $1.0 \text{ mA cm}^{-2}$  followed by  $0.1 \text{ mA cm}^{-2}$  cycling (discharge time was 1h). Voltage profiles of cycling performance at a current density of (b)  $0.1 \text{ mA cm}^{-2}$  with a capacity of  $0.5 \text{ mA h cm}^{-2}$ , (c)  $0.5 \text{ mA cm}^{-2}$  with a capacity of  $2.0 \text{ mA h cm}^{-2}$ , (d)  $1 \text{ mA cm}^{-2}$  with a capacity of  $2.0 \text{ mA h cm}^{-2}$ , respectively.

The addition of the high dielectric material in the BTOLi/LPSC/BTOLi cell, results in a higher critical current density of  $0.5 \text{ mA cm}^{-2}$  with an average voltage hysteresis of 60 mV (**Table S3.1** and **Figure S3.5c**). We propose this is due to the presence of the high dielectric constant BTO that lowers the electrical field gradient at the surface of the Li-metal (**Figure S3.1 e, f**), and not due to the presence of the filler itself because the low dielectric AO filler does not improve the critical current. However, when the plating has filled the BTO matrix dendrite formation may be initiated by the high electrical field gradient in the solid electrolyte region (**Figure 3.1 g, h**). To hide this, the BTO is also added into the electrolyte layer. To determine the impact of the BTO fraction on the conductivity of the solid electrolyte composite, electrochemical impedance spectroscopy (EIS) is performed for different weight ratios between BTO and LPSC, shown in **Figure S3.6**. The resulting ionic conductivities of pure LPSC electrolyte, 15%BTO-LPSC and 30%BTO-LPSC mixtures are 5.6, 4.5 and  $0.73 \text{ mS cm}^{-1}$ , respectively. Due to the relatively low ionic conductivity of 30%BTO-LPSC mixture, 15%BTO-LPSC was chosen as the electrolyte for further experimental evaluation.

The BTOLi/BTOLPSC/BTOLi cell can resist the highest current density, easily handling a current density of  $1.0 \text{ mA cm}^{-2}$  with a potential hysteresis of 65 mV as shown in **Figure 3.3a** and **Table S3.1**). Subsequently, cycling at  $0.1 \text{ mA cm}^{-2}$  can be maintained for at least 6000 hrs with an ultra-low overpotential of 21 mV after 6000 hrs. This much better rate capability suggests that dendrite formation and growth is suppressed, in line with the electrical field calculations that demonstrate that the presence of the high dielectric BTO filler removes the electrical field gradients at inhomogeneous Li-metal features, both in the anode and in the solid electrolyte region. Han et al indicated that a higher electronic conductivity of the solid electrolytes promotes dendrite formation<sup>38</sup> on the other hand a high Li-ion conductivity suppresses dendrite formation. The electronic conductivities of the LPSC and BTOLPSC solid electrolytes amount  $9.12 \times 10^{-8} \text{ S cm}^{-1}$  and  $1.14 \times 10^{-8} \text{ S cm}^{-1}$ , respectively, as determined by the direct-current polarization method. As expected, mixing LPSC with the electronically insulating BTO lowers the overall electronic conductivity which may suppress dendrite formation. Oppositely, it also lowers the overall Li-ion conductivity from 5.6 for LPSC to  $4.5 \text{ mS cm}^{-1}$  for the BTOLPSC composite, which promotes dendrite formation. It is not possible to conclude what is the overall impact of these counteracting properties on dendrite formation. However, the electrical field gradient calculations indicate that the BTO in the solid electrolyte region suppresses the driving force for dendrite formation, providing a rationale for the larger critical current and more stable cycling observed in **Figure 3.3**. To further test the BTOLi composite in combination with the BTOLPSC electrolyte, a symmetric Li-metal cell was cycled to higher current densities, from  $0.1 \text{ mA cm}^{-2}$  to  $8.0 \text{ mA cm}^{-2}$  under a fixed capacity of  $0.1 \text{ mA h cm}^{-2}$  limited by a 1.0 V vs Li/Li<sup>+</sup> stripping cut-off voltage as shown

in **Figure S3.7**, which demonstrate this solid-state battery can prevent a short circuit and remains to have low overpotentials. Under all conditions, higher current density, larger cycling capacity (tested up to  $2 \text{ mA h cm}^{-2}$ ) and cycling duration the BTOLi/BTOLPSC/BTOLi cell outperform the other cell configurations as confirmed by **Figures 3.3a-d** and **Figures S3.7-10**). The areal capacity of  $2 \text{ mA h cm}^{-2}$  is among the highest reported in the open literature for solid-state Li metal batteries, as shown in **Table S3.2**. The ultra-low overpotential of only 11 mV, 36 mV and 48 mV under current densities of 0.1, 0.5 and  $1.0 \text{ mA cm}^{-2}$  indicates more uniform Li-metal plating and stripping as a consequence of introducing the high dielectric BTO.

Electrochemical impedance spectroscopy (EIS) measurements are shown in **Figure 3.4**, conducted to evaluate the cell resistance upon cycling at  $0.1 \text{ mA cm}^{-2}$  for 5 h (**Figure 3.4**). The results found for the four configurations is provided in **Table S3.3**. The quarter-circle and semicircle obtained in the high-frequency range ( $100 \text{ kHz} - 10 \text{ Hz}$ ) can be ascribed to the SEI and charge-transfer resistance<sup>30,34</sup>. Already before cycling, the spontaneous (electro)chemical reaction of Li-metal with LPSC results in less conductive decomposition products ( $\text{Li}_2\text{S}$ ,  $\text{LiCl}$  and  $\text{Li}_3\text{P}$ ),<sup>8,37,39</sup> which are responsible for the relatively high interfacial resistance of  $\approx 159 \Omega$ . Three other configurations lead to a slightly smaller but comparable interface resistance ( $132 \Omega$  for AOLi cell,  $122 \Omega$  for BTOLi cell and  $116 \Omega$  for BTOLi-BTOLPSC cell). As expected, after 1, 10 and 100 cycle(s) the interface resistance of both the Li/LPSC and AOLi/LPSC interfaces increase significantly, which is known to be the consequence of further decomposition reactions amplified by Li-dendritic growth and contact loss.<sup>8,30,40</sup> The presence of BTO, especially in both Li-metal and LPSC solid electrolytes, suppresses the increase in interface resistance (for the BTOLi-BTOLPSC cell  $95 \Omega$  after 1 cycle,  $93 \Omega$  after 10 cycles and  $99 \Omega$  after 100 cycles, see **Table S3.3**). This can be rationalized by the suppression of dendrites, leading to less LPSC decomposition products, and thus a better ability to maintain a low interface resistance, in agreement with the smaller overpotential during cycling and more stable cycling observed in **Figure 3.3**.

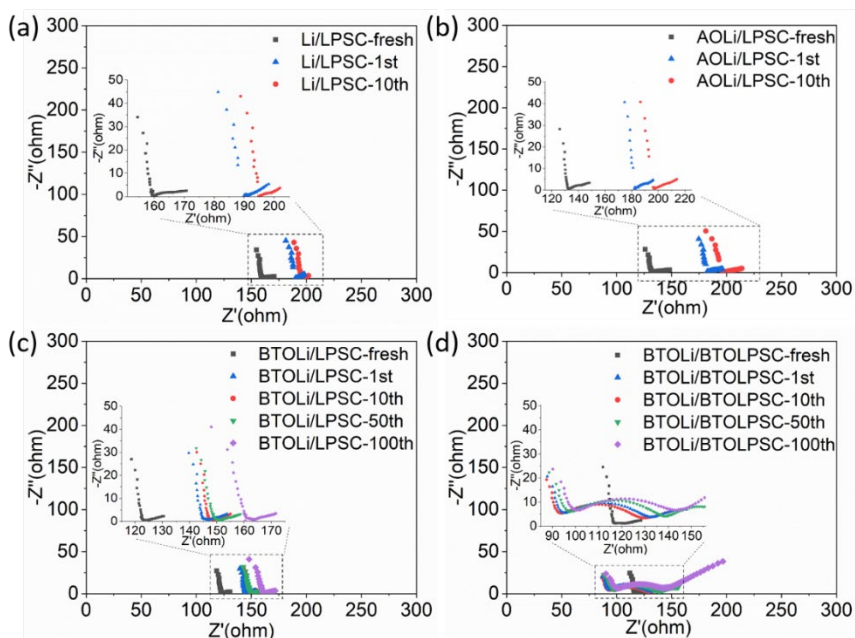


**Figure 3.4** Electrochemical impedance spectroscopy (EIS) Nyquist plots of the solid-state symmetric cells after different numbers of cycling at  $0.1 \text{ mA cm}^{-2}$  for 5 h. (a) Li-metal with LPSC (Li-LPSC), (b) Li-metal-AO composite with LPSC (AOli-LPSC), (c) Li-metal-BTO composite with LPSC (BTOLI-LPSC) (d) Li-metal-BTO composite with the LPSC-BTO composite (BTOLI-BTOLPSC).

### 3.3.4 Li metal morphology after cycling

To compare the surface morphologies of the bare Li anode with the composite AOli and BTOLI anodes, SEM characterization was conducted after 10 cycles at a current density of  $0.1 \text{ mA cm}^{-2}$  for 5 h, the results of which are shown in **Figure 3.5**. (The SEM images of the LPSC electrolyte, and the LPSC and BTOLPSC pallets are shown in **Figure S3.11**). SEM images of the pristine Li foil, AOli and BTOLI electrodes manifest that the Li foil and BTOLI electrodes have a relatively smooth surface, while some voids are observed for the AOli electrode (**Figure 3.5a, d, g, j**). After 10 cycles, the SEM image for the Li-metal anode, **Figure 3.5b**, shows a micro-sized needle-like lithium dendrite on the surface of the lithium metal side, and on the electrolyte side (**Figure 3.5c**) a micro-sized sharp electrodeposit penetrates the LPSC electrolyte. Also at the surface of the AOli and BTOLI electrodes, **Figures 3.5e** and **3.5h** respectively, and on the LPSC electrolyte sides, **Figure 3.5f** and **3.5i** respectively, large dendritic features and very rough surfaces are observed, demonstrating that dendrites can penetrate the solid electrolyte, preferentially growing through pores and cracks.<sup>38</sup> For the BTO modified LPSC both the anode side, **Figure 3.5k**, and electrolyte side, **Figure 3.5l**, show

more uniformly deposited Li-metal. and much less protrusion and pulverization. This supports the hypothesis that the BTO leads to more homogeneous Li-metal deposition, and additionally suggests that the BTO matrix may also suppress delamination due to the large volume changes. Both aspects are crucial to achieving stable Li-metal cycling in combination with solid electrolytes.<sup>15,41</sup>

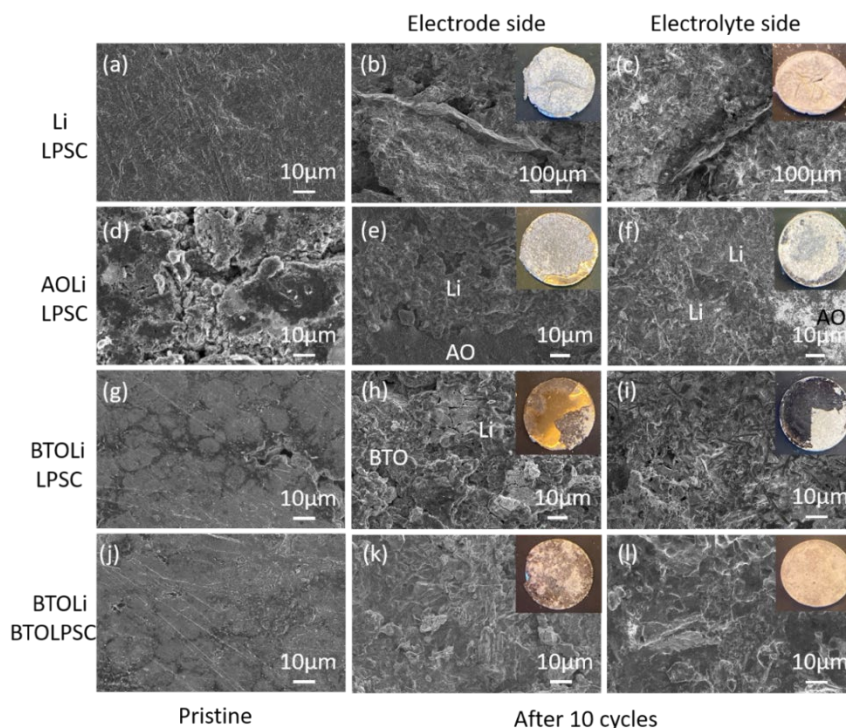


**Figure 3.5** Morphologies of Li electrodeposits on a bare Li-metal electrode, AOLi and BTOLi composite electrodes before and after 10 cycles at  $0.1 \text{ mA cm}^{-2}$  for 5 h. SEM images of the pristine surface of (a, d, g, j) Li-metal, AOLi, BTOLi and BTOLi-BTOLPSC electrodes, respectively. SEM images of electrode side after cycling of (b, e, h, k) bare Li-metal, AOLi, BTOLi and BTOLi-BTOLPSC cells, respectively. SEM images of electrolyte side after cycling of (c, f, i, l) bare Li-metal, AOLi, BTOLi and BTOLi-BTOLPSC cells, respectively. Embedded figures are the relevant digital pictures.

### 3.3.5 Full cell cycling when paired with a $\text{Li}_4\text{Ti}_5\text{O}_{12}$ cathode

The effectiveness of the BTOLi anode is further evaluated by pairing with  $\text{Li}_4\text{Ti}_5\text{O}_{12}$  (LTO) as the cathode and performing galvanostatic cycling. LTO was selected because of its extremely small volumetric change upon (de)lithiation and working potential (1.55 V vs  $\text{Li}/\text{Li}^+$ ) which is within the electrochemical stability window of LPSC.<sup>21,22,42</sup> Thereby, the



degradation of the cell will be mainly due to the Li-metal anode, which will allow evaluating the impact of the dielectric constant of the solid additives. **Figure 3.6** shows the capacity upon galvanostatic cycling at a current density of  $0.31 \text{ mA cm}^{-2}$  for the four battery configurations when paired with the  $\text{Li}_4\text{Ti}_5\text{O}_{12}$  cathode. The mass loading for the LTO is approximately  $6.0 \text{ mg cm}^{-2}$  having a theoretical specific capacity of  $175 \text{ mA h g}^{-1}$ . Both the Li-metal and AOLI anodes, **Figures 3.6a** and **3.6b** show rapid capacity fading and average Coulombic efficiency of 135% and 120% respectively, signifying the large reactivity of the LPSC electrolyte that increases the discharge capacity.<sup>8,30,43</sup> Although the BTOLi/LPSC/LTO cell also shows rapid capacity fading upon cycling, it is less severe due to the better Coulombic efficiency (average 110%), demonstrating that BTO in the Li-metal anode improves the reversibility. Note that a comparison to the AO additive suggests this improvement is the consequence of the dielectric constant.

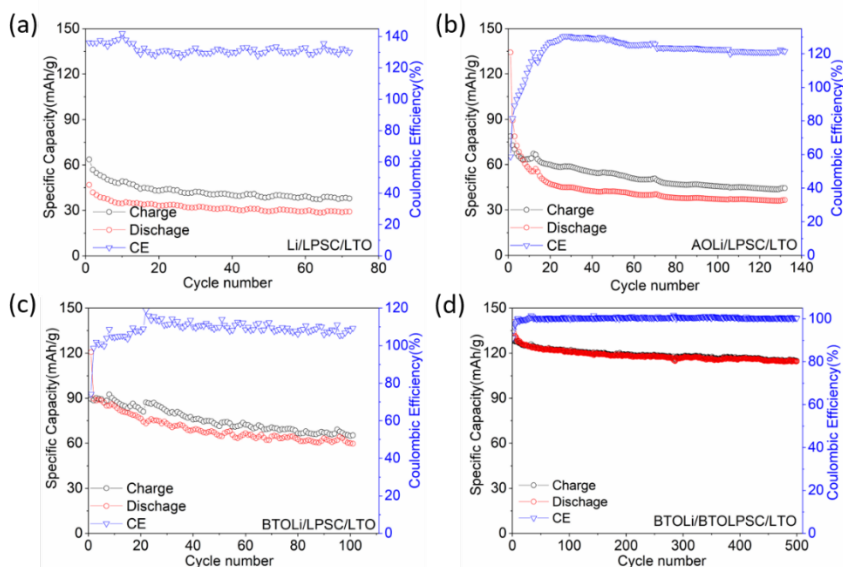


**Figure 3.6** Electrochemical cycling performance at  $0.31 \text{ mA cm}^{-2}$  the Li-metal, AOLI, BTOLi anodes with a  $\text{Li}_4\text{Ti}_5\text{O}_{12}$  cathode in combination with the LPSC and BTOLPSC solid electrolytes. Cycling performance of (a) the Li/LPSC/LTO cell, (b) the AOLI/LPSC/LTO cell, (c) the BTOLi/LPSC/LTO cell and (d) the BTOLi/BTOLPSC/LTO cell.

A spectacular improvement is observed upon adding BTO also to the LPSC solid electrolyte in the BTOLi/BTOLPSC/LTO cell, where the capacity is maintained for 90% over 500 cycles as observed in **Figure 3.6d**. Evaluation of the voltage curves during these cycling experiments, shown in **Figure S3.12**, demonstrates high overpotentials for the Li/LPSC/LTO, AOLI/LPSC/LTO and BTOLi/LPSC/LTO cells (**Table S3.4**). This reflects a high internal resistance due to the anode-solid electrolyte interface upon cycling, in line with the EIS

results in **Figure 3.4**, which can be ascribed to the formation of poorly conducting decomposition products and contact loss.<sup>8,17,33</sup> The BTOLi/BTOLPSC/LTO cell stands out by displaying much lower polarization during cycling, reflecting a much more stable anode-solid electrolyte interface, that is responsible for the relatively long cycle life.

### 3.3.6 Solid-state NMR

Solid-state  $^{31}\text{P}$  magic angle spinning (MAS) NMR measurements, very sensitive to the P chemical state, are performed to determine the decomposition of LPSC upon cycling. For pristine argyrodite, the  $^{31}\text{P}$  resonance occurs at 85 ppm as shown in **Figure 3.7a**, which can be assigned to the P environment in the  $\text{PS}_4$  tetrahedral units.<sup>21</sup> After cycling of the Li-LPSC-LTO cell, an increasing shoulder is observed at 95 ppm (**Figure 3.7c**), which can be assigned to the  $^{31}\text{P}$  environment of  $\text{Li}_3\text{PS}_4$  species. Moreover, as shown in zoomed **Figure 3.7b**, a clear  $\text{Li}_3\text{PO}_4$  peak was also identified. While both peaks of  $\text{Li}_3\text{PS}_4$  and  $\text{Li}_3\text{PO}_4$  in cycled BTOLi-BTOLPSC-LTO cell are not obvious. This indicates that the side decomposition in a Li-LPSC battery is more severe than in a BTO protected battery. In order to illustrate this process, **Figure 3.7d** summarizes the Li geometry change in differently structured batteries. In a Li-LPSC-LTO cell, because of the inhomogeneous electric field, Li tends to grow voids at the interface, which will induce local current concentration and also lithium-dendrite growth. In a cell with BTO added, the homogenous electric field would result in integral stripping of Li, and both matrix and interface are robustly maintained. This difference we believed is very important to solid-state Li metal, which could maintain a stable interface and protect the LPSC from side reactions with Li dendrites, further enhancing the performance of the Li-based anode.

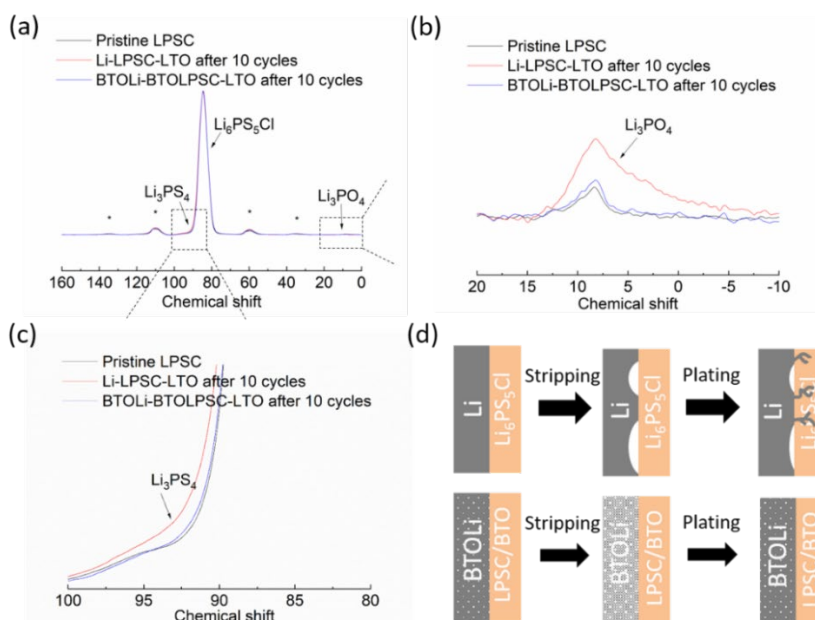


**Figure 3.7** (a-c)  $^{31}\text{P}$  MAS NMR of pristine LPSC and LPSC after cycling in Li-LPSC-LTO and BTOLi-BTOLPSC-LTO cells. (d) schematic figure showing the interface between Li-LPSC and BTOLi-BTOLPSC during Li plating and stripping.

### 3.4 Conclusion and outlook

To conclude, an integrally-formed BTO-based matrix has been successfully synthesized for solid-state Li metal batteries. The focused electric field in both electrolyte and electrode has been dramatically optimized by the BTO matrix, which intrinsically alleviates the growth of lithium filaments. Moreover, the lowered electronic conductivity in solid electrolyte also potentially suppresses the dendrites penetration. The ultra-stable cycling performances of solid-state Li metal symmetrical battery ( $1 \text{ mA cm}^{-2}$ ,  $2 \text{ mA h cm}^{-2}$ ) and BTOLi-BTOLPSC-LTO full battery (500 cycles, 90% capacity retention) have proved the successful suppression of electrolyte decomposition, as demonstrated by solid-state NMR, electrolyte decomposition is strongly reduced, resulting in less interface between Li metal and LPSC and also less decomposition. This work presents a novel way to solve the lithium dendrites growth and solid electrolyte decomposition, which may shed light on the future design of solid-state batteries.

### References

- 1 Goodenough, J. B. & Park, K.-S. The Li-ion rechargeable battery: a perspective. *J. Am. Chem. Soc.* **135**, 1167-1176 (2013).
- 2 Goodenough, J. B. & Kim, Y. Challenges for rechargeable Li batteries. *Chem. Mater.* **22**, 587-603 (2010).
- 3 Dunn, B., Kamath, H. & Tarascon, J.-M. Electrical energy storage for the grid: a battery of choices. *Science* **334**, 928-935 (2011).
- 4 Armand, M. & Tarascon, J.-M. Building better batteries. *Nature* **451**, 652-657 (2008).
- 5 Tarascon, J.-M. & Armand, M. Issues and challenges facing rechargeable lithium batteries. *Materials for sustainable energy: a collection of peer-reviewed research review articles from Nature Publishing Group*, 171-179 (2011).
- 6 Bruce, P. G., Freunberger, S. A., Hardwick, L. J. & Tarascon, J.-M. Li-O<sub>2</sub> and Li-S batteries with high energy storage. *Nat. Mater.* **11**, 19-29 (2012).
- 7 Janek, J. & Zeier, W. G. A solid future for battery development. *Nat. Energy* **1**, 16141 (2016).
- 8 Hatzell, K. B. *et al.* Challenges in lithium metal anodes for solid-state batteries. *ACS Energy Lett.* **5**, 922-934 (2020).
- 9 Famprikis, T., Canepa, P., Dawson, J. A., Islam, M. S. & Masquelier, C. Fundamentals of inorganic solid-state electrolytes for batteries. *Nat. Mater.* **18**, 1278-1291 (2019).
- 10 Xu, K. Electrolytes and interphases in Li-ion batteries and beyond. *Chem. Rev.* **114**, 11503-11618 (2014).
- 11 Manthiram, A., Yu, X. & Wang, S. Lithium battery chemistries enabled by solid-state electrolytes. *Nat. Rev. Mater.* **2** (2017).
- 12 Fu, K. *et al.* Three-dimensional bilayer garnet solid electrolyte based high energy density lithium metal-sulfur batteries. *Energy Environ. Sci.* **10**, 1568-1575 (2017).
- 13 Shen, F., Dixit, M. B., Xiao, X. & Hatzell, K. B. Effect of pore connectivity on Li dendrite propagation within LLZO electrolytes observed with synchrotron X-ray tomography. *ACS Energy Lett.* **3**, 1056-1061 (2018).

- 14 Tippens, J. *et al.* Visualizing chemomechanical degradation of a solid-state battery electrolyte. *ACS Energy Lett.* **4**, 1475-1483 (2019).
- 15 Nagao, M. *et al.* In situ SEM study of a lithium deposition and dissolution mechanism in a bulk-type solid-state cell with a Li<sub>2</sub>S-P<sub>2</sub>S<sub>5</sub> solid electrolyte. *Phys. Chem. Chem. Phys.* **15**, 18600-18606 (2013).
- 16 Porz, L. *et al.* Mechanism of lithium metal penetration through inorganic solid electrolytes. *Adv. Energy Mater.* **7** (2017).
- 17 Albertus, P., Babinec, S., Litzelman, S. & Newman, A. Status and challenges in enabling the lithium metal electrode for high-energy and low-cost rechargeable batteries. *Nat. Energy* **3**, 16-21 (2018).
- 18 Kamaya, N. *et al.* A lithium superionic conductor. *Nat. Mater.* **10**, 682-686 (2011).
- 19 Marbella, L. E. *et al.* <sup>7</sup>Li NMR chemical shift imaging to detect microstructural growth of lithium in all-solid-state batteries. *Chem. Mater.* **31**, 2762-2769 (2019).
- 20 Liu, M. *et al.* Controlling the lithium-metal growth to enable low-lithium-metal-excess all-solid-state lithium-metal batteries. *ACS Mater. Lett.* **2**, 665-670 (2020).
- 21 Schwietert, T. K. *et al.* Clarifying the relationship between redox activity and electrochemical stability in solid electrolytes. *Nat. Mater.* **19**, 428-435 (2020).
- 22 Zhu, Y., He, X. & Mo, Y. Origin of outstanding stability in the lithium solid electrolyte materials: insights from thermodynamic analyses based on first-principles calculations. *ACS Appl. Mater. Interfaces* **7**, 23685-23693 (2015).
- 23 Fan, X. *et al.* Fluorinated solid electrolyte interphase enables highly reversible solid-state Li metal battery. *Sci. Adv.* **4**, eaau9245 (2018).
- 24 Han, X. *et al.* Negating interfacial impedance in garnet-based solid-state Li metal batteries. *Nat. Mater.* **16**, 572-579 (2017).
- 25 Yang, C. *et al.* An electron/ion dual-conductive alloy framework for high-rate and high-capacity solid-state lithium-metal batteries. *Adv. Mater.* **31**, 1804815 (2019).
- 26 Zhang, X. *et al.* Long cycling life solid-state Li metal batteries with stress self-adapted Li/garnet interface. *Nano Lett.* **20**, 2871-2878 (2020).

- 27 Cheng, X.-B., Zhao, C.-Z., Yao, Y.-X., Liu, H. & Zhang, Q. Recent advances in energy chemistry between solid-state electrolyte and safe lithium-metal anodes. *Chem* **5**, 74-96 (2019).
- 28 Han, F., Yue, J., Zhu, X. & Wang, C. Suppressing Li dendrite formation in  $\text{Li}_2\text{S-P}_2\text{S}_5$  solid electrolyte by LiI incorporation. *Adv. Energy Mater.* **8**, 1703644 (2018).
- 29 Huo, H. *et al.* Rational design of hierarchical “Ceramic-in-Polymer” and “Polymer-in-Ceramic” electrolytes for dendrite-free solid-state batteries. *Adv. Energy Mater.* **9**, 1804004 (2019).
- 30 Schlenker, R. *et al.* Understanding the lifetime of battery cells based on solid-state  $\text{Li}_6\text{PS}_5\text{Cl}$  electrolyte paired with lithium metal electrode. *ACS Appl. Mater. Interfaces* **12**, 20012-20025 (2020).
- 31 Yan, H. *et al.* In situ generated  $\text{Li}_2\text{S-C}$  nanocomposite for high-capacity and long-life all-solid-state lithium sulfur batteries with ultrahigh areal mass loading. *Nano Lett.* **19**, 3280-3287 (2019).
- 32 Wang, M., Wolfenstine, J. B. & Sakamoto, J. Temperature dependent flux balance of the  $\text{Li/Li}_7\text{La}_3\text{Zr}_2\text{O}_{12}$  interface. *Electrochim. Acta* **296**, 842-847 (2019).
- 33 Zhang, X., Wang, A., Liu, X. & Luo, J. Dendrites in lithium metal anodes: suppression, regulation, and elimination. *Acc. Chem. Res.* **52**, 3223-3232 (2019).
- 34 Fan, L. *et al.* Enabling stable lithium metal anode via 3D inorganic skeleton with super lithiophilic interphase. *Adv. Energy Mater.* **8**, 1802350 (2018).
- 35 Orsini, F. *et al.* In situ SEM study of the interfaces in plastic lithium cells. *J. Power Sources* **81**, 918-921 (1999).
- 36 Orsini, F. *et al.* In situ scanning electron microscopy (SEM) observation of interfaces within plastic lithium batteries. *J. Power Sources* **76**, 19-29 (1998).
- 37 Liu, H. *et al.* Controlling dendrite growth in solid-state electrolytes. *ACS Energy Lett.* **5**, 833-843 (2020).
- 38 Han, F. *et al.* High electronic conductivity as the origin of lithium dendrite formation within solid electrolytes. *Nat. Energy* **4**, 187-196 (2019).
- 39 Yu, C. *et al.* Tuning ionic conductivity and electrode compatibility of  $\text{Li}_3\text{YBr}_6$  for high-performance all-solid-state Li batteries. *Nano Energy* **77**, 105097 (2020).

- 40 Cheng, X.-B., Zhang, R., Zhao, C.-Z. & Zhang, Q. Toward safe lithium metal anode in rechargeable batteries: a review. *Chem. Rev.* **117**, 10403-10473 (2017).
- 41 Liu, G. *et al.* Densified  $\text{Li}_6\text{PS}_5\text{Cl}$  nanorods with high ionic conductivity and improved critical current density for all-solid-state lithium batteries. *Nano Lett.* **20**, 6660-6665 (2020).
- 42 Richards, W. D., Miara, L. J., Wang, Y., Kim, J. C. & Ceder, G. Interface stability in solid-state batteries. *Chem. Mater.* **28**, 266-273 (2016).
- 43 Lewis, J. A., Tippens, J., Cortes, F. J. Q. & McDowell, M. T. Chemo-mechanical challenges in solid-state batteries. *Trends Chem.* **1**, 845-857 (2019).

## Supporting Information for Chapter 3

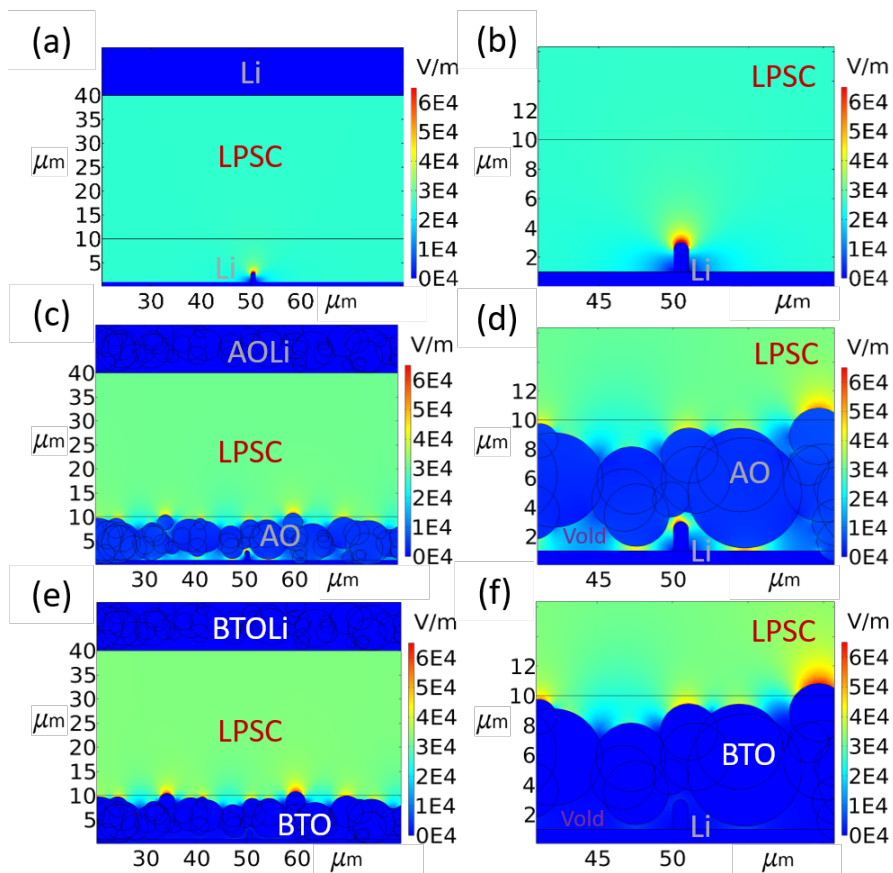


**Figure S3.1** Schematic diagram of electric field distribution in symmetric lithium metal cells with different dielectric materials for the stripped electrodes. (a, b) Li/Li<sub>6</sub>PS<sub>5</sub>Cl(LPSC)/Li cell, (c, d) Li-Al<sub>2</sub>O<sub>3</sub>(AOLi)/LPSC/AOLi cell, (e, f) Li-BaTiO<sub>3</sub>(BTOLi)/LPSC/BTOLi cell.



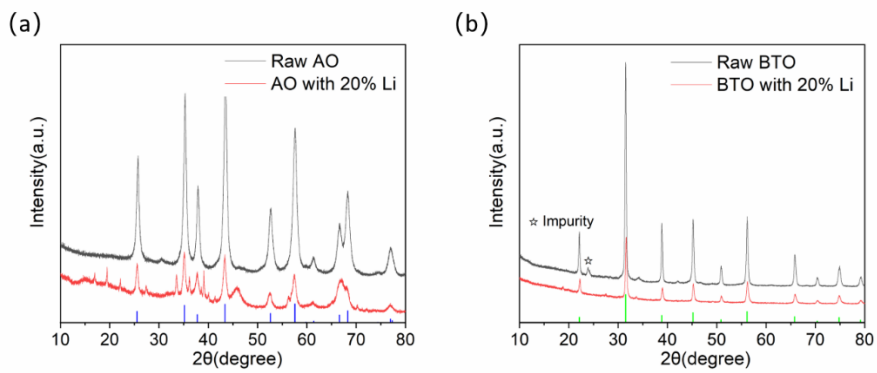


Figure S3.2 XRD patterns of (a)raw AO and AOLI, (b)raw BTO and BTOLi.

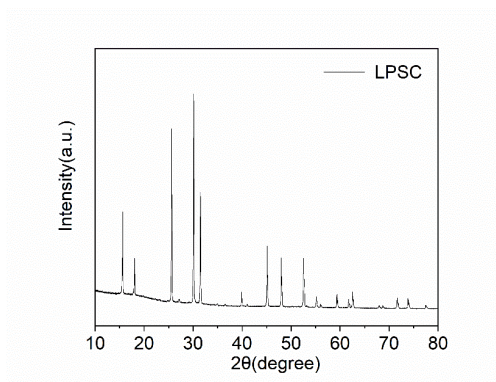
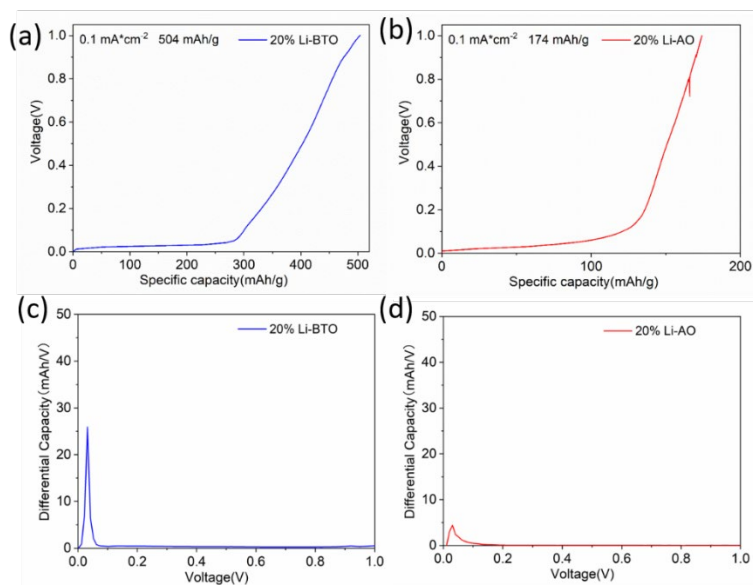


Figure S3.3 XRD pattern of LPSC.



**Figure S3.4** Practical specific capacity of (a) 20%Li-BTO electrode and (b) 20%Li-AO electrode after stripping Li to 1 V versus Li<sup>+</sup>/Li. Relevant differential capacity(c, d) of two electrodes.

**Table S3.1** Average overpotential of solid-state cells using bare Li electrodes, BTOLi or AOLi composite electrodes and LPSC or BTOLPSC electrolytes at varying current densities from 0.1 to 1.0 mA cm<sup>-2</sup> with a (dis)charge time of 1h.

	0.1 mA cm <sup>-2</sup>	0.3 mA cm <sup>-2</sup>	0.5 mA cm <sup>-2</sup>	1 mA cm <sup>-2</sup>
Li-LPSC	22 mV	-	-	-
AOLi-LPSC	26 mV	-	-	-
BTOLi-LPSC	17 mV	42 mV	60 mV	-
BTOLi-BTOLPSC	13 mV	19 mV	33 mV	65 mV

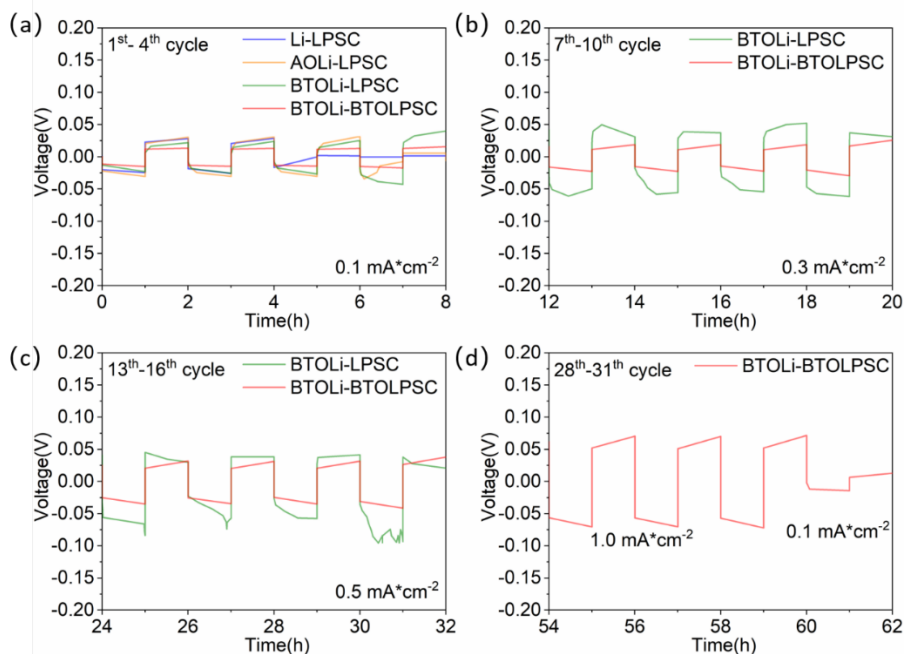


**Figure S3.5** Detailed voltage profiles of rate performance using bare Li electrode, BTOLI or AOLI composite electrodes and LPSC or BTOLPSC electrolytes at different cycles.

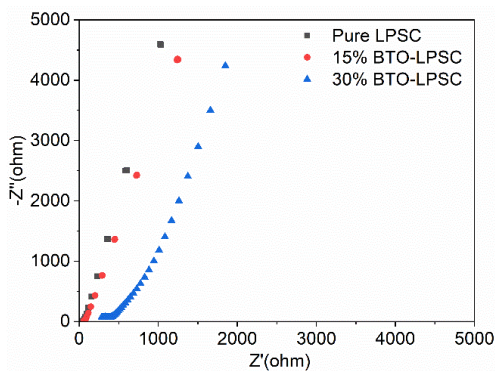


**Figure S3.6** The electrochemical impedance spectroscopy (EIS) results of LPSC solid electrolyte and BTOLPSC mixture.

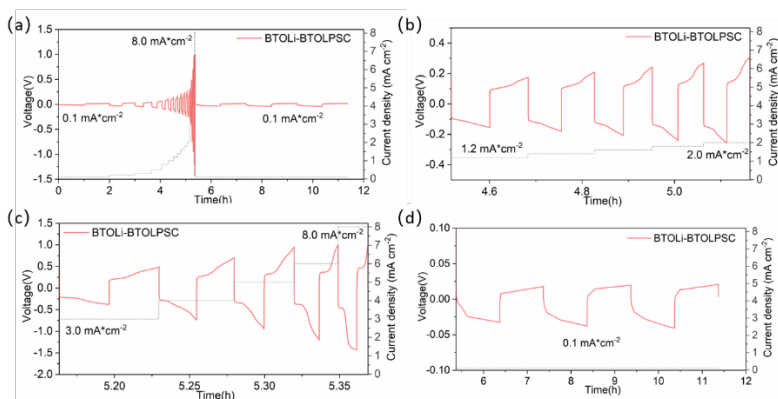


**Figure S3.7** Voltage profiles of the solid-state symmetric cell using a BTOLi composite electrode and BTOLPSC electrolyte cycled under a current density of  $0.1 \text{ mA cm}^{-2}$  to  $8.0 \text{ mA cm}^{-2}$  with a fixed capacity of  $0.1 \text{ mA h cm}^{-2}$ .

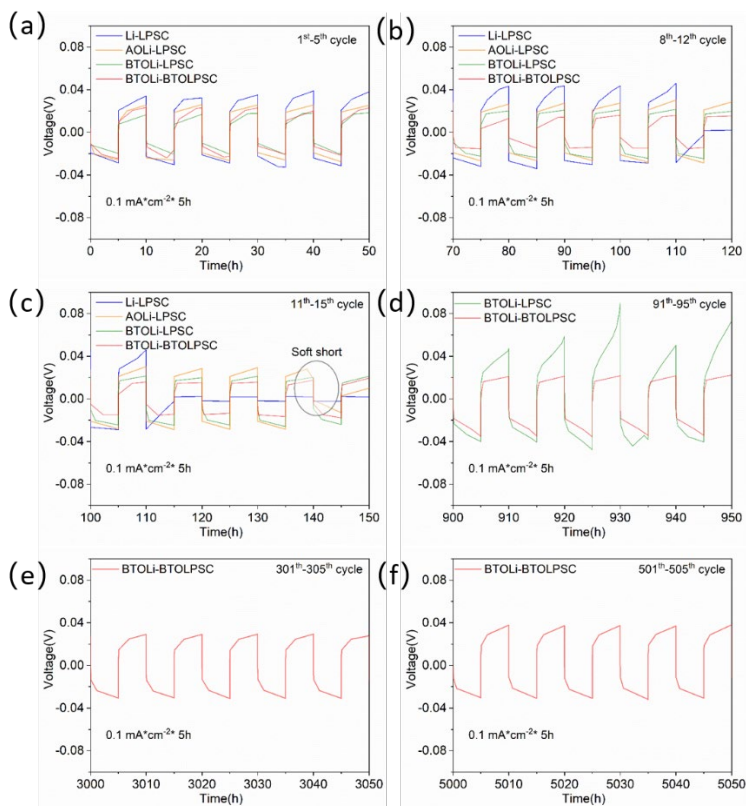


**Figure S3.8** Detailed voltage profiles of cycling performance under a current density of  $0.1 \text{ mA}$  for  $5 \text{ h}$  using a bare Li electrode, AOLI and BTOLi composite electrodes and LPSC or BTOLPSC electrolytes at different cycles.

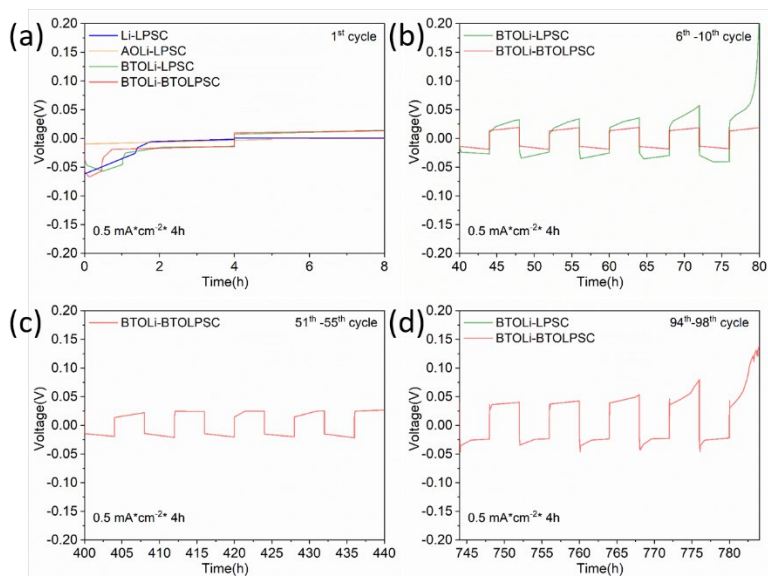


**Figure S3.9** Detailed voltage profiles of cycling performance under a current density of 0.5 mA for 4 h using a bare Li electrode, AOLI and BTOLI composite electrodes and LPSC or BTOLPSC electrolytes at different cycles.

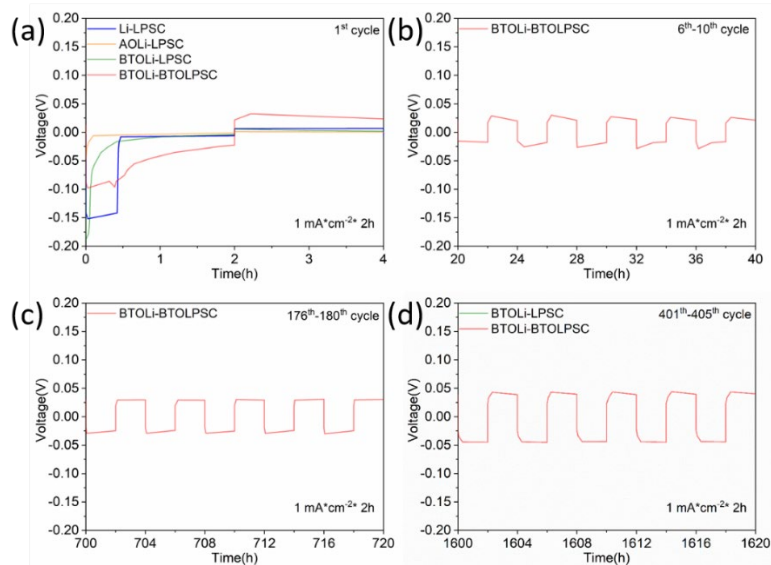


**Figure S3.10** Detailed voltage profiles of cycling performance under a current density of 1.0 mA for 2 h using a bare Li electrode, AOLI and BTOLI composite electrodes and LPSC or BTOLPSC electrolytes at different cycles.

**Table S3.2** Comparison of recently reported plating/stripping performances of all-solid-state Li–Li symmetric cells for current density, areal capacity, and cycling life. (BTO: BaTiO<sub>3</sub>, LPSC: Li<sub>6</sub>PS<sub>5</sub>Cl, CP: carbon paper, PEGDME: poly(ethylene glycol) dimethyl ether, PEO: Polyethylene oxide, LATP: Li<sub>1.3</sub>Al<sub>0.3</sub>Ti<sub>1.7</sub>(PO<sub>4</sub>)<sub>3</sub>, LLZO: Li<sub>6.75</sub>La<sub>3</sub>Zr<sub>1.75</sub>Ta<sub>0.25</sub>O<sub>12</sub>, ALD: Atomic layer deposition, LPS: Li<sub>2</sub>S-P<sub>2</sub>S<sub>5</sub>, HCSE: hierarchical composite solid electrolyte with the interface-regulated garnet layer and “polymer-in-separator” composite polymer electrolyte matrix)

Electrode	Electrolyte	Current density (mA/cm <sup>2</sup> )	Areal capacity (mAh/cm <sup>2</sup> )	Cycling life (h)	Method
<b>BTOLi composite (this work)</b>	BTO/LPSC mixture	1	2	1700	Mixing lithium metal and BTO at 300 °C
<b>Lithium metal<sup>1</sup></b>	Densified LPSC	0.5	0.5	3000	Pellet sintered LPSC
<b>Li/CP@MoS<sub>2</sub><sup>2</sup></b>	PEGDME	1	1	1000	Hydrothermal method
<b>Lithium metal<sup>3</sup></b>	PEO-50%LATP	0.2	0.05	200	Sol-gel method
<b>Lithium metal<sup>4</sup></b>	PEO-LLZO	0.5	0.25	1000	electrospinning
<b>Lithium metal<sup>5</sup></b>	Densified LPSC	1	1	100	Pressed with 500 MPa and then sintered
<b>Lithium metal<sup>6</sup></b>	ALD-garnet	0.2	0.1	90	ALD-treated-garnet
<b>Lithium metal<sup>7</sup></b>	70LPS30LiI	1.5(100°C)	1.5	200	Solid-state method
<b>Lithium metal<sup>8</sup></b>	LLZTO@ZnO	0.5	0.25	600	Acid-etching LLZTO
<b>Lithium metal<sup>9</sup></b>	HCSE	0.5	0.25	4800	Mixing and curing
<b>Lithium metal<sup>10</sup></b>	LiAlCl <sub>4</sub>	0.1	-	160	Solid-state method

**Table S3.3** Resistance of symmetric cells assembled with a bare Li anode, AOLI and BTOLI composite anodes using LPSC electrolyte and a BTOLI composite anode using BTOLPSC composite electrolyte at different cycles.

	Fresh ( $\Omega$ )	1 <sup>st</sup> ( $\Omega$ )	10 <sup>th</sup> ( $\Omega$ )	50 <sup>th</sup> ( $\Omega$ )	100 <sup>th</sup> ( $\Omega$ )
Li-LPSC	159	190	195	-	-
AOLi-LPSC	132	182	196	-	-
BTOLI-LPSC	122	145	147	149	161
BTOLI-BTOLPSC	116	95	93	97	99

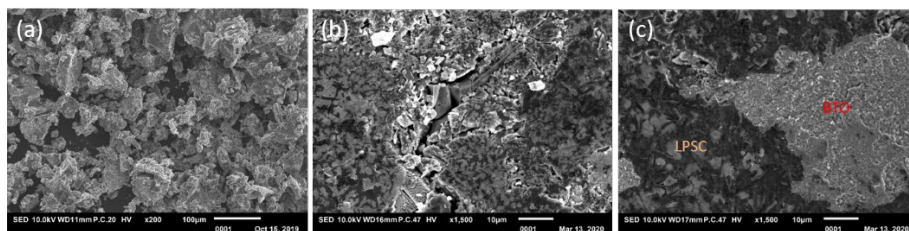


**Figure S3.11** SEM images of (a) LPSC electrolyte, (b) pressed LPSC wafer and (c) pressed BTOLPSC wafer.

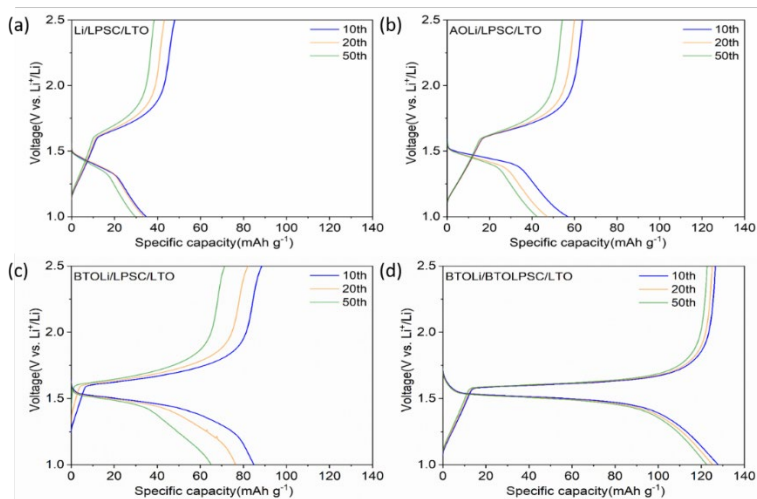


**Figure S3.12** Voltage profiles of (a) Li/LPSC/LTO cell, (b) AOLI/LPSC/LTO cell, (c) BTOLi/LPSC/LTO cell and (d) BTOLi/BTOLPSC/LTO cell at different cycles.

**Table S4** Overpotential of cells in **Figure S12**

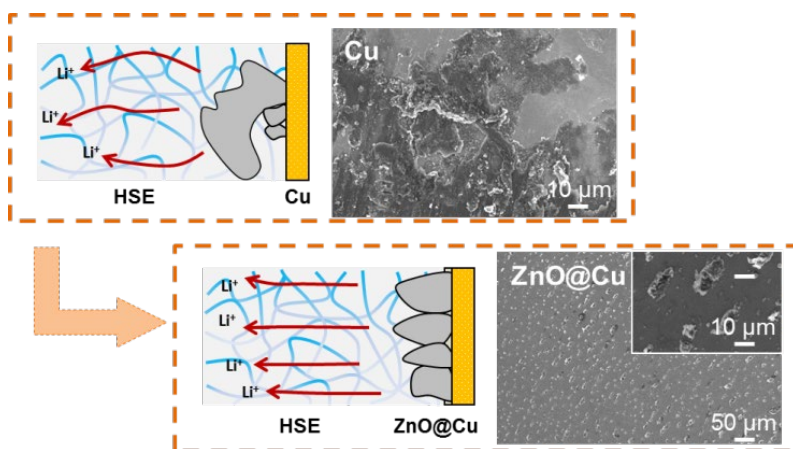
Type of cells	10 <sup>th</sup> cycle	20 <sup>th</sup> cycle	50 <sup>th</sup> cycle
Li/LPSC/LTO	0.283 V	0.289 V	0.335 V
AOLI/LPSC/LTO	0.243 V	0.290 V	0.370 V
BTOLi/LPSC/LTO	0.206 V	0.235 V	0.314 V
BTOLi/BTOLPSC/LTO	0.111 V	0.122 V	0.132 V



### References

- S3.1 Liu, G. *et al.* Densified  $\text{Li}_6\text{PS}_5\text{Cl}$  nanorods with high ionic conductivity and improved critical current density for all-solid-state lithium batteries. *Nano Lett.* **20**, 6660-6665 (2020).
- S3.2 Yang, X. *et al.* Phase evolution of a prenucleator for fast Li nucleation in all-solid-state lithium batteries. *Adv. Energy Mater.* (2020).
- S3.3 Ban, X., Zhang, W., Chen, N. & Sun, C. A high-performance and durable Poly(ethylene oxide)-based composite solid electrolyte for all solid-state lithium battery. *J. Phys. Chem. C* **122**, 9852-9858 (2018).
- S3.4 Fu, K. K. *et al.* Flexible, solid-state, ion-conducting membrane with 3D garnet nanofiber networks for lithium batteries. *Proc. Natl. Acad. Sci.* **113**, 7094-7099 (2016).
- S3.5 Kasemchainan, J. *et al.* Critical stripping current leads to dendrite formation on plating in lithium anode solid electrolyte cells. *Nat. Mater.* **18**, 1105-1111 (2019).
- S3.6 Han, X. *et al.* Negating interfacial impedance in garnet-based solid-state Li metal batteries. *Nat. Mater.* **16**, 572-579 (2017).
- S3.7 Han, F., Yue, J., Zhu, X. & Wang, C. Suppressing Li dendrite formation in  $\text{Li}_2\text{S-P}_2\text{S}_5$  solid electrolyte by LiI incorporation. *Adv. Energy Mater.* **8**, 1703644 (2018).
- S3.8 Huo, H. *et al.* Dynamics of the garnet/Li interface for dendrite-free solid-state batteries. *ACS Energy Lett.* **5**, 2156-2164 (2020).
- S3.9 Sun, J. *et al.* Hierarchical composite-solid-electrolyte with high electrochemical stability and interfacial regulation for boosting ultra-stable lithium batteries. *Adv. Funct. Mater.* (2020).
- S3.10 Tanibata, N. *et al.* Metastable chloride solid electrolyte with high formability for rechargeable all-solid-state lithium metal batteries. *ACS Mater. Lett.* **2**, 880-886 (2020).

## Chapter 4 Controlling the Lithium-Metal Growth To Enable Low-Lithium-Metal-Excess All-Solid-State Lithium-Metal Batteries



**This chapter is based on:**

**Chao Wang**, Ming Liu, Zhu Cheng, Swapna Ganapathy, Lucas A. Haverkate, Sandeep Unnikrishnan and Marnix Wagemaker, Controlling the Lithium-Metal Growth To Enable Low-Lithium-Metal-Excess All-Solid-State Lithium-Metal Batteries, *ACS Materials Letters*, **2020**, 2, 665-670.

### Abstract

Solid-state lithium (Li) metal batteries are considered as a promising candidate for next-generation high energy density storage devices to power electric vehicles. Critical challenges for solid-state Li-metal batteries include the large morphological changes associated with plating and stripping of Li-metal and the decomposition of the solid electrolyte due to the reductive nature of Li-metal, both increasing the Li-metal-solid electrolyte interface resistance. This is especially challenging when starting in the discharged state with a bare anode or “anode-less” current collector facing the solid electrolyte. To overcome this a 100 nm thin layer of ZnO is deposited on the copper current collector with atomic layer deposition (ALD). During the first charge, this results in more homogeneous Li-metal growth, rationalized by the formation of a Zn-Li alloy that acts as seed crystals for the Li-metal. The resulting more homogeneous Li-metal growth maintains better contact with the solid electrolyte, leading to more reversible cycling of Li metal. Minor prelithiating of the ZnO/Cu anode with 1 mA h cm<sup>-2</sup> further improves the cycling performance, as demonstrated in a full all-solid-state cell using LiFePO<sub>4</sub> as a cathode, resulting in an average Coulombic efficiency over 95%. These findings mark the first steps in an interface strategy to overcome the challenges at the solid electrolyte – Li-metal interface in solid-state Li-metal batteries.

### 4.1 Introduction

Proposed by Whittingham in 1976<sup>1</sup>, the lithium metal battery (LMB) makes use of the high specific capacity ( $3860 \text{ mA h g}^{-1}$ ) and low reduction potential ( $-3.040 \text{ V vs SHE}$ ) of Li-metal, motivating the current intensive research towards this 'Holy Grail' anode for Li-batteries<sup>2,3</sup>. Unfortunately, the severe reactivity of Li-metal with liquid electrolytes, leading to uncontrolled solid electrolyte interface (SEI) growth, as well as the formation of dendritic Li-metal morphologies result in a short cycle life and safety concerns that have hindered the capitalization of Li-metal based batteries (LMBs)<sup>3-7</sup>. Specifically, when during plating the current exceeds the supply of Li-ions, determined by the conductivity of the electrolyte, ion depletion at the Li metal surface occurs after the characteristic Sand's time<sup>3,7</sup>. Under these conditions plating becomes inhomogeneous and self-amplified growth of dendrites is induced. Even at lower current densities, dendritic growth is induced, presumably because of the inhomogeneous nature of the SEI<sup>3,8</sup>. As a consequence, the use of volatile and flammable liquid organic electrolytes in Li-metal batteries leads to significant safety concerns<sup>9-11</sup>.

In this context, replacing the liquid electrolyte with a solid electrolyte (SE) is considered to be a promising strategy. In addition to the challenges related to the electrochemical stability of the solid electrolytes, this also introduces a different challenge as compared to liquid electrolytes: How to maintain contact between the SE and the Li-metal anode to guaranty Li-ion transport, especially because the Li-metal undergoes large volumetric and morphological changes upon (dis)charging<sup>12-14</sup>. The interface should thus provide high ionic conductivity, resist the reducing potential of Li-metal environment and prevent delamination upon the inherent Li-metal volumetric change upon cycling<sup>15,16</sup>. From the many solid electrolytes developed<sup>3,17,18</sup> so far only polyethylene oxide (PEO) based polymer electrolytes, developed by Delmas, have allowed the development of commercial solid state Li-metal batteries<sup>19</sup>. The disadvantage is however the relatively low conductivity of polymer-based electrolytes, which demands battery operation above  $60 \text{ }^\circ\text{C}$ . Aiming at more challenging room temperature Li-metal batteries, countless strategies have been developed to improve the ionic conductivity, interfacial properties and the safety issues related to Li metal in polymer-based batteries<sup>12-14,20-23</sup>. This has resulted in lab-scale Li-metal batteries operating at room temperature, however, typically starting with thick lithium-metal sheets at the anode<sup>12-14,20-23</sup>. In practice, a large excess of lithium at the copper current collector, lowers the energy density of the LMB and makes battery assembly more costly and challenging<sup>24,25</sup>. Ideally, all active Li is initially stored in the cathode to maximize energy density. However, starting with a bare copper current collector in contact with the solid electrolyte makes it extremely challenging to maintain this contact, to support Li-ion

transport during cycling<sup>3</sup>, upon the Li-metal growth and shrinking. To the best of our knowledge, only *Yang et al.*<sup>12</sup> have demonstrated cycling of a Cu-solid electrolyte interface in a solid-state Li-Cu battery, which was achieved by e-beam deposition of Cu at the bottom of the garnet skeleton, where the Li-metal plating occurs in the porous garnet matrix. However, it was stressed that completely stripping Li-metal from the copper current collector should be avoided, because this could extract Li from the LLZO electrolyte itself and lead to the LLZO structure to collapse.<sup>12</sup> This demonstrates the challenges to achieve reversible cycling of Li-metal solid-state batteries starting with a lithium metal-free anode, especially aiming for easy to produce, future high energy density LMBs.

Here we demonstrate the formation of large lithium deposits on the bare copper current collector in a solid-state LMB, utilizing a PEO-based hybrid solid electrolyte (HSE) previously reported<sup>14</sup>, upon cycling at room temperature. The large deposits result in contact loss, raise the impedance and cause these cells to fail within a few cycles. In order to improve the compatibility between the HSE and the copper current collector, a thin layer of ZnO was coated on copper by atomic layer deposition (ALD). Upon plating this forms a LiZn alloy, making the surface lithium-philic, resulting in more evenly distributed lithium metal deposits, rationalized by the larger number of Li-metal nucleation sites. The improved cycling of the Li-metal plating and stripping was evaluated by *operando* neutron depth profiling (NDP), monitoring the Li-density as a function of depth on the copper current collector. A much higher lithium efficiency and better lithium geometry are observed. Finally, a full cell composed of 3 mg cm<sup>-2</sup> LiFePO<sub>4</sub> cathode and 1 mA h cm<sup>-2</sup> prelithiated ZnO@Cu anode was successfully combined with high Coulombic efficiency, illustrating the potential of this interface strategy for the development of solid-state Li-metal batteries.

## 4.2 Results and discussions

### 4.2.1 Characterization of electrochemical performance and Li deposition morphology

In order to explore the Li deposition morphology on a bare copper current collector, a solid-state Cu/HSE/Li-metal battery is assembled. The HSE is composed of PEO, lithium bis(trifluoromethanesulfonyl)imide (LiTFSI), succinonitrile (SN) and Li<sub>1.5</sub>Al<sub>0.5</sub>Ge<sub>1.5</sub>(PO<sub>4</sub>)<sub>3</sub> (LAGP) as prepared previously<sup>14</sup>, in which Li-ion transport was enhanced through concurrent transport in both the organic and inorganic phases. The resulting conductivity, 1.73 × 10<sup>-4</sup> S cm<sup>-1</sup>, enables room-temperature battery cycling<sup>14</sup>. The electrochemical performance of the Cu/HSE/Li battery cycled at 0.05 mA cm<sup>-2</sup> for 4 h is shown in **Figure 4.1a**. The poor electrochemical performance of the Cu/HSE/Li battery, as expressed by the large over-potential (about 500 mV) and poor Coulombic efficiency (about 40%), illustrates the

difficulty to plate Li metal on the bare copper surface facing the HSE. The large polarization, in the end, indicates that delamination of the electrode/electrolyte interface, and hence contact loss between the plated Cu current collector and the HSE, is responsible for the very short cycle life. **Figures 4.1b-d** present SEM images showing the surface morphology of the fresh and cycled copper electrodes after plating 0.2 and 1 mA h cm<sup>-2</sup> at a current density of 0.05 mA cm<sup>-2</sup>. After plating 0.2 mA h cm<sup>-2</sup>, the smooth surface of copper is covered by a rough Li-metal morphology (**Figure 4.1c**). The large and irregular shaped lithium particles, having a diameter around about 10 μm, reflect a small density of nucleation centers, presumably initiated by the poor contact. After deposition of 1 mA h cm<sup>-2</sup>, the copper surface is covered by large lithium flakes with a diameter larger than 50 μm. The lithium morphology in a solid-state Li-Cu battery is very different from that in liquid electrolyte-based batteries where mossy/dendritic lithium form<sup>26</sup>. The large deposited Li-flakes in the solid-state battery appear to result in contact loss between the electrode and the HSE, also evidenced by easy removal of the current collector after disassembling, suggesting that more homogeneous plating on the copper surface is demanded.

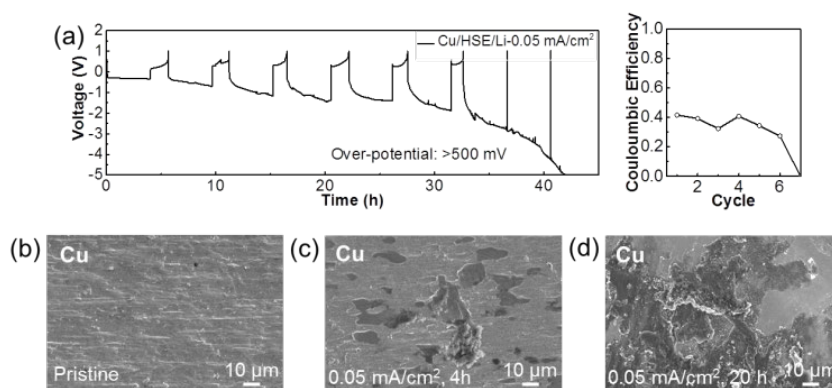


**Figure 4.1** Plating lithium metal at the Cu-HSE interface. (a) Electrochemical performance of Cu/HSE/Li batteries at 0.05 mA cm<sup>-2</sup> for 4 h. (b, c, d) SEM measurements showing the fresh Cu, 0.2 and 1 mA h cm<sup>-2</sup> Li plated metal morphology in a Cu/HSE/Li battery.

Bare Cu is not lithium-phobic, and as a consequence, large deposited Li-flakes tend to be formed because of the insufficient active Li metal grown sites. ZnO is known to improve the wettability of garnet solid-state electrolytes to molten lithium because of a conversion reaction upon lithiation in the voltage range 0-1 V vs Li/Li<sup>+</sup><sup>27, 28</sup>. Here we aim to use the resulting lithium-phillic Zn-Li alloy particles acting as nucleation seeds for Li-metal growth upon subsequent plating at 0 V vs Li/Li<sup>+</sup> on bare Cu, thus to achieve more homogeneous and thin Li-metal growth, and thereby prevent delamination. Using ALD, a 100 nm thin film of

ZnO is deposited on the surface of the copper current collector, as shown in **Figure 4.2a**, which is referred to as ZnO@Cu.

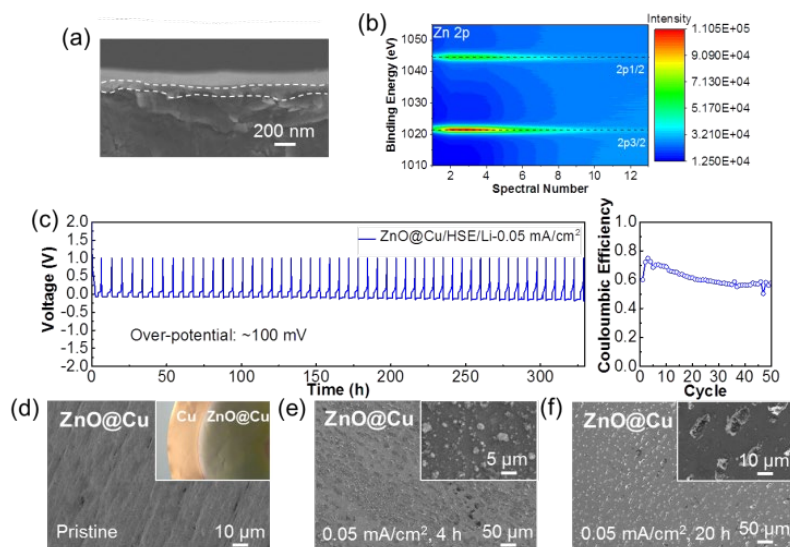


**Figure 4.2** Plating lithium metal at the ZnO@Cu-HSE interface. (a) Cross-section SEM measurements showing the morphology of the ALD deposited ZnO on a Cu current collector (ZnO@Cu). (b) Zn 2p XPS depth profile of the pristine ZnO@Cu current collector. (c) Electrochemical performance of the ZnO@Cu/HSE/Li battery at  $0.05 \text{ mA cm}^{-2}$  for 4 h. (d, e, f) SEM images of the pristine ZnO@Cu current collector, the Li metal morphology after plating at  $0.05 \text{ mA cm}^{-2}$  up to a capacity of 0.2 and  $1 \text{ mA h cm}^{-2}$ , respectively.

To verify the thickness of ZnO, XPS depth profiling was carried out as shown in **Figure 4.2b**, where Zn 2p XPS signal is present until a depth of approximately 100 nm (each spectrum was taken by depth-profiling every 10 nm). The voltage responds upon cycling at  $0.05 \text{ mA cm}^{-2}$  for 4 hours is shown in **Figure 4.1c**. Comparing the cycling of the bare Cu current collector (Cu/HSE/Li battery), **Figure 4.1a**, with the cycling of the ZnO@Cu current collector (ZnO@Cu/HSE/Li battery) shows that the presence of the thin ZnO film results in a Li-Zn alloy formation platform at  $0.5 \text{ V}$ <sup>29, 30</sup> (**Figure S4.1**) and a significant decrease of the over-potential (about 80 mV). In addition, the introduction of the ZnO thin film increases the Coulombic efficiency significantly to 65% and the reversibility. Increasing the current density to  $0.1 \text{ mA cm}^{-2}$  for 10 h during 10 cycles also results in a relatively good performance with a Coulombic efficiency of about 75% (**Figure S4.2**). The morphology of the fresh ZnO@Cu and after Li metal deposition are presented in **Figure 4.2d-f**. As shown in the SEM image of the ALD deposited ZnO film, **Figure 4.2d**, it covers the wrinkled copper surface. As compared to the Li-deposits on bare Cu, **Figure 4.1c-d**, the Li-metal deposits on the ZnO@Cu current

collector are isolated and much smaller, with a diameter of about 3  $\mu\text{m}$ , after plating at 0.05  $\text{mA cm}^{-2}$  up to 0.2  $\text{mA h cm}^{-2}$  as shown in **Figure 4.2e**. The homogeneously distributed and isolated nature of the plated Li-metal particles on the current collector are suggested to form because the Li-Zn alloy acts as a seed crystal for Li-metal nucleation. After plating up to 1  $\text{mA h cm}^{-2}$ , the lithium metal particles grow to an average size of about 10  $\mu\text{m}$ , much smaller and more regular shaped compared to the large Li flakes when plating on the bare copper current collector in the Cu/HSE/Li battery. We conclude that the ZnO layer on the copper current collector, through the formation of well-distributed Zn-Li alloy particles, initiates well distributed and relatively monodisperse growth of lithium metal. This appears very beneficial for the Li-metal plating/stripping reversibility, most likely because it enables to dissipate localized stress and maintains much better contact with the HSE, as indicated by the lower overpotentials.<sup>31</sup> The impedance evolution for Cu/HSE/Li and ZnO@Cu/HSE/Li batteries before and after 5 cycles are shown in **Figure S4.3**. This demonstrates that the interfacial impedance of ZnO@Cu/HSE/Li is significantly smaller than Cu/HSE/Li after 5 cycles, which is in agreement with a better contact between the current collector and the HSE. To gain more insight in the reversibility of the Li-metal plating/stripping behaviour of the ZnO@Cu/HSE interface under *operando* conditions, NDP is employed as a direct probe of the Li-metal distribution as a function of depth perpendicular to the current collector.

### 4.2.2 Neutron depth profiling

Neutron depth profiling (NDP) enables quantitative, non-destructive monitoring of the spatial distribution of lithium metal, perpendicular to the current collector, under realistic battery operation conditions.<sup>32, 33</sup> Thereby, it can provide valuable insights in the formation of the SEI and the evolution of the Li-concentration gradient associated with Li-metal plating/stripping, and how these processes depend on the electrochemical conditions. **Figure 4.3** shows the *operando* NDP results of the Li-metal plating in the solid-state Cu/HSE/Li and ZnO@Cu/HSE/Li batteries, yielding the normalized Li-metal density (measured Li-density normalized on the bulk Li-metal density) as a function of depth, over 5 cycles at a current density of 0.05  $\text{mA cm}^{-2}$ . The depth as shown in **Figures 4.3a, b** is measured starting from the interface between the Cu current collector and the HSE (located at about 12  $\mu\text{m}$  depth). For the bare copper current collector in the Cu/HSE/Li battery, the average Li density, as well as the thickness of the deposits, rapidly increase upon cycling, **Figure 4.3a**, reflecting the buildup of inactive Li-metal and Li-species at the HSE side over cycling. This is improved for the ZnO@Cu current collector, reflecting better affinity between the Li metal with the ZnO covered current collector, and in line with the improved electrochemical cycling shown in **Figure 4.2c**. Integrating the Li-density depth profiles in



**Figures 4.3a**, and **b** results in the evolution of the plated lithium mass during cycling as shown in **Figure 4.3c** for both the Cu/HSE/Li and ZnO@Cu/HSE/Li batteries. The total amount of inactive Li quantified by NDP is a combination of ‘dead’ Li metal, and inactive Li in the SEI, as the chemical nature of Li cannot be distinguished with NDP.<sup>32</sup> The ratio of the stripped capacity and the plated capacity represent the Li-efficiency, complementary to the Coulombic efficiency (electron efficiency). The presence of the ZnO film on the copper current collector raises the Li efficiency from about 45% to 80%, reflecting a more efficient plating/stripping process (**Figure 4.3d**).

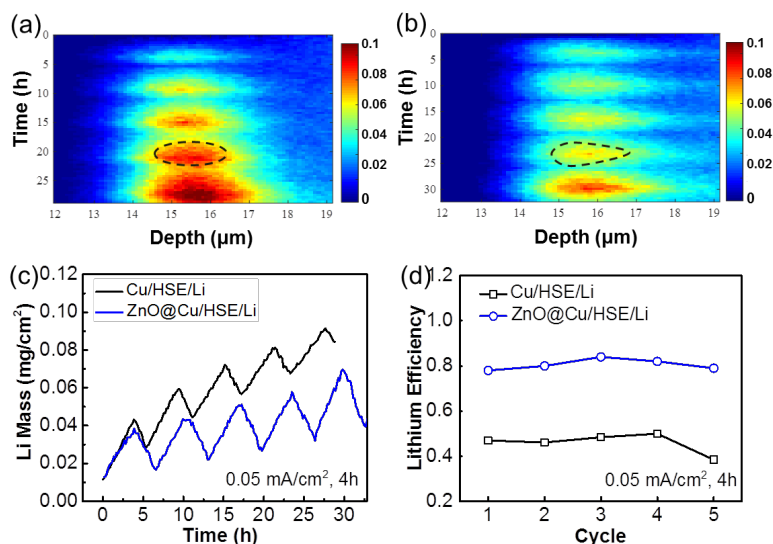


**Figure 4.3** Impact of the ALD ZnO layer on Li density distribution in solid-state lithium copper battery. (a, b) *Operando* NDP measurements for 5 cycles of the Cu/HSE/Li and ZnO@Cu/HSE/Li batteries at 0.05  $\text{mA}/\text{cm}^2$ . The colour intensity quantifies the measured lithium density normalized to bulk Li-metal. (c, d) Lithium density and lithium efficiency evolution of Cu/HSE/Li and ZnO@Cu/HSE/Li batteries. The depth is measured from the outside surface of the copper; hence the plating starts at approximately 12  $\mu\text{m}$ , representing the thickness of the copper current collector window. The colour scale of the NDP measurements indicates the fractional Li-density normalized to Li-metal.

From the *operando* NDP results, probing the average Li-density over approximately 1  $\text{cm}^2$  of the electrode, and the regular distributed and relatively monodisperse Li-metal particles observed by SEM, we propose the process shown in **Figure 4.4**. In the Cu/HSE/Li battery (**Figure 4.4a**), the absence of nucleation sites on the Li-phobic Cu results in large, non-uniform Li-metal flakes, as observed in **Figure 4.1c** and **d**. This can be expected to be a self-amplified process as it induces a non-uniform Li-ion flux through the limited contact points between Li-metal and HSE. Upon stripping this leads to effective delamination of the HSE,

explaining the large voltage polarization observed in **Figure 4.1a**. In contrast, the conversion of the thin ZnO film towards Zn-Li alloy particles results in small nucleation sites for subsequent Li-metal plating, as shown in **Figure 4.2e** and **f**, on the copper surface. The resulting homogeneous distribution of small Li-metal particles, will lead to more contact points with the HSE and thus a more homogeneous Li-ion flux distribution (**Figure 4.4b**). This suppresses delamination and rationalizes the improved reversibility of the plating/stripping process as observed with *operando* NDP.

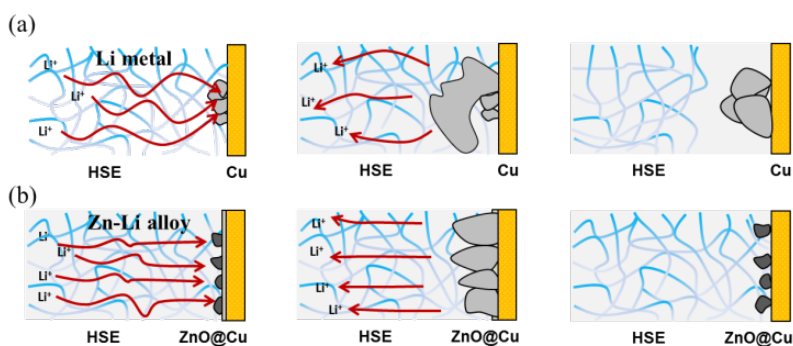


**Figure 4.4** Schematic illustration for the Li metal plating/stripping process on (a) bare Cu current collector and (b) ZnO@Cu current collector.

#### 4.2.3 Full cell performance of prelithiated ZnO@Cu anode and LiFePO<sub>4</sub> cathode

Aiming at further improving the interface of the ZnO@Cu current collector with the HSE, the impact of prelithiation is investigated. After prelithiated to  $1 \text{ mA h cm}^{-2}$  Li, the ZnO@Cu/HSE/Li battery demonstrates stable cycling at  $0.5 \text{ mA h cm}^{-2}$  with nearly 100 % Coulombic efficiency over 40 cycles. (**Figure 4.5a** and **b**) Clearly, this compromises the energy density as well as the full cell assembly conditions. The prelithiation may be optimized to yield much lower Li prelithiation capacities, which is subject of further research. Here we employ this approach to demonstrate cycling of the  $1 \text{ mA h cm}^{-2}$  prelithiated ZnO@Cu in combination with a  $3 \text{ mg cm}^{-2}$  LiFePO<sub>4</sub> cathode. This full solid-state Li-metal battery geometry delivers relatively stable cycling, at an average Coulombic efficiency of approximately 95 % as shown in **Figure 4.5c** and **d**. After 45 cycles, a capacity of about  $100 \text{ mA h g}^{-1}$  is still maintained (**Figure S4.4**), demonstrating that the present Li-metal current collector configuration shows perspective for full solid-state Li-metal batteries.

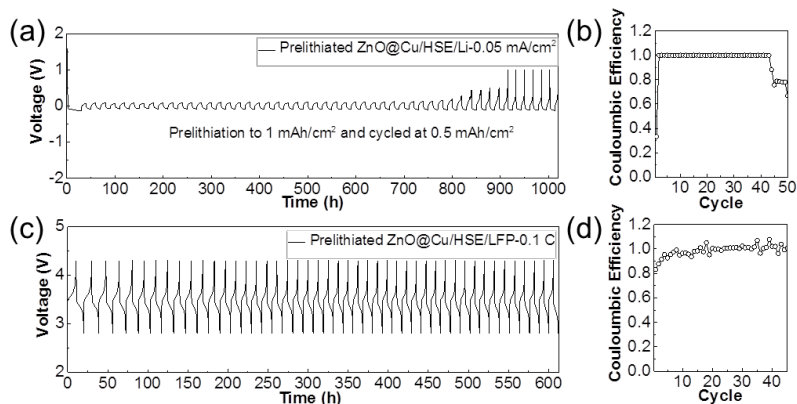


**Figure 4.5** Full cells composed of pre-lithiated ZnO@Cu anode and LFP cathode. (a, b) Electrochemical performance of the ZnO@Cu/HSE/Li battery prelithiated to 1 mA h cm<sup>-2</sup> and cycled at 0.5 mA h cm<sup>-2</sup>. (c, d) Electrochemical performance of the ZnO@Cu/HSE/LFP battery cycled at 0.1 C.

### 4.3 Conclusions

In conclusion, cycling of solid electrolytes in combination with Li-metal anodes is generally demonstrated starting with a thick Li-metal anode. Ideally, the battery is assembled in its discharged state, without a major excess of Li-metal, hence with the solid electrolyte directly facing the current collector. This is a much more challenging condition, in practice leading to severe delamination of the solid electrolyte from the current collector upon repeated Li-metal plating/stripping, resulting in early cell death. Here we explore a potential strategy to improve the HSE/Cu interface by introducing a 100 nm thin film of ZnO on the copper current collector, effectively making the current collector lithium-philic. The conversion reaction upon lithiation results in a regular distribution of small Zn-Li particles, acting as seed crystals for Li-metal plating. A stable solid-state full cell composed of prelithiated ZnO@Cu anode and LiFePO<sub>4</sub> cathode was demonstrated, providing insights in a potential route towards solid-state Li-metal batteries.

### 4.4 Experimental section

Hybrid solid electrolyte (HSE) films were prepared by mixing 0.768 g PEO (Sigma-Aldrich, Mw=600,000), 0.28 g LiTFSI (Sigma-Aldrich), 0.403g SN (Sigma-Aldrich) and 0.105 g LAGP (synthesized by conventional solid sintering method) together in 10 ml acetonitrile (Sigma-Aldrich) and stirring for 24 h. The prepared solution was evenly casted on a Teflon plate and dried in the glove box at room temperature for 24 h. Detailed electrolyte property can be found in our previous publication.<sup>14</sup> The HSE-based all-solid-state cells were assembled in an Ar-filled glove box. These cells consisted of lithium metal, Cu or ZnO@Cu and LiFePO<sub>4</sub> as

negative and positive electrodes, respectively, and the HSE electrolyte and separator layer. Charge-discharge tests of the HSE-based all-solid-state cells were carried out using a Maccor 4000 battery cycler at 25 °C. Lithium metal-plating electrodes were prepared by discharging the cell for 0.2 mA h cm<sup>-2</sup> and 1 mA h cm<sup>-2</sup> capacity. Subsequently, electrodes were transferred into a SEM (JEOL JSM-6010LA) machine under dry Argon conditions, and images were taken using an accelerating voltage of 10 kV. EIS measurements were carried out from 100 kHz to 1 Hz with an alternating current amplitude of 5 mV using an Autolab (PGSTAT302N).

ZnO@Cu was prepared using the Spatial-ALD equipment at TNO-Holst Centre, which relies on the spatial, rather than the conventional temporal distribution of reagent precursors.<sup>34</sup> Depositions are performed at atmospheric pressure while preserving the self-limiting nature of conventional ALD. In this work, a rotary type reactor was used which allows up to 152 mm round substrates to be mounted. More details on the reactor used can be found elsewhere.<sup>35</sup> Depositions were done by mounting Copper foils on a holder and loaded into the S-ALD reactor. The deposition precursors were Diethylzinc (DEZ) and H<sub>2</sub>O, each dosed at 50 sccm and 500 sccm, respectively. The temperature of the precursor bottles was controlled outside the reactor and kept at room temperature for DEZ and at 50 °C for H<sub>2</sub>O. Depositions of 100 nm thickness were performed with 200 rpm substrate rotation frequency and a fixed substrate temperature of 200 °C.

An X-ray photoelectron spectrometer with an Ar<sup>+</sup> beam was employed to investigate the thickness of ALD ZnO on Cu (PHI5000 VersaProbe-II). The applied X-ray source was monochromatic K $\alpha$  X-rays at 1486.6 eV (aluminium anode) under ultrahigh vacuum (10<sup>-9</sup> Torr) conditions. The instrument work function was calibrated to give binding energy (BE) of 83.96 eV for the Au 4f7/2 line on a metallic gold reference sample and the spectrometer dispersion was adjusted to give a BE of 932.62 eV for the Cu 2p3/2 line on a metallic copper sample. The depth-profiling sputtering was conducted by 2 min sputtering in 5 cycles (2 kV, 2×2 mm), the narrow spectra of particular elements were recorded after each cycle of sputtering. The pass energy used for the hemispheric analyzer was 58.7 eV, the base pressure of the system was around 1×10<sup>-7</sup> Pa. The estimated sputtering rates are 5 nm/min.

Neutron depth profiling was performed on thermal neutron beamline A at the Reactor Institute Delft. The detailed setup and working principle can be found in our previous publication.<sup>33</sup> To relate the triton (<sup>3</sup>H<sup>+</sup>) energy loss and intensity to the Li depth and Li density the data needs to be corrected for the stopping power of the materials. The energy-dependent stopping power was calculated using SRIM (2013 version)<sup>36</sup> for the 12  $\mu$ m copper

current collector (density  $8.96 \text{ g cm}^{-3}$ ), and for the electrolyte based on PEO (density  $1.21 \text{ g cm}^{-3}$ ), SN (density  $0.985 \text{ g cm}^{-3}$ ), LiTFSI (density  $1.33 \text{ g cm}^{-3}$ ), LAGP (density  $3.42 \text{ g cm}^{-3}$ ).

### References

- 1 Whittingham, M. S. Electrical energy storage and intercalation chemistry. *Science* **1976**, *192*, 1126-1127.
- 2 Lin, D., Liu, Y.; Cui, Y. Reviving the lithium metal anode for high-energy batteries. *Nat. Nanotech.* **2017**, *12*, 194-201.
- 3 Cheng, X., Zhang, R., Zhao, C.; Zhang, Q. Toward Safe Lithium Metal Anode in Rechargeable Batteries: A Review. *Chem. Rev.* **2017**, *117*, 10403-10473.
- 4 Luntz, A. C.; McCloskey, B. D. Nonaqueous Li-air batteries: a status report. *Chem. Rev.* **2014**, *114*, 11721-11750.
- 5 Manthiram, A., Fu, Y., Chung, S., Zu, C.; Su, Y. Rechargeable lithium-sulfur batteries. *Chem. Rev.* **2014**, *114*, 11751-11787.
- 6 Liu, M., Qin, X., He, Y., Li, B.; Kang, F. Recent innovative configurations in high-energy lithium-sulfur batteries. *J. Mater. Chem. A* **2017**, *5*, 5222-5234.
- 7 Aurbach, D., Zinigrad, E., Cohen, Y.; Teller, H. A short review of failure mechanisms of lithium metal and lithiated graphite anodes in liquid electrolyte solutions. *Solid State Ion.* **2002**, *148*, 405-416.
- 8 Bai, P., Li, J., Brushett, F. R.; Bazant, M. Z. Transition of lithium growth mechanisms in liquid electrolytes. *Energy Environ. Sci.* **2016**, *9*, 3221-3229.
- 9 Ngai, K. S., Ramesh, S., Ramesh, K.; Juan, J. C. A review of polymer electrolytes: fundamental, approaches and applications. *Ionics* **2016**, *22*, 1259-1279.
- 10 Yao, X., Huang, B., Yin, J., Peng, G., Huang, Z., Gao, C., Liu, D.; Xu, X. All-solid-state lithium batteries with inorganic solid electrolytes: Review of fundamental science. *Chin. Phys.* **2015**, *25*, 018802.
- 11 Quartarone, E.; Mustarelli, P. Electrolytes for solid-state lithium rechargeable batteries: recent advances and perspectives. *Chem. Soc. Rev.* **2011**, *40*, 2525-2540.
- 12 Yang, C., Zhang, L., Liu, B., Xu, S., Hamann, T., McOwen, D., Dai, J., Luo, W., Gong, Y., Wachsman, E. D.; Hu, L. Continuous plating/stripping behavior of solid-state lithium

- metal anode in a 3D ion-conductive framework. *Proc. Natl. Acad. Sci.* **2018**, *115*, 3770-3775.
- 13 Zeng, X., Yin, Y., Li, N., Du, W., Guo, Y.; Wan, L. Reshaping lithium plating/stripping behavior via bifunctional polymer electrolyte for room-temperature solid Li metal batteries. *J. Am. Chem. Soc.* **2016**, *138*, 15825-15828.
- 14 Liu, M., Cheng, Z., Ganapathy, S., Wang, C., Haverkate, I., Tulodziecki, M., Unnikrishnan, S.; Wagemaker, M. Tandem Interface and Bulk Li-ion Transport in a Hybrid Solid Electrolyte with Micro-Sized Active Filler. *ACS Energy Lett.* **2019**, *4*, 2336-2342.
- 15 Yue, L., Ma, J., Zhang, J., Zhao, J., Dong, S., Liu, Z., Cui, G.; Chen, L. All solid-state polymer electrolytes for high-performance lithium-ion batteries. *Energy Stor. Mater.* **2016**, *5*, 139-164.
- 16 Zheng, J., Gu, M., Chen, H., Meduri, P., Engelhard, M. H., Zhang, J., Liu, J.; Xiao, J. Ionic liquid-enhanced solid-state electrolyte interface (SEI) for lithium-sulfur batteries. *J. Mater. Chem. A* **2013**, *1*, 8464-8470.
- 17 Xu, K. Electrolytes and interphases in Li-ion batteries and beyond. *Chem. Rev.* **2014**, *114*, 11503-11618.
- 18 Bachman, J. C., Muy, S., Grimaud, A., Chang, H. -, Pour, N., Lux, S. F., Paschos, O., Maglia, F., Lupart, S., Lamp, P., Giordano, L.; Shao-Horn, Y. Inorganic Solid-State Electrolytes for Lithium Batteries: Mechanisms and Properties Governing Ion Conduction. *Chem. Rev.* **2016**, *116*, 140-162.
- 19 Zhang, H., Li, C., Piszcz, M., Coya, E., Rojo, T., Rodriguez-Martinez, L. M., Armand, M.; Zhou, Z. Single lithium-ion conducting solid polymer electrolytes: Advances and perspectives. *Chem. Soc. Rev.* **2017**, *46*, 797-815.
- 20 Goodenough, J. B.; Singh, P. Review-Solid electrolytes in rechargeable electrochemical cells. *J. Electrochem. Soc.* **2015**, *162*, A2387-A2392.
- 21 Shim, J., Kim, L., Kim, H. J., Jeong, D., Lee, J. H.; Lee, J. All-solid-state lithium metal battery with solid polymer electrolytes based on polysiloxane crosslinked by modified natural gallic acid. *Polymer* **2017**, *122*, 222-231.
- 22 Kotobuki, M., Kanamura, K., Sato, Y.; Yoshida, T. Fabrication of all-solid-state lithium battery with lithium metal anode using Al<sub>2</sub>O<sub>3</sub>-added Li<sub>7</sub>La<sub>3</sub>Zr<sub>2</sub>O<sub>12</sub> solid electrolyte. *J. Power Sources* **2011**, *196*, 7750-7754.

- 23 Han, X., Gong, Y., Fu, K. K., He, X., Hitz, G. T., Dai, J., Pearse, A., Liu, B., Wang, H.; Rubloff, G. Negating interfacial impedance in garnet-based solid-state Li metal batteries. *Nat. Mater.* **2017**, *16*, 572-579.
- 24 Yun, Q., He, Y., Lv, W., Zhao, Y., Li, B., Kang, F.; Yang, Q. Chemical dealloying derived 3D porous current collector for Li metal anodes. *Adv. Mater.* **2016**, *28*, 6932-6939.
- 25 Zhang, J. Anode-less. *Nat. Energy* **2019**, *4*, 637-638.
- 26 Shi, Q., Zhong, Y., Wu, M., Wang, H.; Wang, H. High-capacity rechargeable batteries based on deeply cyclable lithium metal anodes. *Proc. Natl. Acad. Sci.* **2018**, *115*, 5676-5680.
- 27 Yang, C., Fu, K., Zhang, Y., Hitz, E.; Hu, L. Protected Lithium-Metal Anodes in Batteries: From Liquid to Solid. *Adv. Mater.* **2017**, *29*, 1701169.
- 28 Wang, C., Gong, Y., Liu, B., Fu, K., Yao, Y., Hitz, E., Li, Y., Dai, J., Xu, S.; Luo, W. Conformal, nanoscale ZnO surface modification of garnet-based solid-state electrolyte for lithium metal anodes. *Nano Lett.* **2017**, *17*, 565-571.
- 29 Xie, Q., Zhang, X., Wu, X., Wu, H., Liu, X., Yue, G., Yang, Y.; Peng, D. Yolk-shell ZnO-C microspheres with enhanced electrochemical performance as anode material for lithium-ion batteries. *Electrochim. Acta* **2014**, *125*, 659-665.
- 30 Zhang, G., Hou, S., Zhang, H., Zeng, W., Yan, F., Li, C. C.; Duan, H. High-performance and ultra-stable lithium-ion batteries based on MOF-derived ZnO@ZnO quantum Dots/C core-shell nanorod arrays on a carbon cloth anode. *Adv. Mater.* **2015**, *27*, 2400-2405.
- 31 Zhang, X., Xiang, Q., Tang, S., Wang, A., Liu, X.; Luo, J. Long Cycling Life Solid-State Li Metal Batteries with Stress Self-Adapted Li/Garnet Interface. *Nano Lett.* **2020**, *20*, 2871-2878.
- 32 Lv, S., Verhallen, T., Vasileiadis, A., Ooms, F., Xu, Y., Li, Z., Li, Z.; Wagemaker, M. Operando monitoring the lithium spatial distribution of lithium metal anodes. *Nat. Commun.* **2018**, *9*, 1-12.
- 33 Liu, M., Cheng, Z., Qian, K., Verhallen, T., Wang, C.; Wagemaker, M. Efficient Li-metal plating/stripping in carbonate electrolytes using a LiNO<sub>3</sub>-gel polymer electrolyte, monitored by operando neutron depth profiling. *Chem. Mater.* **2019**, *31*, 4564-4574.
- 34 Poodt, P., Cameron, D. C., Dickey, E., George, S. M., Kuznetsov, V., Parsons, G. N., Roozeboom, F., Sundaram, G.; Vermeer, A. Spatial atomic layer deposition: A route

- towards further industrialization of atomic layer deposition. *J. Vac. Sci. Technol. A* **2012**, *30*, 010802.
- 35 Illiberi, A., Roozeboom, F.; Poodt, P. Spatial atomic layer deposition of zinc oxide thin films. *ACS Appl. Mater. Interfaces* **2012**, *4*, 268-271.
- 36 Nagpure, S. C., Downing, R. G., Bhushan, B.; Babu, S. S. Discovery of lithium in copper current collectors used in batteries. *Scr. Mater.* **2012**, *67*, 669-672.



Supporting Information for Chapter 4

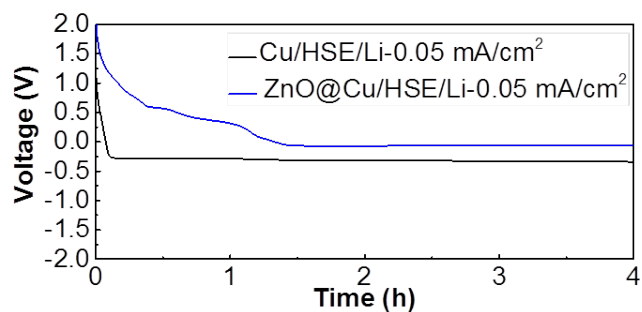


Figure S4.1 The initial discharge curves for Cu/HSE/Li and ZnO@Cu/HSE/Li batteries cycled at current density of  $0.05 \text{ mA cm}^{-2}$ .

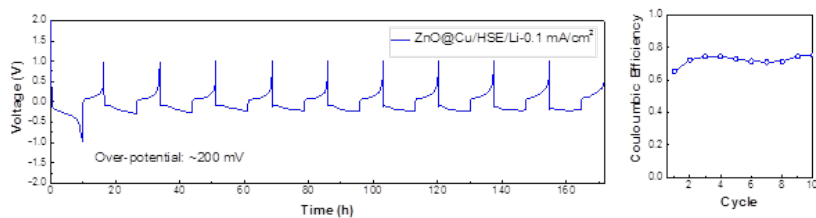


Figure S4.2 Electrochemical performance of ZnO@Cu/HSE/Li batteries cycled at  $0.1 \text{ mA cm}^{-2}$  for 10 h.

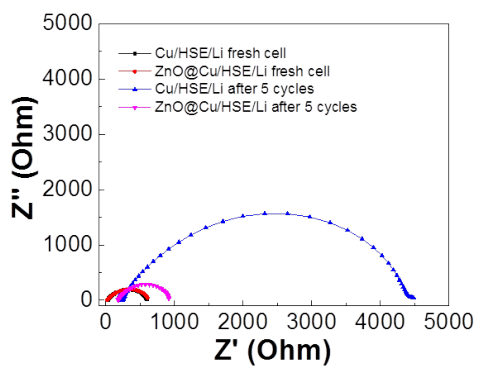


Figure S4.3 The impedance evolution for Cu/HSE/Li and ZnO@Cu/HSE/Li batteries before and after 5 cycles.

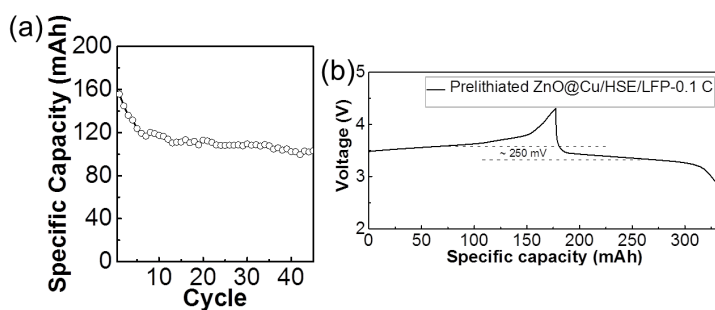
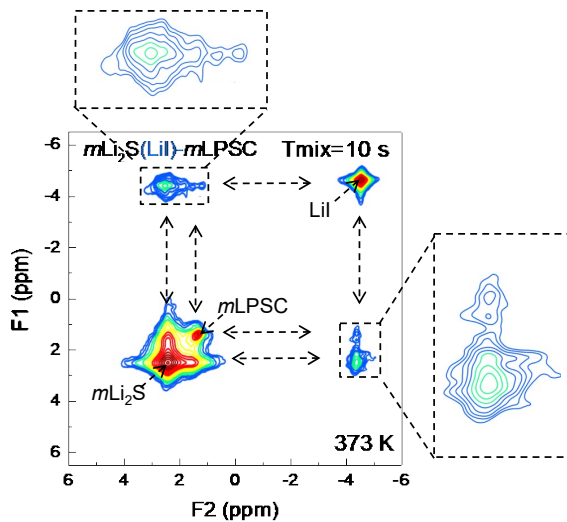


Figure S4.4 Specific capacity and initial capacity-voltage profiles of the ZnO@Cu/HSE/LFP battery cycled at 0.1 C.



## Chapter 5 Quantifying the local Li-ion diffusion over the grain boundaries of a protective coating, revealing the impact on the macroscopic Li-ion transport in an all-solid-state battery



In this work, the three-phase Li-ion transport, between solid electrolyte (Li<sub>6</sub>PS<sub>5</sub>Cl), coating(LiI) and electrode(Li<sub>2</sub>S) is directly observed and quantified using exchange-NMR, thus uniquely disentangling the impact of the coating on the Li<sup>+</sup> diffusion.

**This chapter is based on:**

**Chao Wang**, Ming Liu, Chenglong Zhao, Eveline van der Maas, Kui Lin, Violetta A. Arzelewska, Baohua Li, Swapna Ganapathy and Marnix Wagemaker, Quantifying the local Li-ion diffusion over the grain boundaries of a protective coating, revealing the impact on the macroscopic Li-ion transport in an all-solid-state battery, submitted.

### Abstract

The key challenge for solid-state-batteries is to design electrode-electrolyte interfaces that combine (electro)chemical and mechanical stability with facile Li-ion transport. Typically, this presents conflicting demands, that the solid electrolyte-electrode interface-area should be maximized to facilitate high currents, but should be minimized to reduce the parasitic interface reactions. Addressing these issues would greatly benefit from establishing the impact of interface coatings on local Li-ion transport, which presents an experimental challenge. Here, the three-phase Li-ion transport, between solid electrolyte, coating and electrode is directly observed and quantified using exchange-NMR. A  $\text{Li}_2\text{S}$  cathode is coated by  $\text{LiI}$ , providing a ductile and conductive interface with the argyrodite-sulfur electrolyte, which enhances the interface transport to such an extent that the common nanosizing of the cathodic mixture can be abandoned. The result is facile sulfur activation, preventing solid-electrolyte decomposition, in micron-sized cathodic mixtures, providing insights into the role of coatings and perspective for sulfur-based solid-state-batteries.

### 5.1 Introduction

All-solid-state lithium(Li)-ion batteries are promising candidates for next-generation high energy density and safe energy storage technology<sup>1-2</sup>. As a liquid-free system, it generally does not suffer from leakage and gas generation and the risk of a thermal runaway, inherent to liquid electrolytes used in conventional Li-ion batteries<sup>3-7</sup>. As a result, research has intensified towards solid electrolytes that display conductivities approaching, or even exceeding that of liquid electrolytes, including structural families such as LISICON, argyrodites, garnets, and NASICON-type structures<sup>6, 8-10</sup>.

A major obstacle for solid-state batteries is the high internal resistance for Li<sup>+</sup> transfer over the solid-solid electrode-electrolyte interface<sup>11-12</sup> which may be due to poorly conducting electrolyte decomposition products<sup>4, 13</sup>, contact loss due to volumetric changes<sup>4, 14</sup> and space-charges<sup>15-16</sup>. The commonly applied strategy to lower the resistance for Li<sup>+</sup> transport, is to enlarge the electrolyte-electrode interface area, often expressed as “ionic contact area”, by nanosizing the electrode and electrolyte particles<sup>17-19</sup>. However, with the interface area between electrolyte and electrode, the detrimental chemical and electrochemical reactions also scale at the interfaces between the electrolyte and electrode, raising the internal resistance for Li<sup>+</sup> transport. Thus, from the perspective of stability, larger electrolyte and electrode particles in the micron range are preferred, having the additional advantage of being more suitable for practical production<sup>20</sup>. However, this puts even higher demands on improving the Li<sup>+</sup> transport over the relatively small ionic contact area between micron-sized solid electrolyte-electrode particles.

Addressing both stability and Li<sup>+</sup> transport at the interfaces has led to the development of interphases, often realized through coating processes<sup>6, 18-19</sup>. The demands on these interphases are challenging, including (electro)chemical stability towards both electrode and electrolyte, poor electronic conductivity and at least reasonable ion conductivity, and a low grain boundary resistance with both solid electrode and electrolyte which typically is achieved with good wettability (low interface energy) and soft materials (low Young’s modulus and/or yield point). One of the challenges is to assess the impact of interphases on the local Li<sup>+</sup> transport, which can provide valuable insights for interphase design and preparation methodologies. Where the macroscopic charge transfer resistance is most often estimated by electrochemical impedance spectroscopy<sup>21-22</sup>, disentangling the three-phase diffusion between the electrode, interphase/coating and electrolyte is yet to be accomplished.

One of the solid electrolyte-electrode combinations where interphase strategies are intensively investigated is sulfur-based solid electrolyte in combination with sulfur cathodes, providing a high energy density in combination with cheap raw materials and synthesis. Sulfide-based electrolytes (such as  $\text{Li}_2\text{S-P}_2\text{S}_5$  and  $\text{Li}_6\text{PS}_5\text{X}$  ( $\text{X}=\text{Cl}$ ,  $\text{Br}$  and  $\text{I}$ )) are especially promising due to their high ionic conductivity and relatively low grain boundary resistance<sup>23-26</sup>. These advantages, unfortunately, come along with a major drawback, which is a very small electrochemical stability window<sup>13, 27-28</sup>. This is one of the main reasons for the extremely sluggish  $\text{Li}^+$  transport over the solid-solid  $\text{Li}_2\text{S}$ -solid electrolyte interface during battery operation, especially when micron-sized solid electrolyte particles are used<sup>3-4, 29-31</sup>. An additional challenge is the activation of solid sulfur cathodes due to the very low  $\text{Li}^+$  diffusivity<sup>32-34</sup>, which also demands a relatively large ionic contact area<sup>35</sup>. To improve the  $\text{Li}^+$  interfacial transport the two applied strategies are; bilayer solid electrolytes design (porous layer and dense layer)<sup>30, 36-37</sup> and mixing in binary lithium halide salts (such as  $\text{LiBr}$ ,  $\text{LiI}$ ) additives<sup>29-31, 38-40</sup>. Because of the large cost and sophisticated process associated with the former, halide salt addition appears especially promising for practical application. The lower internal resistance of these three-phase mixtures has been argued to be the result of the small Young's modulus (softness) of the halide salts, which effectively act as a solid wetting agent for the electrode/electrolyte interface<sup>29-31, 38-40</sup>. However, how the halogen salt affects the local  $\text{Li}^+$  transport over the grain boundaries (electrolyte-halogen salt, halogen salt-electrode and electrolyte-electrode) is difficult to establish, and especially important to develop a fundamental understanding and guide to the design of the optimal geometry and preparation of these interphases.

Making use of the ability of solid-state nuclear magnetic resonance (NMR) to characterize the spontaneous  $\text{Li}^+$  exchange between solid electrolyte and electrode phases in solid-state cathodes<sup>41-42</sup>, the present work explores the three-phase  $\text{Li}^+$  transport between the  $\text{Li}_2\text{S}$  electrode,  $\text{LiI}$  coating and argyrodite  $\text{Li}_6\text{PS}_5\text{Cl}$  solid electrolyte, aiming to gain insight in the role of the coating in  $\text{Li}$ -ion transport in solid-state batteries. The difference in NMR chemical shift of the three phases allows unravelling the diffusivity between each phase via  $^6\text{Li}$  2D-EXSY experiments. The sluggish  $\text{Li}^+$  diffusion over the  $\text{Li}_2\text{S}$ -argyrodite interface is drastically improved by the presence of a  $\text{LiI}$  coating, where the  $\text{Li}^+$  diffusion is shown to proceed through the  $\text{LiI}$  coating. The activation energy between the three phases is equal to the bulk activation energy for  $\text{Li}^+$  diffusion in  $\text{LiI}$ , demonstrating the extremely low grain boundary resistance achieved by the facile  $\text{LiI}$  coating strategy. The practical consequence during battery operation is that this prevents large overpotentials during battery cycling, even at a relatively low ionic contact area between the cathode and microscopic solid electrolyte particles. This is fortuitous, as it makes the working potential

fall within the electrochemical stability window of the argyrodite solid electrolyte. The result is a solid-state battery that can be activated at a very low applied voltage and can cycle with high reversibility under a modest 2 MPa pressure for over 200 cycles. The ability to monitor the local  $\text{Li}^+$  transport over the grain boundaries in this three-phase system provides valuable insight in the role of coatings in achieving low interphase resistances using micron-sized solid electrolyte particles, guiding the design of stable high-performance interphases, which are crucial aspects for future solid-state batteries.

## 5.2 Methods

### 5.2.1 Solid electrolyte and cathode active materials preparation

The solid-state electrolyte  $\text{Li}_6\text{PS}_5\text{Cl}$  (denoted as LPSC) was prepared by a simple solid-state reaction. The stoichiometric raw materials  $\text{LiCl}$  (Sigma-Aldrich),  $\text{P}_2\text{S}_5$  (Sigma-Aldrich), and  $\text{Li}_2\text{S}$  (Sigma-Aldrich) were used as the starting materials and were ball milled at 110 rpm, 2hrs with the  $\text{ZrO}_2$  coated jars using 18  $\text{ZrO}_2$  balls. After the ball milling, the precursor was sealed in a quartz tube with Ar and then annealed at 550 °C for 15 hours to obtain the LPSC solid electrolyte. These were subsequently crushed with an agate mortar-pestle before using the samples for further measurements. For the preparation of the  $\text{Li}_2\text{S}$ - $\text{LiI}$  mixtures, proportional 10 mmol  $\text{Li}_2\text{S}$  and 3.33 mmol  $\text{LiI}$  were dissolved into 1 ml ethanol and stirred for 10 mins then heated at 300 °C until totally dry.

### 5.2.2 Material characterization

Powder X-ray diffraction (XRD) patterns were collected over a two-theta range of 10–80° to identify the crystalline phases of the prepared materials using  $\text{CuK}\alpha$  X-rays (1.5406 Å at 45 kV and 40 mA) on an X'Pert Pro X-ray diffractometer (PANalytical). To prevent reaction with moisture and oxygen, the powder materials were sealed in an airtight XRD sample holder in an argon-filled glove box. For the TEM and energy dispersive X-ray (STEM-EDX) investigations, a suspension in dry ethanol was prepared, which was drop casted onto a standard gold grid with a holey carbon film under a high temperature, inside an argon-filled glove box. To prevent any contact with air TEM grids with the sample were loaded into a custom-made vacuum transfer TEM holder. TEM measurements were carried out in a FEI-Tecnaï operating at 200 kV. FE-SEM (JEOL JSM-6010LA) images were taken under dry Argon conditions and taken using an accelerating voltage of 10 kV. The depth-profiling sputtering was conducted by 2 min of sputtering in five cycles (2 kV, 2 mm × 2 mm), the narrow spectra of particular elements were recorded after each cycle of sputtering. The pass energy used for the hemispheric analyzer was 58.7 eV, and the base pressure of the system was about  $10^{-7}$  Pa. The estimated sputtering rates are 5 nm/min.



### 5.2.3 Solid-state lithium battery preparation and electrochemical performance

Solid-state cells were assembled in an argon-filled glove box in the following steps: 150 mg of LPSC was pressed relative tightly under pressure of 0.5 Mpa as the electrolyte layer, and then 12.5 mg of cathode mixture and In-Li foil were added to both sides of the electrolyte layer, separately. After that, 2 MPa pressure was used to press these three layers together for 30 s. The assembled cells were charged and discharged under specific current densities to evaluate their electrochemical performances.

### 5.2.4 Solid-state $^6\text{Li}$ NMR measurements

Solid-state NMR measurements were performed on a Bruker Ascend 500 spectrometer ( $B_0 = 11.7$  T) with a NEO console operating at the  $^6\text{Li}$  resonance frequency of 73.578 MHz. The  $\pi/2$  pulse length was determined to be 3.9  $\mu\text{s}$  with an RF field strength of 64 kHz. Chemical shifts were referenced with respect to a 1 M LiCl solution. A Bruker two-channel MAS WVT 4 mm probe was used for all measurements. One pulse experiment was performed under MAS at a spinning speed of 10 kHz. A recycle delay of three times of  $T_1$  was used each time. Two-dimensional exchange spectroscopy (2D-EXSY) measurements were performed for the mixture at a spinning speed of 10 kHz and at various mixing times ranging from 10 ms up to 10 s and at temperatures from 20 to 100  $^\circ\text{C}$ . All 2D spectra consist of 16 scans for each of the 32 transients, each transient incremented by 800  $\mu\text{s}$  with a recycle delay of up to 50 s. The exchange between the  $\text{Li}_2\text{S}$  and LPSC phases was quantified by fitting the evolution of the cross-peak intensity as a function of  $T_{\text{mix}}$  to a diffusion model derived from Fick's law, which has been described previously<sup>4, 24</sup>.

## 5.3 Results and discussion

### 5.3.1 Stability of solid electrolytes, nanosized versus micronized

The electrochemical stability of solid electrolytes was recently shown to be significantly lower than initially thought, especially for sulfide-based solid electrolytes, where consequential decomposition reactions have been shown to have a large detrimental impact on the all-solid-state battery performance<sup>10, 43-44</sup>. To demonstrate the redox activity of the sulfur solid electrolyte material and the impact of particle size, several mixtures of sulfur solid electrolytes with carbon are electrochemically cycled. As shown in **Figure 5.1a** and **b**, when nanosized  $\text{Li}_3\text{PS}_4$  ( $n\text{LPS}$ ) and  $\text{Li}_6\text{PS}_5\text{Cl}$  ( $n\text{LPSC}$ ) are mixed with conductive carbon (referred to as  $n\text{LPS-C}$  and  $n\text{LPSC-C}$  respectively), they are readily oxidized at low oxidation potentials,  $<2$  V vs. In ( $<2.62$  V vs.  $\text{Li}/\text{Li}^+$ ), at a relatively low current density of  $0.033$  mA/cm<sup>2</sup>, in agreement with recent findings<sup>10, 25</sup>. This illustrates that the decomposition of nanosized

solid electrolytes in cathodic mixtures is the prime reason for the short cycle life of current all-solid-state batteries utilizing sulfide solid electrolytes<sup>25</sup>. The combination of a  $\text{Li}_2\text{S}$  cathode and the LPSC electrolyte has been intensively studied<sup>3-4, 29-30</sup>, where the harsh activation process of  $\text{Li}_2\text{S}$ , caused by the low bulk conductivity of  $\text{Li}_2\text{S}$ , and sluggish  $\text{Li}^+$  transport between the electrode and electrolyte represent another critical issue. A straightforward approach to achieve easier activation of  $\text{Li}_2\text{S}$  and to improve the  $\text{Li}^+$  transport between the electrode and electrolyte is to reduce the particle size of both the  $\text{Li}_2\text{S}$  and the LPSC (here referred to as  $n\text{Li}_2\text{S}-n\text{LPSC-C}$  electrode). Accompanied by a large overpotential of about 800 mV, this results in a capacity during the first charge and discharge and upon subsequent cycling, as shown in **Figure 5.1f** and **Figure S5.1**, which is hard to distinguish from the capacity of the electrolyte itself (because oxidation of LPSC is carried by the  $\text{S}^{2-}/\text{S}^0$  redox).

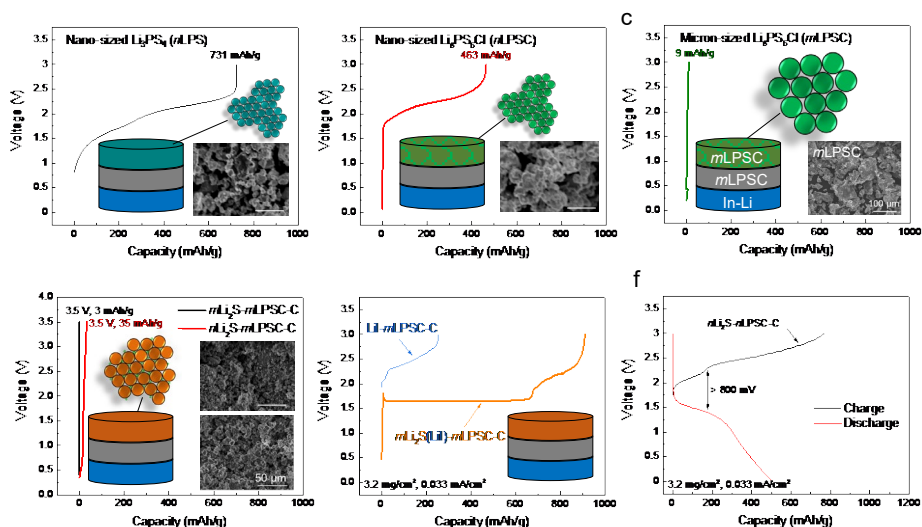


**Figure 5.1** Voltage as a function of the capacity of solid sulfur electrolyte, carbon mixtures, and solid-state sulfur electrodes. Voltage profiles of (a) nanosized (n) nLPSC-, (b) nLPSC-C and (c) micron-sized (m) mLPSC-C cathodes; In this configuration, the solid electrolyte acts as a cathode electrode material, which allows direct evaluation of the electrochemical activity as these would occur in a solid-state battery, excluding specific (electro)chemical reactions with a cathode material. (d) Activation voltage profiles of  $m\text{Li}_2\text{S}-m\text{LPSC-C}$ ,  $n\text{Li}_2\text{S}-m\text{LPSC-C}$  cathodes; (e, f) Voltage profiles of  $m\text{Li}_2\text{S}(\text{LiI})-m\text{LPSC-C}$ ,  $\text{LiI}-m\text{LPSC-C}$  and  $n\text{Li}_2\text{S}-n\text{LPSC-C}$  cathodes; For all voltage profiles the current density is  $0.033 \text{ mA cm}^{-2}$ .

The simplest strategy to reduce the contribution of the solid electrolyte to the capacity is to lower the active area of ionic contact through the use of micron-sized solid electrolyte particles. To verify the smaller redox activity, micron-sized LPSC (average diameter of  $50 \mu\text{m}$ , as shown in **Figure S5.2**) was mixed with carbon, and charged (oxidized) to 3 V vs. In-Li

(3.62 vs. Li/Li<sup>+</sup>) in the solid-state battery configuration, referred to as *m*LPSC-C electrode. The result, shown in **Figure 5.1c**, demonstrates nearly no contribution of the LPSC solid electrolyte to the capacity, reflecting the smaller amount of decomposition reactions under the same current density. However, as expected, the small area of ionic contact of micron-sized LPSC compromises ion transport, leading to a very small capacity of the sulfur active material, even when nanosized Li<sub>2</sub>S is employed as shown in **Figure 5.1d**. Although nanosized Li<sub>2</sub>S displays a slightly larger capacity, the rapid voltage increases to the 3.5 V vs. In-Li (4.12 vs. Li/Li<sup>+</sup>) cut-off demonstrates that in both cases the sulfur cathode material is marginally activated. At the same time, decreasing the ionic contact area increases the internal resistance and thus the overpotentials experienced at the solid electrolyte, which will induce decomposition reactions and thus driving a self-amplifying resistance growth towards battery failure.

The mechanical mixing of halogen salts like LiI with Li<sub>2</sub>S and sulfide solid electrolytes is an often-applied strategy, to improve conductivity, although the exact mechanism has not been clarified<sup>29-31, 38-39</sup>. At present we take a different and more controlled approach, aiming to introduce LiI at the Li<sub>2</sub>S-LPSC interfaces. Rather than using the conventional ball-milling route, this is achieved by introducing LiI via solution, making use of the much better solubility of LiI in ethanol compared to Li<sub>2</sub>S (see supporting information **Figure S5.3**). The solution was then evaporated at 300 °C (**Figure S5.3**) to obtain a LiI-Li<sub>2</sub>S (1:3 molar ratio) composite, where LiI precipitates on the surface of Li<sub>2</sub>S as discussed below. This cathode was subsequently hand-mixed with LPSC and C (referred to *m*Li<sub>2</sub>S(LiI)-*m*LPSC-C) to prepare the cathodic mixture and an all-solid-state *m*Li<sub>2</sub>S(LiI)-*m*LPSC-C|*m*LPSC|In-Li battery was assembled under 2 MPa pressure. This has a large impact on the charging, as shown in **Figure 5.1e**, demonstrating that the introduction of LiI results in a very low sulfur redox activation plateau at 1.69 V vs. In (2.31 V vs. Li/Li<sup>+</sup>) of the micron-sized Li<sub>2</sub>S combined with micron-sized LPSC. The plateau is followed by a rapid increase in potential which most likely reflects oxidation of the solid electrolyte and/or of LiI (to LiI<sub>3</sub> which is known to occur at about 2.3 V vs. In)<sup>45-46</sup>. To identify the contribution of the LiI and/or LPSC oxidation, this measurement was repeated in a battery without Li<sub>2</sub>S, shown in **Figure 5.1e**, leading to charging at a higher voltage marking the oxidation of LPSC and/or LiI.

In conclusion, deposition of LiI on Li<sub>2</sub>S via solution, and hand mixing this cathode with LPSC results in an extremely low activation (oxidation) potential for Li<sub>2</sub>S, suggesting that facile Li<sup>+</sup> transport between the electrode and electrolyte is achieved even for a relatively small ionic contact area between the micron-sized solid electrolyte and the electrode particles.

## 5.3.2 Electrode and Lil coating synthesis and characterization

To understand the role of Lil in the activation of  $\text{Li}_2\text{S}$ , a detailed structural investigation was performed. Both Lil and  $\text{Li}_2\text{S}$  have a cubic structure indexed to the  $Fd\bar{3}m$  space group. Three  $\text{Li}_2\text{S}$ -Lil composites were prepared via dissolution and precipitation where  $\text{Li}_2\text{S}$ :Lil molar ratios of 9:1, 3:1, and 1:1 was added to ethanol, followed by evaporation of the solution at 300 °C.  $\text{Li}_2\text{S}$  and Lil were also individually dissolved and precipitated from ethanol via evaporation for comparison. X-ray patterns of pristine  $\text{Li}_2\text{S}$  and Lil, precipitated  $\text{Li}_2\text{S}$  and Lil and the three  $\text{Li}_2\text{S}$ -Lil composites are provided in **Figure 5.2a** and **S5.4**. From a cursory inspection, it can be observed that the peaks corresponding to the precipitated  $\text{Li}_2\text{S}$  are much broader than those of the parent  $\text{Li}_2\text{S}$ , while the peak width of precipitated Lil is comparable to the parent Lil. This indicates that on precipitation smaller primary crystallites of  $\text{Li}_2\text{S}$  are obtained. In the three composite mixtures, both the  $\text{Li}_2\text{S}$  and Lil phases could be indexed, albeit with shifts in peak positions of the  $\text{Li}_2\text{S}$  component indicating changes in lattice parameters of this phase. Rietveld refinement was further performed of all the patterns depicted in **Figure S5.5**, and the lattice parameters obtained from the refinement are given in **Figure S5.4**. It can be seen that the lattice parameter of Lil (6.025 Å) remains unchanged from that of the pristine material. On the other hand, with increasing amounts of Lil in the composite, the lattice parameter of  $\text{Li}_2\text{S}$  keeps increasing from 5.701 Å (pristine) to 5.750 Å (1 $\text{Li}_2\text{S}$ :1Lil), which could be due to the much smaller average crystallite size of 9.18 nm (1 $\text{Li}_2\text{S}$ :1Lil) compared to 162.92 nm (pristine) as shown in **Figure S5.6** or by incorporation of some iodine in the  $\text{Li}_2\text{S}$  lattice.

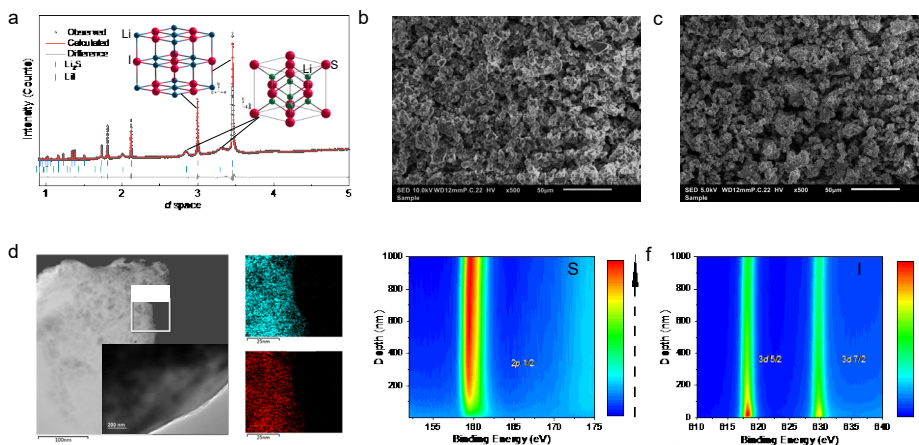


**Figure 5.2** Structural characterizations of the active materials. (a) XRD pattern of the  $\text{Li}_2\text{S}$ -Lil materials. The pattern is fit with the Rietveld method as implemented in GSAS; (b, c, d) SEM images, TEM images and energy spectrum of the  $\text{Li}_2\text{S}$  and  $\text{Li}_2\text{S}$ -Lil (3:1) materials; (e, f) S 2p and I 3d XPS depth profiles of the pristine  $\text{Li}_2\text{S}$ -Lil (3:1) materials.

Additional SEM and TEM measurements are performed to study the morphology of the pristine  $\text{Li}_2\text{S}$  and the  $\text{Li}_2\text{S}$ -LiI mixture. As shown in **Figure 5.2c**, the prepared mixture consists of a microstructure comprising of micron-sized secondary particles with a relatively uniform particle size of around  $5\ \mu\text{m}$  similar to pristine  $\text{Li}_2\text{S}$  in **Figure 5.2b**. TEM is used to study the morphology at smaller length scales ( $100\ \text{nm}$ ). As seen from the TEM image and energy spectrum (**Figure 5.2d**), the EDS mapping of the particle surface shows uniform S and I distribution, indicating a mixture on the nanoscale was obtained with this precipitation method, and the LiI was uniformly distributed over the surface structure of  $\text{Li}_2\text{S}$  particles. To further verify the structure of the  $\text{Li}_2\text{S}$ -LiI material, XPS depth profiling was performed as shown in **Figure 5.2e and f**. The S 2p XPS signal is relatively low until a depth of  $\sim 100\ \text{nm}$ , and vice versa the I 3d is relatively high to approximately the same depth (selected window diameter is as small as  $14\ \mu\text{m}$  to locate only a few particles). Therefore, the present precipitation method results in micron-sized secondary cathode particles, referred to as  $\text{mLi}_2\text{S}(\text{LiI})$ , that exist of agglomerates of LiI coated nanosized primary  $\text{Li}_2\text{S}$  particles, where the micron-sized agglomerates are coated by a relatively thick LiI layer at some positions accumulating to large domains of LiI (as observed with XRD).

### 5.3.3 Li-ion conductivity and role of LiI in the Li-ion transport mechanism

To investigate the impact of the LiI coating on the conductivity impedance spectroscopy and  $^6\text{Li}$  solid NMR spectroscopy are performed. The temperature dependence of the ionic conductivities for the pristine  $\text{Li}_2\text{S}$  and LiI as well as pellets of the 3:1  $\text{Li}_2\text{S}$ -LiI composite are presented in **Figure 5.3a**. The conductivity of all the materials follows an Arrhenius law, resulting in activation energies of 0.235, 0.107 and 0.212 eV for the  $\text{Li}_2\text{S}$ , LiI and  $\text{Li}_2\text{S}$ -LiI mixture, respectively. The room-temperature conductivity of the  $\text{Li}_2\text{S}$ -LiI mixture ( $6.72 \times 10^{-9}\ \text{S cm}^{-1}$  at  $25\ ^\circ\text{C}$ ) is between that of  $\text{Li}_2\text{S}$  ( $7.51 \times 10^{-11}\ \text{S cm}^{-1}$  at  $25\ ^\circ\text{C}$ ) and LiI ( $0.97 \times 10^{-7}\ \text{S cm}^{-1}$  at  $25\ ^\circ\text{C}$ ), indicating that the LiI in the  $\text{Li}_2\text{S}$  agglomerates enhances the overall conductivity of the cathode material. To investigate the role of LiI as interphase material between the  $\text{Li}_2\text{S}$  electrode and LPSC solid electrolyte, (2D)  $^6\text{Li}$ - $^6\text{Li}$  exchange (2D-EXSY) solid-state NMR experiments are performed. These experiments can provide selective and non-invasive quantification of the spontaneous  $\text{Li}^+$  diffusion, charge transfer, over the solid-solid electrolyte–electrode interface in realistic solid-state cathode mixtures, as previously reported<sup>4, 24</sup>.

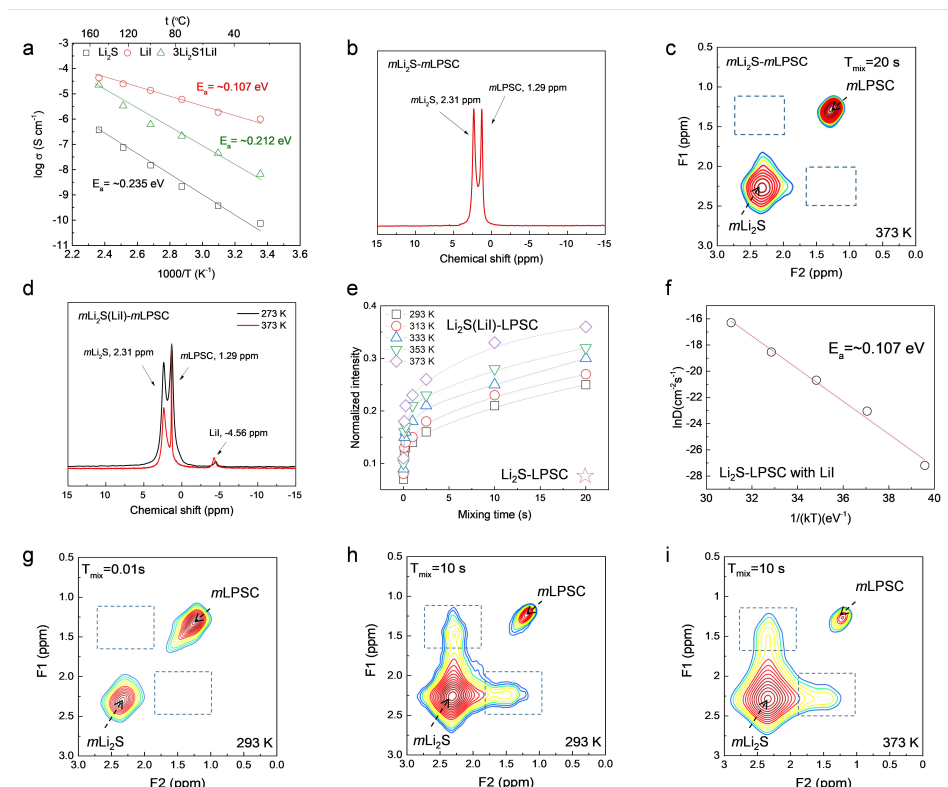


**Figure 5.3** Conductivity of the cathodes and quantification of the  $\text{Li}^+$  transfer across the electrode-electrolyte interface. (a) Ionic conductivity determined by impedance spectroscopy of pellets of  $\text{Li}_2\text{S}$ ,  $\text{LiI}$  and the  $\text{Li}_2\text{S}$ - $\text{LiI}$  mixture at different temperatures. (b, c) One-dimensional (1D)  $^6\text{Li}$  magic angle spinning (MAS) and two-dimensional (2D)  $^6\text{Li}$ - $^6\text{Li}$  exchange (2D-EXSY) NMR spectra of the  $\text{mLi}_2\text{S}$ - $\text{mLPSC}$  cathode mixtures at a mixing time of 20 s, where  $\text{Li}_2\text{S}$  and  $\text{LPSC}$  are both micron-sized. No obvious off-diagonal cross-peak intensity is observed, indicating that the exchange of  $\text{Li}^+$  over the solid-solid  $\text{LPSC}$ - $\text{Li}_2\text{S}$  interface is very small. (d) 1D  $^6\text{Li}$  MAS spectra corresponding to the  $\text{mLi}_2\text{S}(\text{LiI})$ - $\text{mLPSC}$  cathode mixtures at 273 and 373 K. (e) Evolution of the cross-peak intensity as a function of  $T_{\text{mix}}$  obtained from the temperature-dependent 2D-EXSY measurements. (f) Temperature dependence of the diffusion coefficient obtained from fitting the data in (e) to a diffusion model described in detail in reference <sup>24</sup>. These can be fitted with an Arrhenius law, yielding an activation energy ( $E_a$ ) of 0.107 eV. (g-i) Two-dimensional  $^6\text{Li}$ - $^6\text{Li}$  exchange spectra of the mixture of micron-sized  $\text{LPSC}$  and  $\text{Li}_2\text{S}$ - $\text{LiI}$  (3:1) cathodes measured at a spinning speed of 10 kHz at (g,h) 293 K with mixing times of 0.01 s and 10 s and at (i) 373 K with a mixing time of 10 s. The spectra consist of 16 scans for each of the 32 slices, each slice incremented by 8 ms with a recycle delay of 50 s. The cross-peak at the off-diagonal positions in the dashed boxes represent the diffusion of  $\text{Li}$ -ions between solid electrolyte and electrode.

The one-dimensional (1D)  $^6\text{Li}$  magic angle spinning (MAS) NMR spectra of the micron-sized  $\text{Li}_2\text{S}$ - $\text{LPSC}$  cathode mixture, shown in **Figure 5.3b**, displays two resonances with chemical shifts of 2.31 and 1.29 ppm, representing  $\text{Li}$  in  $\text{Li}_2\text{S}$  and in  $\text{LPSC}$  respectively. MAS can average out anisotropic interactions that are described by rank-2 tensors, such as dipolar, first-order

quadrupolar and chemical shift anisotropy. Compared to  $\text{Li}_2\text{S}$ , the larger screening of  $\text{Li}^+$  in the LPSC results in the upfield  $^6\text{Li}$  chemical shift position. The difference in chemical shift between Li in  $\text{Li}_2\text{S}$  and LPSC, which allows distinguishing both species, making it possible to conduct the 2D exchange experiments. In the 2D exchange spectrum, **Figure 5.3c**, both  $\text{Li}^+$  environments are clearly observed, where the more LPSC narrow resonance is due to the higher mobility of  $\text{Li}^+$  in the solid electrolyte. 2D exchange NMR effectively measures the spectrum of the  $^6\text{Li}$  ions at  $t=0$  s, then waits a mixing time  $T_{mix}$ , and subsequently measure the spectrum of the same ions again at  $t=T_{mix}$ .  $\text{Li}^+$  diffusion over the grain boundaries between the two chemical Li environments ( $\text{Li}_2\text{S}$  and in LPSC) should result in off-diagonal cross-peaks, positioned in the dotted box in **Figure 5.3c**. The intensity of these cross-peaks reflects the amount of  $\text{Li}^+$  exchange, which is expected to increase when the diffusion time ( $T_{mix}$ ) and temperature are increased<sup>4</sup>. The absence of off-diagonal intensity, even for the maximum  $T_{mix}$  and temperature ( $T_{mix}=20\text{s}$ , 373K) indicates that the  $\text{Li}^+$  exchange (flux) over the solid-solid interface between LPSC and  $\text{Li}_2\text{S}$  (without Lil coating), is too small to be observed, reflecting sluggish  $\text{Li}^+$  mobility across the interface with the solid electrolyte. This rationalizes the observation in **Figure 5.1d**, that these mixtures do not facilitate activation of  $\text{Li}_2\text{S}$ . As expected, the addition of Lil to the cathodic mixture,  $m\text{Li}_2\text{S}(\text{Lil})-m\text{LPSC}$ , results in the appearance of the Li resonance at -4.56 ppm associated with Lil, in the 1D  $^6\text{Li}$  NMR spectrum (**Figure 5.3d**). The impact of the Lil on the spontaneous  $\text{Li}^+$  charge transfer, over the  $\text{Li}_2\text{S}$ -LPSC interface is dramatic, as can be observed in **Figure 5.3e-i**. At short mixing time,  $T_{mix} = 10$  ms, no appreciable cross-peak intensity is observed in the 2D EXSY spectrum (**Figure 5.3g**). However, increasing the mixing time,  $T_{mix}$ , to 10 s, and raising the temperature to 373 K, results in a strong cross-peak intensity (**Figure 5.3h and i**), which is a measure of the  $\text{Li}^+$  exchange between  $\text{Li}_2\text{S}$  and LPSC. The evolution of the normalized cross-peak intensity as a function of  $T_{mix}$  measured at a range of temperatures and a  $T_{mix}$  range of 10 ms –10 s is provided in **Figure 5.3e**. The exchange between the  $\text{Li}_2\text{S}$  and LPSC phases was quantified by fitting the evolution of the cross-peak intensity as a function of  $T_{mix}$  to a diffusion model derived from Fick's law, described elsewhere by us<sup>24</sup>. From the fit, the diffusion coefficient (D) as a function of temperature can be obtained, which in this case pertains to Li-ion transport across the  $\text{Li}_2\text{S}$ -LPSC interface. The diffusion coefficients as a function of temperature obtained from the fit are given in **Figure 5.3f**. The data for  $\text{Li}_2\text{S}$ -LPSC diffusion can be fitted to an Arrhenius law, yielding an activation energy of 0.107 eV for the charge transfer. This activation energy equals that of Lil as measured by the impedance of the pure phase, suggesting that Lil is responsible for lowering the interfacial barrier between electrode and electrolyte. The value for the activation energy and observed  $\text{Li}^+$  exchange is comparable to that obtained for interfacial diffusion between nanosized  $\text{Li}_2\text{S}$  and nanosized (average particle size about 100 nm) LPSC argyrodite (0.10-0.13 eV)<sup>3-4</sup>. The

remarkable conclusion is that despite the small ionic contact area of the present micron-sized LPSC (average particle size about 50  $\mu\text{m}$ ) in the cathodic mixtures, the interface transport is improved to such an extent that it matches that of nanostructured mixtures having a much larger ionic contact area. The two orders of magnitude difference in diameter between the LPSC in the cathodic mixtures, suggests that the Lil improves the  $\text{Li}^+$  diffusion over the interface with 4 orders of magnitude.

To understand the role of the Lil in the diffusion, **Figure 5.4a** focuses on the exchange of Li in  $\text{Li}_2\text{S}$  and LPSC with Lil, hence the three-phase Li-ion exchange in the 2D EXSY measurements shown in **Figure 5.3**.

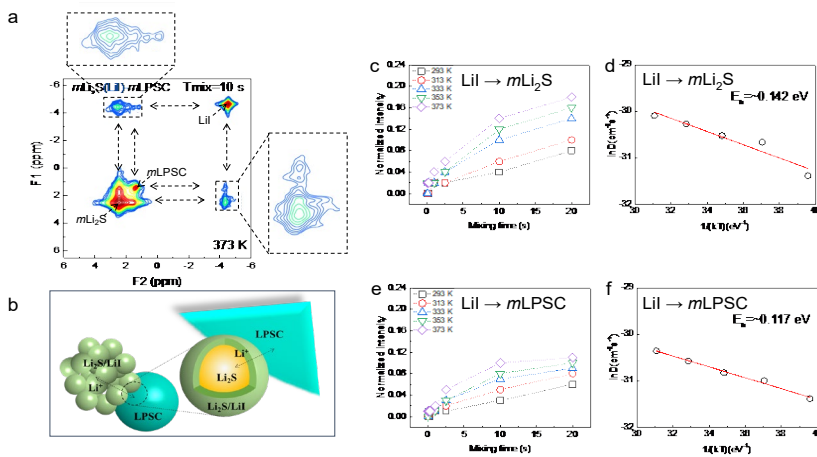


**Figure 5.4** Mechanism for  $\text{Li}^+$  transport in the  $m\text{Li}_2\text{S}(\text{Lil})\text{-mLPSC-C}$  cathodic mixtures. (a) Two-dimensional  $^6\text{Li}$ - $^6\text{Li}$  exchange spectra of the mixture of LPSC and  $\text{Li}_2\text{S}$ -Lil powders measured at spinning speed of 10 kHz at 100  $^\circ\text{C}$  and a mixing time of 10 s. (b) The proposed schematic mechanism for  $\text{Li}^+$  transport in the  $m\text{Li}_2\text{S}(\text{Lil})\text{-mLPSC-C}$  cathodic mixtures. (c, e) Evolution of the cross-peak intensity as a function of  $T_{\text{mix}}$  obtained from the temperature-dependent 2D-EXSY measurements. (d, f) Temperature dependence of the diffusion coefficient obtained from fitting the data in (c, e).

**Figure 5.4a** displays a clear exchange of  $\text{Li}^+$  between Lil and both  $\text{Li}_2\text{S}$  and LPSC, reflecting the equilibrium exchange of  $\text{Li}^+$  between the three phases in the cathodic mixture. This represents a unique view of the  $\text{Li}^+$  transport between a coating and the electrode and electrolyte phases in a solid-state battery. By measuring and fitting the exchange intensities as a function of the mixing time and temperature, **Figure 5.4c-f**, similar to the evaluation of the direct exchange between  $\text{Li}_2\text{S}$  and LPSC, the diffusion coefficients and activation energies over both the LPSC-Lil and Lil- $\text{Li}_2\text{S}$  interfaces is quantified. To the best of our knowledge, this is the first quantification of the local ion-diffusion between a coating and its facing solid phases, providing insight into the impact



of a coating on the Li-ion transport. The high diffusivity, very low activation energies, and for  $\text{Li}^+$  transfer from  $\text{Li}_2\text{S}$  to Lil and LPSC to Lil, 0.142 eV and 0.117 eV respectively, are similar to the overall  $\text{Li}^+$  transfer between  $\text{Li}_2\text{S}$  and LPSC. This indicates that Lil facilitates the transportation and thus functions as a bridge between electrode and electrolyte as summarized schematically in **Figure 5.4b**. Apparently, the ductile  $\text{LiI}^{40}$  creates grain boundaries between both the electrolyte and electrode material that do not pose an additional barrier for Li-ion diffusion, and the diffusivity of Lil itself dictates the diffusivity between electrode and electrolyte.

### 5.3.4 Electrochemical performance

To test the efficacy of the  $\text{Li}_2\text{S}$ -Lil cathode in combination with the micron-sized LPSC,  $m\text{Li}_2\text{S}(\text{Lil})\text{-}m\text{LPSC-C}|m\text{LPSC}|\text{In-Li}$  all-solid-state batteries were assembled during which only a mild pressure, 2MPa, was applied (see methods section for assembly details). The battery performance is shown in **Figure 5.5**. Although the battery can be activated during charge to over  $900 \text{ mA h g}^{-1}$  as shown in **Figure 5.1e**, discharge leads to large overpotentials. The increase of the oxidation potential towards  $900 \text{ mA h g}^{-1}$  exceeds the oxidation potential of Lil (2.3 V vs. In-Li) and that of the LPSC electrolyte (2.1 V vs. In-Li), which will result in poorly conducting species that increase the impedance. To prevent this, the battery is charged to specific capacities (fixed charge capacity) as shown in **Figure 5.5a**, followed by discharging to a fixed potential (0.8 V vs. In-Li) to achieve complete discharge. After the battery is initially charged to  $600 \text{ mA h g}^{-1}$  directly, the battery was cycled up to 50 cycles at different currents with an average Coulombic efficiency higher than 97.8% (**Figure 5.5b**). The 1<sup>st</sup>, 25<sup>th</sup> and 50<sup>th</sup> charge and discharge curves of the  $m\text{Li}_2\text{S}(\text{Lil})\text{-}m\text{LPSC-C}|m\text{LPSC}|\text{In-Li}$  battery cycled at  $0.132 \text{ mA cm}^{-2}$ , shown in **Figure 5.5c**, demonstrate an ultra-low activation potential of 1.7 V vs. In-Li, amounting to an overpotential of only about 100 mV, which is the lowest reported (**Figure 5.5d** and **Table S5.1**) to date. Post-mortem XRD analysis after different states of charge, and NMR analysis after 50 cycles (ending in the charged state) of the cycled  $m\text{Li}_2\text{S}(\text{Lil})\text{-}m\text{LPSC-C}$  active materials can be found in **Figure S5.7**. After the first charge to  $600 \text{ mA h g}^{-1}$  and even after the 50<sup>th</sup> charge to  $600 \text{ mA h g}^{-1}$ , only the  $\text{Li}_2\text{S}$  is oxidized, towards an amorphous structure, and the micron-sized LPSC solid electrolyte remains intact as no decomposition products are observed<sup>47</sup>. The long cycling stability of the battery with a higher mass loading,  $6.4 \text{ mg cm}^{-2}$ , is demonstrated in **Figure 5.5e**. After 200 cycles, the Coulombic efficiency maintains values exceeding 99.9% resulting in an average Coulombic efficiency of 99.6%. Most notable is that this is achieved in combination with a micron-sized electrolyte and that further optimization can be expected upon variation of the amount of Lil, the applied pressure, charge capacity and the cathodic mixture.

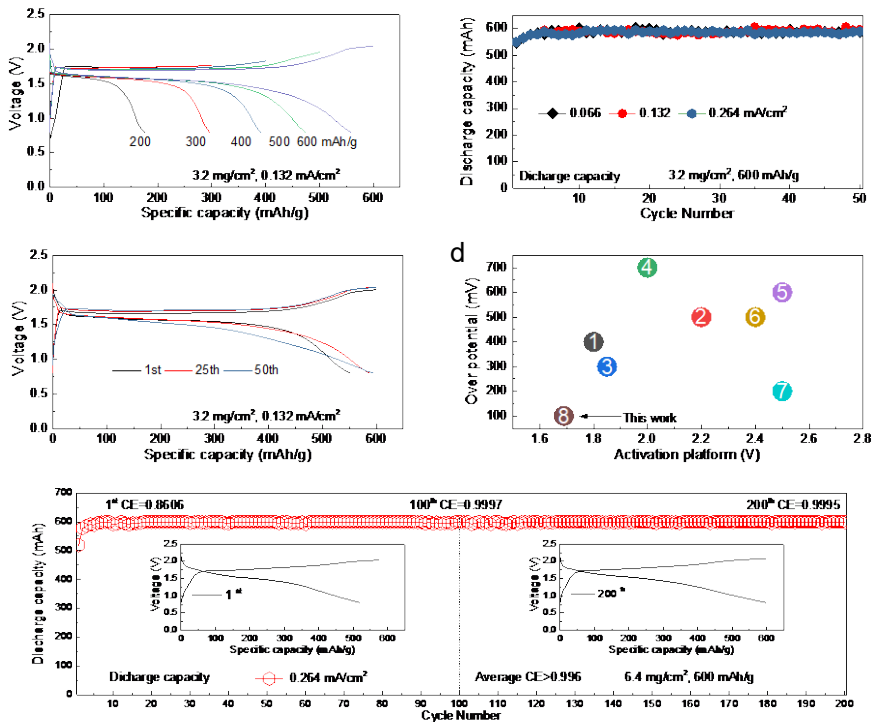


**Figure 5.5** Electrochemical performance of  $m\text{Li}_2\text{S(LiI)}\text{-mLPSC}$  batteries. (a) Charge and discharge curves of the  $m\text{Li}_2\text{S(LiI)}\text{-mLPSC-C|LPSC|In-Li}$  battery cycled incrementally from 200 to 600  $\text{mA h g}^{-1}$  at a  $0.132 \text{ mA cm}^{-2}$  current density; (b) Discharged capacity of  $m\text{Li}_2\text{S(LiI)}\text{-mLPSC-C|LPSC|In-Li}$  battery cycled to 600  $\text{mA h g}^{-1}$  at 0.066, 0.132 and  $0.264 \text{ mA cm}^{-2}$  respectively; (c) 1<sup>st</sup>, 25<sup>th</sup> and 50<sup>th</sup> charge and discharge curves of  $m\text{Li}_2\text{S(LiI)}\text{-mLPSC-C|LPSC|In-Li}$  battery cycled at  $0.132 \text{ mA cm}^{-2}$  current density; (d) Overpotential versus average activation voltage comparing results from literature as listed in **Table S1** with the present work; (e) Discharge capacity of the  $m\text{Li}_2\text{S(LiI)}\text{-mLPSC-C|LPSC|In-Li}$  battery cycled to 600  $\text{mA h g}^{-1}$  at  $0.264 \text{ mA cm}^{-2}$  current density up to 200 cycles.

## 5.4 Conclusions

In summary, the impact of a ductile coating on the diffusion over the grain boundary between the electrode and solid electrolyte is investigated. 2D exchange NMR reveals and quantifies the spontaneous equilibrium  $\text{Li}^+$  between  $\text{Li}_2\text{S}$  electrode, LiI coating and argyrodite  $\text{Li}_6\text{PS}_5\text{Cl}$  solid electrolyte, thus uniquely disentangling the impact of the coating on the  $\text{Li}^+$  diffusion. Effectively, the ductile LiI lowers the barrier for grain boundary diffusion towards both the  $\text{Li}_2\text{S}$  (electrode) and  $\text{Li}_6\text{PS}_5\text{Cl}$  (electrolyte) phases to such an extent that the conductivity of the thin LiI coating dominates. This improves the transport between electrode and electrolyte with several orders of magnitude and enables to move from nanostructured solid-state cathode mixtures to micron-sized solid-state cathode

mixtures, the latter having the practical advantages of high stability and facile material and electrode production. The impact of the improved transportation is demonstrated by a sulfide-based solid-state battery which combines easy activation of the sulfur electrode at very low overpotentials with stable cycling. This work demonstrates the ability of exchange NMR to unambiguously quantify and disentangle the  $\text{Li}^+$  transport over the interfaces between electrode, coating and solid electrolyte (three-phase exchange) in solid-state batteries. As one of the key challenges towards solid-state batteries is the development of interphases to establish stability and facile  $\text{Li}^+$  transport, the present approach and insights provide valuable insights to guide future understanding and material design.

### References

1. Goodenough, J. B.; Kim, Y., Challenges for rechargeable Li batteries. *Chem. Mater.* **2010**, *22* (3), 587-603.
2. Goodenough, J. B.; Park, K.-S., The Li-ion rechargeable battery: a perspective. *J. Am. Chem. Soc.* **2013**, *135* (4), 1167-1176.
3. Yu, C.; Ganapathy, S.; de Klerk, N. J.; Roslon, I.; van Eck, E. R.; Kentgens, A. P.; Wagemaker, M., Unravelling Li-Ion Transport from Picoseconds to Seconds: Bulk versus Interfaces in an Argyrodite  $\text{Li}_6\text{PS}_5\text{Cl-Li}_2\text{S}$  All-Solid-State Li-Ion Battery. *J. Am. Chem. Soc.* **2016**, *138* (35), 11192-201.
4. Yu, C.; Ganapathy, S.; Eck, E.; Wang, H.; Basak, S.; Li, Z.; Wagemaker, M., Accessing the bottleneck in all-solid-state batteries, lithium-ion transport over the solid-electrolyte-electrode interface. *Nat. Commun.* **2017**, *8* (1), 1086.
5. Tian, Y. S.; Shi, T.; Richards, W. D.; Li, J. C.; Kim, J. C.; Bo, S. H.; Ceder, G., Compatibility issues between electrodes and electrolytes in solid-state batteries. *Energy Environ. Sci.* **2017**, *10* (5), 1150-1166.
6. Manthiram, A.; Yu, X. W.; Wang, S. F., Lithium battery chemistries enabled by solid-state electrolytes. *Nat. Rev. Mater.* **2017**, *2* (4).
7. Kato, Y.; Hori, S.; Saito, T.; Suzuki, K.; Hirayama, M.; Mitsui, A.; Yonemura, M.; Iba, H.; Kanno, R., High-power all-solid-state batteries using sulfide superionic conductors. *Nat. Energy* **2016**, *1*.
8. Cheng, X. B.; Zhao, C. Z.; Yao, Y. X.; Liu, H.; Zhang, Q., Recent Advances in Energy Chemistry between Solid-State Electrolyte and Safe Lithium-Metal Anodes. *Chem* **2019**, *5* (1), 74-96.
9. Banerjee, A.; Tang, H. M.; Wang, X. F.; Cheng, J. H.; Nguyen, H.; Zhang, M. H.; Tang, D. H. S.; Wynn, T. A.; Wu, E. A.; Doux, J. M.; Wu, T. P.; Ma, L.; Sterbinsky, G. E.; D'Souza, M. S.; Ong, S. P.; Meng, Y. S., Revealing Nanoscale Solid-Solid Interfacial Phenomena for Long-Life and High-Energy All-Solid-State Batteries. *ACS Appl. Mater. Interfaces.* **2019**, *11* (46), 43138-43145.
10. Han, F. D.; Zhu, Y. Z.; He, X. F.; Mo, Y. F.; Wang, C. S., Electrochemical Stability of  $\text{Li}_{10}\text{GeP}_2\text{S}_{12}$  and  $\text{Li}_7\text{La}_3\text{Zr}_2\text{O}_{12}$  Solid Electrolytes. *Adv. Energy Mater.* **2016**, *6* (8).

11. Yan, H. F.; Wang, H. C.; Wang, D. H.; Li, X.; Gong, Z. L.; Yang, Y., In Situ Generated  $\text{Li}_2\text{S-C}$  Nanocomposite for High-Capacity and Long-Life All-Solid-State Lithium-Sulfur Batteries with Ultrahigh Areal Mass Loading. *Nano Lett.* **2019**, *19* (5), 3280-3287.
12. Xu, R. C.; Han, F. D.; Ji, X.; Fan, X. L.; Tu, J. P.; Wang, C. S., Interface engineering of sulfide electrolytes for all-solid-state lithium batteries. *Nano Energy* **2018**, *53*, 958-966.
13. Schwietert, T. K.; Arszewlewska, V. A.; Wang, C.; Yu, C.; Vasileiadis, A.; de Klerk, N. J. J.; Hageman, J.; Hupfer, T.; Kerkamm, I.; Xu, Y.; van der Maas, E.; Kelder, E. M.; Ganapathy, S.; Wagemaker, M., Clarifying the relationship between redox activity and electrochemical stability in solid electrolytes. *Nat. Mater.* **2020** *19*, 428-435.
14. Liu, M.; Wang, C.; Cheng, Z.; Ganapathy, S.; Haverkate, L. A.; Unnikrishnan, S.; Wagemaker, Controlling the Li-metal growth to enable low Li-metal excess all-solid-state Li-metal batteries. *ACS Mater. Lett.* **2020** *2*, 665-670.
15. de Klerk, N. J. J.; Wagemaker, M., Space-Charge Layers in All-Solid-State Batteries; Important or Negligible? *ACS Appl. Energy Mater.* **2018**, *1* (10), 5609-5618.
16. Swift, M. W.; Qi, Y., First-Principles Prediction of Potentials and Space-Charge Layers in All-Solid-State Batteries. *Phys. Rev. Lett.* **2019**, *122* (16).
17. Park, J.; Kim, J. Y.; Shin, D. O.; Oh, J.; Kim, J.; Lee, M. J.; Lee, Y.-G.; Ryou, M.-H.; Lee, Y. M. Dimension-controlled solid oxide electrolytes for all-solid-state electrodes: Percolation pathways, specific contact area, and effective ionic conductivity. *Chem. Eng. J.* **2020**, *391*, 123528.
18. Quartarone, E.; Mustarelli, Electrolytes for solid-state lithium rechargeable batteries: recent advances and perspectives. *Chem. Soc. Rev.* **2011**, *40* (5), 2525-2540.
19. Xu, K. Electrolytes and interphases in Li-ion batteries and beyond. *Chem. Rev.* **2014**, *114* (23), 11503-11618.
20. Liu, M.; Cheng, Z.; Ganapathy, S.; Wang, C.; Haverkate, L. A.; Tulodziecki, M.; Unnikrishnan, S.; Wagemaker, M., Tandem Interface and Bulk Li-Ion Transport in a Hybrid Solid Electrolyte with Microsized Active Filler. *ACS Energy Lett.* **2019**, *4* (9), 2336-2342.
21. Simon, F. J.; Hanauer, M.; Henss, A.; Richter, F. H.; Janek, Interfaces, Properties of the interphase formed between argyrodite-type  $\text{Li}_{16}\text{PS}_5\text{Cl}$  and polymer-based PEO10: LiTFSI. *ACS Appl. Mater. Interfaces* **2019**, *11* (45), 42186-42196.

22. Simon, F. J.; Hanauer, M.; Richter, F. H.; Janek, Interphase Formation of PEO20: LiTFSI–Li6PS5Cl Composite Electrolytes with Lithium Metal. *ACS Appl. Mater. Interfaces* **2020**, *12* (10), 11713-11723.
23. de Klerk, N. J. J.; Roslon, T.; Wagemaker, M., Diffusion Mechanism of Li Argyrodite Solid Electrolytes for Li-Ion Batteries and Prediction of Optimized Halogen Doping: The Effect of Li Vacancies, Halogens, and Halogen Disorder. *Chem. Mater.* **2016**, *28* (21), 7955-7963.
24. Ganapathy, S.; Yu, C.; van Eck, E. R. H.; Wagemaker, M., Peeking across Grain Boundaries in a Solid-State Ionic Conductor. *ACS Energy Lett.* **2019**, *4* (5), 1092-1097.
25. Tan, D. H. S.; Wu, E. A.; Nguyen, H.; Chen, Z.; Marple, M. A. T.; Doux, J. M.; Wang, X. F.; Yang, H. D.; Banerjee, A.; Meng, Y. S., Elucidating Reversible Electrochemical Redox of Li6PS5Cl Solid Electrolyte. *ACS Energy Lett.* **2019**, *4* (10), 2418-2427.
26. de Klerk, N. J. J.; van der Maas, E.; Wagemaker, M., Analysis of Diffusion in Solid-State Electrolytes through MD Simulations, Improvement of the Li-Ion Conductivity in beta-Li3PS4 as an Example. *ACS Appl Energy Mater.* **2018**, *1* (7), 3230-3242.
27. Zhu, Y. Z.; He, X. F.; Mo, Y. F., Origin of Outstanding Stability in the Lithium Solid Electrolyte Materials: Insights from Thermodynamic Analyses Based on First-Principles Calculations. *ACS Appl. Mater. Interfaces* **2015**, *7* (42), 23685-23693.
28. Richards, W. D.; Miara, L. J.; Wang, Y.; Kim, J. C.; Ceder, G., Interface Stability in Solid-State Batteries. *Chem. Mater.* **2016**, *28* (1), 266-273.
29. Hakari, T.; Hayashi, A.; Tatsumisago, M., Li2S-Based Solid Solutions as Positive Electrodes with Full Utilization and Superlong Cycle Life in All-Solid-State Li/S Batteries. *Adv. Sustain Syst.* **2017**, *1* (6).
30. Xu, R. C.; Yue, J.; Liu, S. F.; Tu, J. P.; Han, F. D.; Liu, P.; Wang, C. S., Cathode-Supported All-Solid-State Lithium-Sulfur Batteries with High Cell-Level Energy Density. *ACS Energy Lett.* **2019**, *4* (5), 1073-1079.
31. Yu, C.; Hageman, J.; Ganapathy, S.; van Eijck, L.; Zhang, L.; Adair, K. R.; Sun, X. L.; Wagemaker, M., Tailoring Li6PS3Br ionic conductivity and understanding of its role in cathode mixtures for high performance all-solid-state Li-S batteries. *J. Mater. Chem. A* **2019**, *7* (17), 10412-10421.

32. Han, F.; Yue, J.; Fan, X.; Gao, T.; Luo, C.; Ma, Z.; Suo, L.; Wang, C., High-Performance All-Solid-State Lithium-Sulfur Battery Enabled by a Mixed-Conductive  $\text{Li}_2\text{S}$  Nanocomposite. *Nano Lett.* **2016**, *16* (7), 4521-7.
33. El-Shinawi, H.; Cussen, E. J.; Corr, S. A., A facile synthetic approach to nanostructured  $\text{Li}_2\text{S}$  cathodes for rechargeable solid-state Li-S batteries. *Nanoscale* **2019**, *11* (41), 19297-19300.
34. Wu, F. X.; Lee, J. T.; Zhao, E. B.; Zhang, B.; Yushin, G., Graphene- $\text{Li}_2\text{S}$ -Carbon Nanocomposite for Lithium-Sulfur Batteries. *ACS Nano* **2016**, *10* (1), 1333-1340.
35. Famprakis, T.; Canepa, P.; Dawson, J. A.; Islam, M. S.; Masquelier, Fundamentals of inorganic solid-state electrolytes for batteries. *Nat. Mater.* **2019**, 1-14.
36. Fu, K. K.; Gong, Y.; Dai, J.; Gong, A.; Han, X.; Yao, Y.; Wang, C.; Wang, Y.; Chen, Y.; Yan, C. Flexible, solid-state, ion-conducting membrane with 3D garnet nanofiber networks for lithium batteries. *Proc. Natl. Acad. Sci.* **2016**, *113* (26), 7094-7099.
37. Fu, K. K.; Gong, Y.; Hitz, G. T.; McOwen, D. W.; Li, Y.; Xu, S.; Wen, Y.; Zhang, L.; Wang, C.; Pastel, Three-dimensional bilayer garnet solid electrolyte based high energy density lithium metal-sulfur batteries. *Energy. Environ. Sci.* **2017**, *10* (7), 1568-1575.
38. Suyama, M.; Kato, A.; Sakuda, A.; Hayashi, A.; Tatsumisago, M., Lithium dissolution/deposition behavior with  $\text{Li}_3\text{PS}_4\text{-LiI}$  electrolyte for all-solid-state batteries operating at high temperatures. *Electrochim. Acta* **2018**, *286*, 158-162.
39. Han, F. D.; Yue, J.; Zhu, X. Y.; Wang, C. S., Suppressing Li Dendrite Formation in  $\text{Li}_2\text{S-P}_2\text{S}_5$  Solid Electrolyte by LiI Incorporation. *Adv. Energy. Mater.* **2018**, *8* (18), 1703644.
40. Singh, N.; Horwath, J. P.; Bonnicksen, P.; Suto, K.; Stach, E. A.; Matsunaga, T.; Muldoon, J.; Arthur, The role of lithium iodide addition to lithium thiophosphate: Implications beyond conductivity. *Chem. Mater.* **2020**, *32*, 7150-7158.
41. Grey, C. P.; Dupre, N., NMR studies of cathode materials for lithium-ion rechargeable batteries. *Chem. Rev.* **2004**, *104* (10), 4493-4512.
42. Pecher, O.; Carretero-Gonzalez, J.; Griffith, K. J.; Grey, C. P., Materials' Methods: NMR in Battery Research. *Chem. Mater.* **2017**, *29* (1), 213-242.
43. Wenzel, S.; Sedlmaier, S. J.; Dietrich, C.; Zeier, W. G.; Janek, J., Interfacial reactivity and interphase growth of argyrodite solid electrolytes at lithium metal electrodes. *Solid State Ion.* **2018**, *318*, 102-112.

44. Koerver, R.; Walther, F.; Aygun, I.; Sann, J.; Dietrich, C.; Zeier, W. G.; Janek, J., Redox-active cathode interphases in solid-state batteries. *J. Mater. Chem. A* **2017**, *5* (43), 22750-22760.
45. Zhao, Q.; Lu, Y. Y.; Zhu, Z. Q.; Tao, Z. L.; Chen, J., Rechargeable Lithium-Iodine Batteries with Iodine/Nanoporous Carbon Cathode. *Nano Lett.* **2015**, *15* (9), 5982-5987.
46. Liu, M.; Ren, Y. X.; Jiang, H. R.; Luo, C.; Kang, F. Y.; Zhao, T. S., An efficient  $\text{Li}_2\text{S}$ -based lithium-ion sulfur battery realized by a bifunctional electrolyte additive. *Nano Energy* **2017**, *40*, 240-247.
47. Liu, M.; Zhou, D.; He, Y. B.; Fu, Y. Z.; Qin, X. Y.; Miao, C.; Du, H. D.; Li, B. H.; Yang, Q. H.; Lin, Z. Q.; Zhao, T. S.; Kang, F. Y., Novel gel polymer electrolyte for high-performance lithium-sulfur batteries. *Nano Energy* **2016**, *22*, 278-289.



Supporting Information for Chapter 5

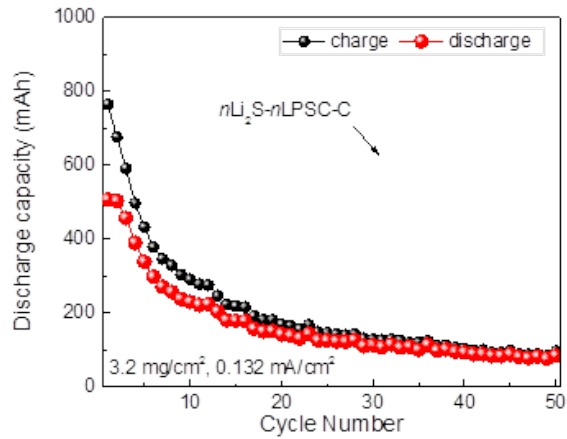


Figure S5.1 Cycle performance of battery with the nLi<sub>2</sub>S-nLPSC-C cathode.

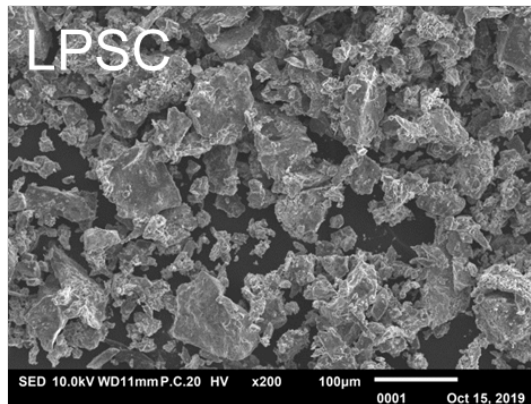
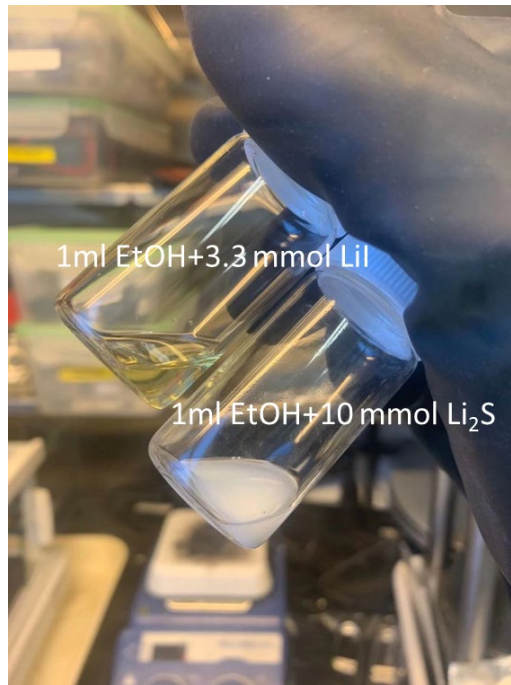
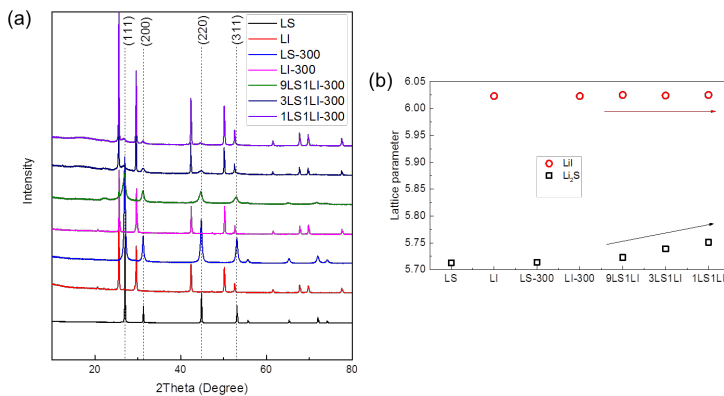


Figure S5.2 SEM images of micron-sized LPSC.



**Figure S5.3** Optical image of 3.3 mmol fully dissolved LiI and 10 mmol partially dissolved Li<sub>2</sub>S in 1 ml ethanol respectively.



**Figure S5.4** (a) XRD patterns and (b) fits of the lattice parameter of the Li<sub>2</sub>S, LiI and Li<sub>2</sub>S-LiI materials. All the patterns are fitted with the Rietveld method as implemented in GSAS. The arrows show the variation tendency of lattice parameters for different samples.

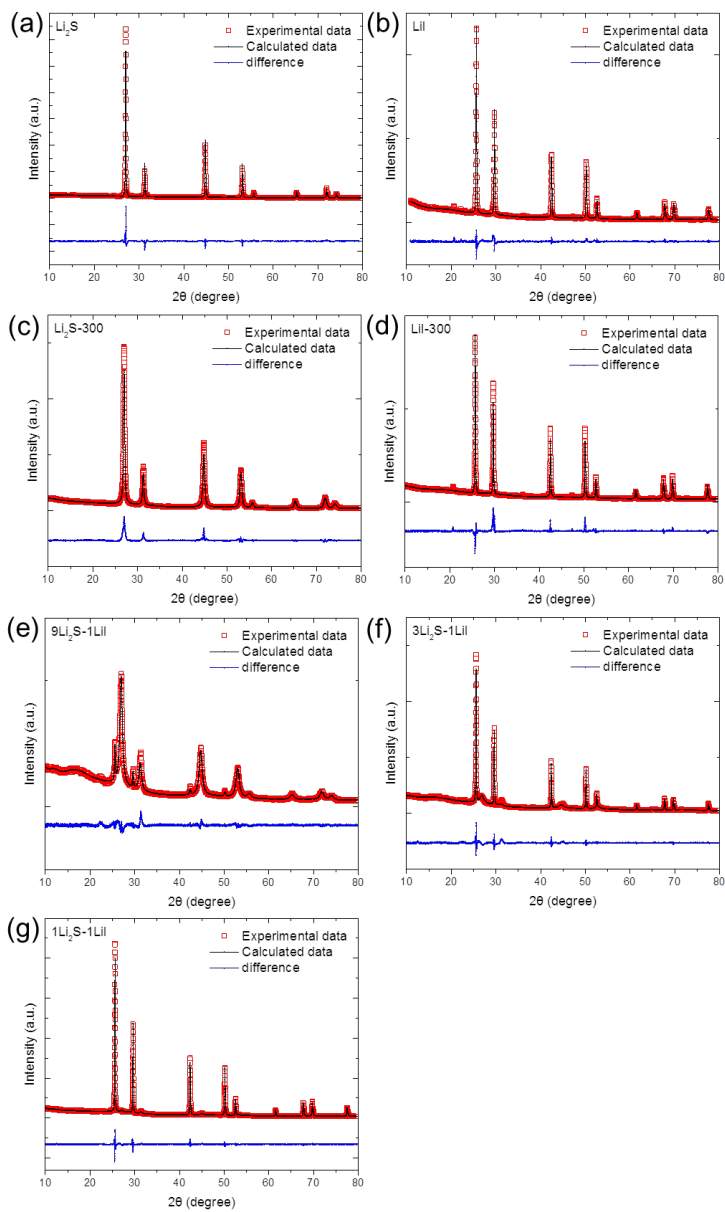


Figure S5.5 Rietveld refinement of  $\text{Li}_2\text{S}$ ,  $\text{LiI}$  and  $\text{Li}_2\text{S-LiI}$  based on diffraction patterns given in Figure S5.4.

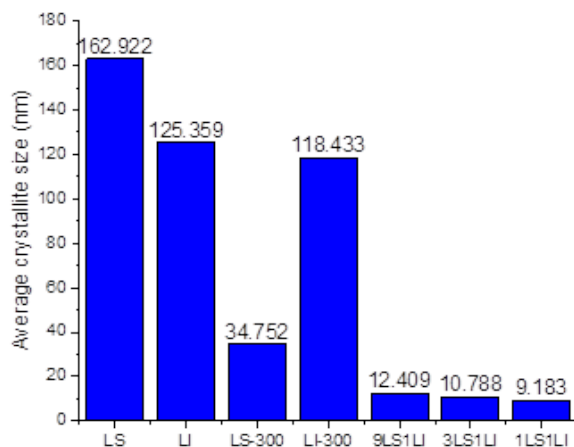


Figure S5.6 Average crystallite size of  $\text{Li}_2\text{S}$ ,  $\text{LiI}$  and  $\text{Li}_2\text{S}$  in  $\text{Li}_2\text{S-LiI}$  based on the Rietveld refinement in Figure S5.5.

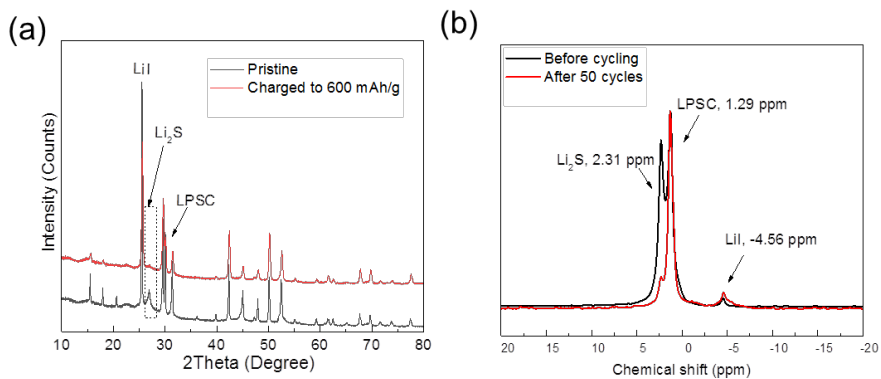


Figure S5.7 Post mortem (a) XRD and (b) NMR analysis of the  $m\text{Li}_2\text{S(LiI)}-m\text{LPSC-C}$  active materials after activation to  $600 \text{ mA h g}^{-1}$  and after 50 cycles to  $600 \text{ mA h g}^{-1}$  under the charged state.

**Table S5.1** Activation voltage and overpotential in our work compared with open literature as shown in **Figure 5.4d**.

Title	Activation platform	Over-potential	Reference number
Accessing the bottleneck in all-solid-state batteries, lithium-ion transport over the solid-electrolyte electrode interface	~1.8 V vs. In-Li	~400 mV	1
Li <sub>2</sub> S-Based Solid Solutions as Positive Electrodes with Full Utilization and Super long Cycle Life in All-Solid-State Li/S Batteries	~2.4 V vs. In-Li	~500 mV	2
In Situ Generated Li <sub>2</sub> S–C Nanocomposite for High-Capacity and Long-Life All-Solid-State Lithium-Sulfur Batteries with Ultrahigh Areal Mass Loading	~1.85 V vs. In-Li	~300 mV	3
High-Performance All-Solid-State Lithium–Sulfur Battery Enabled by a Mixed-Conductive Li <sub>2</sub> S Nanocomposite	~2 V vs. In-Li	~700 mV	4
High performance all-solid-state lithium-sulfur battery using a Li <sub>2</sub> S-VGCF nanocomposite	~2.5 V vs. In-Li	~600 mV	5
Cathode-Supported All-Solid-State Lithium-Sulfur Batteries with High Cell-Level Energy Density	~2.4 V vs. In-Li	~500 mV	6
Carbon-coated Li <sub>2</sub> S cathode for improving the electrochemical properties of an all-solid-state lithium-sulfur battery using Li <sub>2</sub> S-P2S5 solid electrolyte	~2.5 V vs. In-Li	~200 mV	7
<b>This work</b>	1.69 V vs. In-Li	~100 mV	8

### References

- S5.1 Yu, C. *et al.* Accessing the bottleneck in all-solid-state batteries, lithium-ion transport over the solid-electrolyte-electrode interface. *Nat Commun.* **8**, 1086 (2017).
- S5.2 Hakari, T. *et al.* Li<sub>2</sub>S-Based Solid Solutions as Positive Electrodes with Full Utilization and Superlong Cycle Life in All-Solid-State Li/S Batteries. *Adv. Sustain Syst.* **1**, 1700017 (2017).
- S5.3 Yan, H. F. *et al.* In Situ Generated Li<sub>2</sub>S-C Nanocomposite for High-Capacity and Long-Life All-Solid-State Lithium-Sulfur Batteries with Ultrahigh Areal Mass Loading. *Nano Lett.* **19**, 3280-3287 (2019).
- S5.4 Han, F. *et al.* High-Performance All-Solid-State Lithium-Sulfur Battery Enabled by a Mixed-Conductive Li<sub>2</sub>S Nanocomposite. *Nano Lett.* **16**, 4521-4527, (2016).
- S5.5 Eom, M. *et al.* High performance all-solid-state lithium-sulfur battery using a Li<sub>2</sub>S-VGCF nanocomposite. *Electrochim. Acta*, **230**, 279-284 (2017).
- S5.6 Xu, R. C. *et al.* Cathode-Supported All-Solid-State Lithium-Sulfur Batteries with High Cell-Level Energy Density. *ACS Energy Lett.* **4**, 1073-1079 (2019).
- S5.7 Choi, S. *et al.* Carbon-coated Li<sub>2</sub>S cathode for improving the electrochemical properties of an all-solid-state lithium-sulfur battery using Li<sub>2</sub>S-P<sub>2</sub>S<sub>5</sub> solid electrolyte. *Ceram. Int.* **44**, 7450-7453 (2018).

### Summary

Rechargeable Li-ion batteries for the market of electrical vehicles, portable equipment for entertainment, computing and telecommunication surge for the past decades, but the increasing demands introduce great challenges towards future battery systems that require higher energy and power density, improved safety as well as a longer lifespan. Lithium metal batteries can deliver higher energy densities compared with commercialized LIBs but the practical applications have been hindered due to the growth of lithium dendrites in liquid lithium metal batteries. The uncontrollable dendrite leads to the repeated formation of solid electrolyte interphase, irreversible capacity loss, short circuits, and safety hazards with liquid electrolytes. Compared to liquid electrolytes, solid-state electrolytes might be a better choice, but the reliance of ionic diffusion at the contact of solid particles is crucial presenting a major challenge. Moreover, the effective use of high capacity cathodes in combination with Li metal in a solid-state battery is another big challenge for future battery development. Therefore, to unlock the full potential of LMBs with high energy density and safe operation, it is imperative to devote efforts in solid-state batteries design. This thesis aims to search effective methods for enabling safe and high-energy-density solid-state Li metal batteries, starting from the developments of new concepts in liquid-based batteries and heading for an anode less Li metal solid-state battery configuration step by step.

The challenge faced by Li-metal anodes firstly is to prevent dendritic and mossy Li-metal growth that lead to low electrochemical plating/stripping efficiencies. In **Chapter 2**, Li metal stripping and plating was studied in the liquid-based battery in the presence of a high dielectric material that aims to annihilate the driving force of dendrites. Electrical field calculations show that through the ferroelectric effect, the presence of a high dielectric material  $\text{BaTiO}_3$  takes away the electrical field gradient at the tip of nearby Li-metal deposits, suggesting that the Li-metal dendritic and mossy microstructure growth can be suppressed by an anode comprising of a high dielectric porous scaffold. Operando  $^7\text{Li}$  solid-state NMR of an anode-less BTO scaffold- $\text{LiCoO}_2$  full cell demonstrates that the high dielectric scaffold induces compact plating and efficient stripping. Half-cells with a BTO scaffold cycled against Li-metal exhibits 99.82% CE after the first two initial cycles, low overpotentials and an extended cycle life even in the worst-case scenario using 1 M  $\text{LiPF}_6$  EC/DMC electrolyte, under different current and capacity conditions. With the same basic electrolyte, full cells also demonstrate improved performance with an average CE of 99.37%. These results demonstrate the use of high dielectric scaffolds that take away the driving force for inhomogeneous Li-metal deposition as a strategy to improve the reversibility and safety of Li-metal anodes in an anode-less configuration.

Based on the impact of high dielectric materials on the Li plating and stripping process, studied in the aforementioned chapter, the concept is transferred to a solid-state battery design in **Chapter 3**. A 3D integrally-formed BTO-based matrix has been successfully synthesized for an all-solid-state Li metal battery. Stable cycling of the solid-state Li metal symmetrical battery ( $1\text{ mA cm}^{-2}$ ,  $2\text{ mA h cm}^{-2}$ ) is achieved, and much higher Coulombic efficiencies in full cells with this 3D matrix were realized. This proved successful in restricting the electrolyte decomposition, as examined by solid-state NMR, which is crucial to improve solid-state battery performance. These results show promise for the practical application of composite Li metal anodes with solid electrolytes for the development of all-solid-state batteries and shed light on the future design of all-solid-state batteries.

Generally, cycling of solid electrolytes in combination with Li-metal anodes is demonstrated using a thick Li-metal anode. Ideally, the battery is assembled in its discharged state, without a major excess of Li-metal, hence with the solid electrolyte directly facing the current collector. This is a much more challenging condition, in practice leading to severe delamination of the solid electrolyte from the current collector upon repeated Li-metal plating/stripping, resulting in early cell death. In **Chapter 4**, we explore a potential strategy to improve the HSE/Cu interface by introducing a 100 nm thin film of ZnO on the copper current collector, effectively making the current collector lithium-philic. The conversion reaction upon lithiation results in a regular distribution of small Zn-Li particles, acting as seed crystals for Li-metal plating. A stable solid-state full cell composed of prelithiated ZnO@Cu cathode and LiFePO<sub>4</sub> cathode was demonstrated, providing insights into a potential route towards solid-state Li-metal batteries.

The last chapter represents an attempt to enable a suitable high energy sulfide cathode for Li metal solid-state batteries, aiming for an anode-less configuration. In **Chapter 5**, we propose a simple solvent method to deposit Lil at the interfaces between the sulfur cathode and the argyrodite solid electrolyte to achieve facile Li-ion transport in combination with improved stability in solid-state batteries. The solvent method results in micron-sized agglomerates of nanostructured Li<sub>2</sub>S coated by Lil, which increases the conductivity of the agglomerates as compared to micron-sized Li<sub>2</sub>S. Secondly, the ductile Lil can be expected to result in good ionic contact area where the present results demonstrate that this leads to radically improved transportation between the electrode and solid electrolyte, despite the relatively small ionic contact area associated with the micron-sized solid electrolyte and electrode. These two aspects are responsible for the exceptional low overpotential upon cycling, which prevent potentials that induce oxidation of both the solid electrolyte and Lil interface species. The result is a sulfide-based solid-state battery which is easily activated, cycles at a  $600\text{ mA h g}^{-1}$  capacity for more than 200 cycles with



a Coulombic efficiency of more than 99.6% under mild pressure (2MPa). The present low contact area interface strategy unites facile charge transport and stability, resolving a key challenge towards high-performance solid-state battery performance.

In summary, this thesis explores potential configurations for the development of safe and high-energy-density solid-state lithium metal batteries. It is proved that the presence of high dielectric material, in this case, BaTiO<sub>3</sub>, takes away the electrical field gradient at the tip of nearby Li-metal deposits and suppresses the formation of dendritic and mossy microstructure in the liquid-based electrolyte. This concept was also able to improve the cycling of Li metal anodes in a solid-state battery concept, intrinsically alleviating the growth of lithium dendrites. We further explored anode-free or anode-less configurations by deposition of thin film ZnO on the copper current collector to improve the SE/Cu interface and make the current collector lithium-philic for homogeneous Li-metal plating. Last but not least, by depositing Lil at the interfaces between the sulfur cathode and the argyrodite solid electrolyte, a facile Li-ion transport in combination with improved stability in solid-state lithium metal batteries was achieved. These fundamental findings presented in this thesis aim to contribute to the understanding of the limiting processes in next-generation batteries, providing approaches that may be valuable for the development of future high energy density lithium metal batteries.

### Samenvatting

In de afgelopen decennia zijn oplaadbare Li-ion-batterijen sterk opgekomen in de markt voor elektrische voertuigen, draagbare apparatuur voor entertainment, computers en telecommunicatie, maar de toenemende eisen stellen grote uitdagingen aan toekomstige batterijsystemen die een hogere energie- en vermogensdichtheid, verbeterde veiligheid en een langere levensduur vereisen. Lithium-metaalbatterijen kunnen hogere energiedichtheden leveren in vergelijking met commerciële LIB's, maar de praktische toepassingen worden belemmerd door de groei van lithiumdendrieten in lithiummetaalbatterijen met vloeibaar elektrolyt. De oncontroleerbare dendriet leidt tot de herhaalde vorming van een vaste elektrolyt-interfase, onomkeerbaar capaciteitsverlies, kortsluiting en veiligheidsrisico's met vloeibare elektrolyten. Vergeleken met vloeibare elektrolyten zijn elektrolyten in de vaste toestand misschien een betere keuze, maar de afhankelijkheid van ionendiffusie bij het contact tussen vaste deeltjes is cruciaal en vormt een majeure uitdaging. Daarenboven vormt effectief gebruik van kathodes met hoge capaciteit in combinatie met Li-metaal in een vaste-stofbatterij een andere grote uitdaging voor de ontwikkeling van toekomstige batterijen. Om het volledige potentieel van LMB's met hoge energiedichtheid en veilige werking te ontsluiten, is het daarom noodzakelijk om inspanningen te leveren in het ontwerp van vaste-stofbatterijen. Dit proefschrift heeft tot doel effectieve methoden te zoeken voor het mogelijk maken van veilig vaste-stof-Li-metaal met hoge energiedichtheid, uitgaande van de ontwikkeling van nieuwe concepten in op vloeistof gebaseerde batterijen, stap voor stap op weg naar een anode-loze Li-metaal vaste-stof batterijconfiguratie.

De uitdaging waarmee Li-metaalanodes worden geconfronteerd, is in de eerste plaats het voorkomen van dendritische en bemoste Li-metaalgroei die leiden tot lage elektrochemische platerings/stripefficiënties. In **Hoofdstuk 2** werd het strippen en plateren van Li-metaal bestudeerd in de vloeistofgebaseerde batterij in de aanwezigheid van een hoog diëlektrisch materiaal dat tot doel heeft de drijvende kracht voor dendrietvorming te annihilieren. Berekeningen van het elektrisch veld laten zien dat door het ferro-elektrisch effect de aanwezigheid van hoog diëlektrisch materiaal  $\text{BaTiO}_3$  de elektrische veldgradiënt aan de punt van nabijgelegen Li-metaalafzettingen wegneemt, wat suggereert dat de groei van dendritische en bemoste microstructuren van Li-metaal kan worden onderdrukt door een anode bestaande uit een hoog diëlektrische poreus exoskelet. Operando  $^7\text{Li}$  vaste-stof NMR van een anode-loze BTO exoskelet- $\text{LiCoO}_2$  volledige cel toont aan dat het hoog diëlektrische exoskelet compact plateren en efficiënt strippen induceert. Cycli van halve cellen met een BTO-exoskelet tegen Li-metaal vertonen 99,82% CE na de eerste twee

initiële cycli, lage overpotentialen en een langere levensduur wanneer het ongunstigste scenario van 1 M LiPF<sub>6</sub> EC/DMC-elektrolyt wordt gebruikt, onder verschillende stroomsterkte- en capaciteitsvoorwaarden. Met dezelfde basiselektrolyt vertonen volledige cellen ook verbeterde prestaties met een gemiddelde CE van 99,37%. Deze resultaten demonstreren het gebruik van hoog diëlektrische exoskeletten die de drijvende kracht voor inhomogene Li-metaalafzetting wegnemen als een strategie om de omkeerbaarheid en veiligheid van Li-metaalanodes in een anode-loze configuratie te verbeteren.

Gebaseerd op de impact van hoog-diëlektrische materialen op het Li-plateer-en stripproces, bestudeerd in het vorige hoofdstuk, wordt het concept overgebracht naar een vaste-stof batterij-ontwerp in **Hoofdstuk 3**. Een 3D integraal gevormde en op BTO gebaseerde matrix is met succes gesynthetiseerd voor een volledige vaste-stof Li-metaalbatterij. Stabiliteit onder cycli van de vaste-stof Li-metaal symmetrische batterij (1 mA cm<sup>-2</sup>, 2 mA h cm<sup>-2</sup>) wordt bereikt en veel hogere Coulomb efficiëntie in volledige cellen met deze 3D-matrix werd gerealiseerd. Dit bleek succesvol in het beperken van de elektrolytafbraak, zoals onderzocht door middel van vaste-stof NMR, wat cruciaal is om de prestaties van vaste-stof batterijen te verbeteren. Deze resultaten zijn veelbelovend voor de praktische toepassing van composiet Li-metaalanodes met vaste elektrolyten voor de ontwikkeling van volledig vaste-stof batterijen en werpen licht op het toekomstige ontwerp van volledig-vaste-stof batterijen.

In het algemeen wordt het gedrag onder cycli van vaste elektrolyten in combinatie met Li-metaalanodes getoond met gebruik van een dikke Li-metaalanode. Idealiter wordt de batterij in ontladen toestand geassembleerd, zonder een grote overmaat aan Li-metaal, dus met de vaste elektrolyt direct naar de stroomcollector gericht. Dit is een veel uitdagender conditie, die in de praktijk leidt tot ernstige delaminatie van de vaste elektrolyt uit de stroomcollector bij herhaaldelijk plateren/strippen met Li-metaal, wat resulteert in vroege celdood. In **Hoofdstuk 4** onderzoeken we een mogelijke strategie om het HSE/Cu grensvlak te verbeteren door een 100 nm dunne film van ZnO op de koperen stroomcollector te plaatsen, waardoor de stroomcollector effectief lithifiel wordt. De omzettingsreactie na lithiatie resulteert in een regelmatige verdeling van kleine Zn-Li-deeltjes, die fungeren als kiemkristallen voor Li-metaalplateren. Een stabiele vaste-stof volledige cel bestaande uit een vooraf gelithieerde ZnO@Cu-kathode en LiFePO<sub>4</sub>-kathode werd gedemonstreerd, wat inzicht gaf in een mogelijke route naar vaste-stof Li-metaalbatterijen.

Het laatste hoofdstuk vertegenwoordigt een poging om een geschikte hoogenergetische sulfidekathode mogelijk te maken voor Li-metalen vaste-stofbatterijen, waarbij wordt gestreefd naar een anode-loze configuratie. In **Hoofdstuk 5** stellen we een eenvoudige

oplosmiddelmethode voor om Lil af te zetten op de grensvlakken tussen de zwavelkathode en de vaste elektrolyt van argyrodiet om een gemakkelijk Li-ion transport te bereiken in combinatie met verbeterde stabiliteit in vaste-stof batterijen. De oplosmiddelmethode resulteert in agglomeraten van nanogestructureerd  $\text{Li}_2\text{S}$  van micronformaat, gecoat met Lil, waardoor de geleidbaarheid van de agglomeraten toeneemt in vergelijking met  $\text{Li}_2\text{S}$  van micronformaat. Ten tweede kan worden verwacht dat het ductiele Lil resulteert in een goed ionisch contactoppervlak, waar de huidige resultaten aantonen dat dit leidt tot een radicaal verbeterd ladingstransport tussen de elektrode en de vaste elektrolyt, ondanks het relatief kleine ionische contactoppervlak dat geassocieerd is met de vaste elektrolyt van micronformaat en elektrode. Deze twee aspecten zijn verantwoordelijk voor de uitzonderlijk lage overpotentiala bij cycli, die potentialen voorkomt die oxidatie van zowel de vaste elektrolyt als de Lil-grensvlakspecies induceren. Het resultaat is een op sulfide gebaseerde vaste-stof batterij die gemakkelijk kan worden geactiveerd, cycli kan ondergaan met een capaciteit van  $600 \text{ mA h g}^{-1}$  gedurende meer dan 200 cycli met een Coulomb-efficiëntie van meer dan 99,6% onder milde druk (2 MPa). De huidige grensvlakstrategie met een laag contactoppervlak verenigt gemakkelijk ladingstransport en stabiliteit, en verhelpt daarmee een belangrijke uitdaging voor de prestaties van krachtige vaste-stof batterijen.

Samenvattend verkent dit proefschrift mogelijke configuraties voor de ontwikkeling van veilige lithium-metaalbatterijen met hoge energiedichtheid. Het is bewezen dat de aanwezigheid van hoog diëlektrisch materiaal, in dit geval  $\text{BaTiO}_3$ , de elektrische veldgradiënt aan het uiteinde van nabijgelegen Li-metaalafzettingen wegneemt en de vorming van dendritische en mosachtige microstructuur in de vloeistofgebaseerde elektrolyt onderdrukt. Dit concept was ook in staat om het gedrag onder cycli van Li-metaalanodes in een vaste-stof batterijconcept te verbeteren, waardoor de groei van lithiumdendrieten intrinsiek werd verlicht. We hebben anode-vrije of anode-loze configuraties verder onderzocht door een dunne laag ZnO af te zetten op de koperen stroomcollector om het SE/Cu grensvlak te verbeteren en de stroomcollector lithifiel te maken om homogene Li-metaalbeplating te bereiken. Tenslotte maar niet minder belangrijk, werd door Lil af te zetten op de grensvlakken tussen de zwavelkathode en de vaste elektrolyt van argyrodiet, een gemakkelijk Li-ionentransport in combinatie met verbeterde stabiliteit in vaste lithium-metaalbatterijen bereikt. Deze fundamentele bevindingen die in dit proefschrift worden gepresenteerd, zijn bedoeld om bij te dragen aan het begrip van de beperkende processen in batterijen van de volgende generatie, door benaderingen te bieden die waardevol kunnen zijn voor de ontwikkeling van toekomstige lithium-metaalbatterijen met hoge energiedichtheid.



### Acknowledgements

Upon the completion of this thesis, I would like to take this special opportunity to express my sincere gratitude to all the people who have helped me, supported me, inspired me and encouraged me during my whole PhD journey in the Netherlands.

First and foremost, I would like to thank my supervisor/promotor, Prof. Marnix Wagemaker, who performs more than a mentor in the development of my research career. Thanks for your patient guidance and encouragement in my PhD journey, which inspires me in performing researches more independently and critically. Without your coherent and illuminating instruction, this thesis would not have reached its present form so smoothly. I am also indebted to my second promotor Prof. Ekkes Brück for revising this thesis and remarkable suggestions for my work. Without your help and generosity, this thesis cannot be finished on time.

I am also grateful to my master supervisor Prof. Yan-Bing He from Tsinghua University, where I started my research journey, he has taught and inspired me a lot on the way of my scientific research. Without his recommendation and support, I couldn't get the opportunity to start my PhD at the Delft University of Technology (TUD), which is a big turning point in my life. Warm thanks once again go to all of my supervisors, Marnix and Yan-Bing, for your contributions, and I feel so lucky to meet all of you in my life.

Next, I would like to express my gratitude to Jouke Heringa, Frans Ooms, Michel Steenvoorden, Bert Zwart, Kees Goubitz, Baukje Terpstra and Michel Thijs for their strong technical support for lab facilities and simulations. Jouke is acknowledged for his kind help with a Dutch translation of the summary and preparation of office facilities. Frans, Michel, Baukje and Kees gave me the introduction of lab facilities, helped me order and prepare all the chemicals I need for the experiments, and assist me to design the experiment in the thesis. Bert has helped me with the sealing of the quartz tubes, otherwise, no solid electrolyte can be achieved. Special thanks to Michel Thijs, who has helped me a lot with the Comsol simulations even in the Christmas Eve. I also wish to thank the secretaries, Ilse van der Kraaji and Nicole Banga, who are always friendly to solve the administrative problems and have helped me solve the accommodation problem when I was here four years ago.

Very special thanks to Ming Liu, who is more than a nice colleague, an excellent collaborator and a good friend. He has inspired me strongly during the research process and supported me from all aspects of the thesis writing. It is a nice and wonderful experience to get

## Acknowledgements

---

acquaintances here from Tsinghua University. I can still recall the wonderful time we went to the open market in Rotterdam for shopping with Kun Qian, Zhu Cheng, Zhimin Zhou, Ming and his wife. And the unforgettable time, we went to the snow world for skiing.

I extend my sincere thanks to all members of the Storage of Electrochemical Energy (SEE), Fundamental Aspects of Materials (FAME) and Neutron Positron Methods for Materials (NPM2) faculties in TUD who are great persons to work with and also nice friends in life. There are many names I would like to mention with great pleasure: Alexandros, Angie, Anton, Bei, Bert, Bowei, Chandra, Chenglong, Ekkes, Erik, Eveline, Fengqi, Guorei, Hamutu, Hanan, Huan Huan, Jiawei, Jun, Kun, Lars, Mark, Martijn, Michael, Niek, Niels, Peter Paul, Pranav, Qidi, Remco, Shiv, Swapna, Tammo, Tomas, Victor, Violetta, Walter, Wenqin, Xinmin, Yifan, Zhaolong, Zhimin, Zhou, Zhu, Ziwei and many more.

I still remember the happy skiing and rock climbing time, from which I acquired some new skills and got a lot of fun. Another unforgettable thing is the barbecue activity for the whole SEE group members which takes place every year in the whole summer. Thanks for all of you make my life pleasant and full of variety outside the PhD work.

Last but not the least, I would like to express my deep gratitude to my family for their warm caring and selfless love. I am greatly indebted to my beloved parents and girlfriend Qiulin. Love you forever.

Chao Wang

2021.01.19 Delft

### List of Publications

#### Publications related to this thesis

1. **Chao Wang**, Ming Liu, Michel Thijs, Frans G.B. Ooms, Swapna Ganapathy and Marnix Wagemaker, High Dielectric 3D Scaffold to Suppress Lithium-Dendrites and Increase the Reversibility of Anode-less Lithium-Metal Anodes, *Nature Communications*, major revision.
2. **Chao Wang**, Ming Liu, Lars J. Bannenberg, Michel Thijs, Frans G.B. Ooms, Swapna Ganapathy and Marnix Wagemaker, High Dielectric Barium Titanate Skeleton for All-Solid-state Lithium-Metal Battery, To be submitted.
3. **Chao Wang**, Ming Liu, Zhu Cheng, Swapna Ganapathy, Lucas A. Haverkate, Sandeep Unnikrishnan and Marnix Wagemaker, Controlling the Lithium-Metal Growth To Enable Low-Lithium-Metal-Excess All-Solid-State Lithium-Metal Batteries, *ACS Materials Letters*, **2020**, 2, 665-670.
4. **Chao Wang**, Ming Liu, Chenglong Zhao, Eveline van der Maas, Kui Lin, Violetta A. Arszewska, Baohua Li, Swapna Ganapathy and Marnix Wagemaker, Combining Facile Ionic Transport with Interface Stability in Sulfur-Based All-Solid-State-Batteries, *Nature Communications*, minor revision.

#### Other Publications

5. Remco van der Jagt, Alexandros Vasileiadis, Hugo Veldhuizen, Pengpeng Shao, Xiao Feng, Swapna Ganapathy, Nicolas C. Habisreutinger, Monique A. van der Veen, **Chao Wang**, Marnix Wagemaker, Sybrand van der Zwaag and Atsushi Nagai, Synthesis and Structure–Property Relationships of Polyimide Co-valent Organic Frameworks for Carbon Dioxide Capture and (Aqueous) Sodium-ion Batteries, *Chemistry of Materials* (**2021**).
6. Tammo K. Schwietert, Violetta A. Arszewska, **Chao Wang**, Chuang Yu, Alexandros Vasileiadis, Niek J. J. de Klerk, Jart Hageman, Thomas Hupfer, Ingo Kerkamm, Yaolin Xu, Eveline van der Maas, Erik M. Kelder, Swapna Ganapathy and Marnix Wagemaker, Clarifying the Relationship between Redox Activity and Electrochemical Stability in Solid Electrolytes, *Nature Materials*, **2020**, 19(4), 428-435.
7. Ming Liu, Zhu Cheng, Swapna Ganapathy, **Chao Wang**, Lucas A. Haverkate, Michał Tułodziecki, Sandeep Unnikrishnan and Marnix Wagemaker, Tandem Interface and Bulk



- Li-Ion Transport in a Hybrid Solid Electrolyte with Microsized Active Filler, *ACS Energy Letters*, **2019**, 4, 2336–2342.
8. Ming Liu, Zhu Cheng, Kun Qian, Tomas Verhallen, **Chao Wang** and Marnix Wagemaker, Efficient Li-Metal Plating/Stripping in Carbonate Electrolytes Using a LiNO<sub>3</sub>-Gel Polymer Electrolyte, Monitored by Operando Neutron Depth Profiling, *Chemistry of Materials*, **2019**, 31, 4564–4574.
  9. Jiaming Ma, Yinping Wei, Lin Gan, **Chao Wang**, Heyi Xia, Wei Lv, Jia Li, Baohua Li, Quan-Hong Yang, Feiyu Kang and Yan-Bing He, Abundant Grain Boundaries Activate Highly Efficient Lithium-Ion Transportation in High Rate Li<sub>4</sub>Ti<sub>5</sub>O<sub>12</sub> Compact Microspheres, *Journal of Materials Chemistry A*, **2019**, 7, 1168-1176.
  10. Peter-Paul R.M.L. Harks, Carla B. Robledo, Chandramohan George, **Chao Wang**, Thomas van Dijk, Leon Sturkenboom, Erik D.W. Roesink, Fokko M. Mulder, Immersion Precipitation Route towards High Performance Thick and Flexible Electrodes for Li-ion Batteries, *Journal of Power Sources*, **2019**, 441, 227200.
  11. Linkai Tang, Yan-Bing He, **Chao Wang**, Shuan Wang, Marnix Wagemaker, Baohua Li, Quan-Hong Yang and Feiyu Kang, High-Density Microporous Li<sub>4</sub>Ti<sub>5</sub>O<sub>12</sub> Microbars with Superior Rate Performance for Lithium-Ion Batteries, *Advanced Science*, **2017**, 4, 1600311.
  12. Cuiping Han, Yan-Bing He, Shuan Wang, **Chao Wang**, Hongda Du, Xianying Qin, Zhiqun Lin, Baohua Li and Feiyu Kang, Large Polarization of Li<sub>4</sub>Ti<sub>5</sub>O<sub>12</sub> Lithiated to 0 V at Large Charge/Discharge Rates, *ACS Applied Materials & Interfaces*, **2016**, 8, 29, 18788–18796.
  13. Yan Zhao, Ming Liu, Wei Lv, Yan-Bing He, **Chao Wang**, Qinbai Yun, Baohua Li, Feiyu Kang, Quan-Hong Yang, Dense Coating of Li<sub>4</sub>Ti<sub>5</sub>O<sub>12</sub> and Graphene Mixture on the Separator to Produce Long Cycle Life of Lithium-Sulfur Battery, *Nano Energy*, **2016**, 30, 1-8.
  14. **Chao Wang**, Shuan Wang, Linkai Tang, Yan-Bing He, Lin Gan, Jia Li, Hongda Du, Baohua Li, Zhiqun Lin, Feiyu Kang, A Robust Strategy for Crafting Monodisperse Li<sub>4</sub>Ti<sub>5</sub>O<sub>12</sub> Nanospheres as Superior Rate Anode for Lithium-Ion Batteries, *Nano Energy*, **2016**, 21, 133–144. (ESI Highly Cited Paper)
  15. **Chao Wang**, Shuan Wang, Yan-Bing He, Linkai Tang, Cuiping Han, Cheng Yang, Marnix Wagemaker, Baohua Li, Quan-Hong Yang, Jang-Kyo Kim and Feiyu Kang, Combining Fast Li-Ion Battery Cycling with Large Volumetric Energy Density: Grain Boundary Induced

## Publications

---

High Electronic and Ionic Conductivity in  $\text{Li}_4\text{Ti}_5\text{O}_{12}$  Spheres of Densely Packed Nanocrystallites, *Chemistry of Materials*, **2015**, 27, 5647–5656.

## Patents

1. Y.-B. He, **C. Wang**, L.K. Tang, et al, Authorized patent number: **CN 105118979**
2. Y.-B. He, **C. Wang**, S. Wang, et al, Authorized patent number: **CN 105070897**
3. S. Wang, **C. Wang**, C. Han, Y.-B. He, et al, Authorized patent number: **CN 104282906**
4. Y.-B. He, L.K. Tang, S. Wang, **C. Wang**, et al, Authorized patent number: **CN 105070898**
5. Y.-B. He, L.K. Tang, S. Wang, **C. Wang**, et al, Authorized patent number: **CN 106410146**
6. M. Wagemaker, **C. Wang**. High dielectric electrode additives to achieve dendrite free stable Li-metal plating. Applied.

### Curriculum Vitae

**Chao Wang** was born on 08 October 1989 in Hubei, China. He started his research and got his Master degree majored in Materials Engineering in July 2016 at Tsinghua University. After that, he started his PhD study upon high energy density lithium metal batteries in the group of Storage of Electrochemical Energy at Delft University of Technology supervised by Prof. dr. Ir. Marnix Wagemaker and was financially supported by Guangzhou Elite Project.